Study of Charged Kaon production in Three-prong Tau decays

WEI HAO

NIKHEF-H, Kruislaan 409, P.O. Box 41882, NL-1009 DB Amsterdam
email: hao@nikhef.nl
telephone: (+31)-20-592 5018
fax: (+31)-20-592 5155

Structure of the thesis, LaTeX run 13:16 3rd December 1995

Study of Charged Kaon Production in Three-prong Tau Decays

Proefschrift

TER VERKRIJGING VAN DE GRAAD VAN DOCTOR
AAN DE RIJKSUNIVERSITEIT TE LEIDEN,
OP GEZAG VAN DE RECTOR MAGNIFICUS DR. L. LEERTOUWER,
HOOGLERAAR IN DE FACULTEIT DER GODGELEERDHEID,
VOLGENS BESLUIT VAN HET COLLEGE VAN DEKANEN
TE VERDEDIGEN OP DONDERDAG 1 FEBRUARI 1996
TE KLOKKE 14:15 UUR

door

Wei Hao

geboren te Beijing, P. R. China, op 30 november 1961

Promotiecommissie:

Promotor:	Prof. dr. A.N. Diddens	
Co-Promotor:	Dr. W. Ruckstuhl	(NIKHEF-H, Amsterdam)
Overige Leden:	Prof. dr. J. Amesz	
	Prof. dr. F.A. Berends	
	Prof. dr. R.H.P. Kleiss	
	Prof. dr. J.J. Engelen	(Universiteit van Amsterdam)
	Dr. W.L.G.A.M. van Neerven	
	Dr. B. Koene	(NIKHEF-H, Amsterdam)

For copies of this thesis, contact the author or the library at NIKHEF-H (P.O. Box 41882, NL-1009 DB Amsterdam, the Netherlands, e-mail: library@nikhef.nl)

The work described in this thesis is part of the research programme of 'het Nationaal Instituut voor Kernfysica en Hoge-Energie Fysica' (NIKHEF-H) in Amsterdam. The author was financially supported by 'de Stichting voor Fundamenteel Onderzoek der Materie' (FOM).

Contents

1 Introduction **1**

2 Theory **3**
2.1 Standard Model 3
2.2 Physics of the τ Lepton 6
2.2.1 Properties of the τ 6
2.2.2 Theory of semileptonic τ decay 8

3 Apparatus **13**
3.1 DELPHI 13
3.1.1 Tracking 13
3.1.2 Calorimetry 15
3.1.3 On-line Systems and Off-line Software 16
3.2 The Ring Imaging Cherenkov detectors of DELPHI 16
3.2.1 Principle of operation 17
3.2.2 The Barrel RICH 19
3.2.3 The Forward RICH 20
3.2.4 K/π separation with the RICH 22

4 On-line Calibration of the Forward RICH **23**
4.1 UV calibration system of the FRICH 23
4.2 Calibration Results 26
4.2.1 Data Selection 26
4.2.2 Determination of Drift velocity and Lorentz angle 27
4.3 Monitoring 30
4.3.1 High Voltage on the MWPC modules 31
4.3.2 Discriminator thresholds 31
4.3.3 Absorption of UV light in TMAE 31
4.3.4 Attenuation length of photo-electron drift 32
4.3.5 Drift diffusion 33
4.4 Summary and Discussion 34

5 Track Selection and Performance of the RICH **37**
5.1 Track Selection 37
5.2 Ring Identification 39

5.2.1 Angular Resolution 39
5.2.2 Improvement of the Cherenkov angle measurement 41
5.2.2.1 Mirror alignment 41
5.2.2.2 Top and bottom difference 43
5.2.2.3 Drift velocity 44
5.2.2.4 Miscellaneous 45
5.2.3 Photon Clusters 45
5.2.4 Reconstruction of the Cherenkov Ring 46
5.3 Veto Identification 47
5.4 Performance in single-prong τ decay 49

6 Data Analysis **51**
6.1 Event selection 51
6.2 Kaon Identification in 3-prong τ decays 52
6.2.1 Photon Selection 52
6.2.2 Ring Identification 54
6.2.3 Veto Identification 59
6.3 Branching Ratios in 3-prong τ decays to Kaons 62
6.3.1 Kaon Production in 3-prong τ decays 62
6.3.2 Inclusive Branching ratios 65
6.3.3 Exclusive Branching ratios 68
6.4 Further study of the decays $\tau \to KK\pi\nu_\tau(\pi^\circ)$ and $\tau \to K\pi\pi\nu_\tau(\pi^\circ)$ . . 69
6.4.1 Resonances in the decays 70
6.4.2 Interpretation of the results and Comparison with other experiments 71

7 Summary and Discussion **75**

Bibliography **79**

Summary **83**

samenvatting **85**

Acknowledgements **87**

Curriculum Vitae **89**

Chapter 1

Introduction

The history of mankind shows that people have an instinctive interest in learning about the world around them, and in trying to explain all kinds of phenomena in nature. In ancient China a book, known as the *Book of Changes*[*] in the West, says that the basic units of the world are water, fire, wood, metal and earth. This comes from the brains of some philosophers and is based on the experience of daily life. Modern science is based on experiment. The motivation for spending time and money on these subjects is not only scientific curiosity, but also their applications and the benefits for human life. The A-bomb is clearly not one of them.

Matter can be broken down into small pieces, molecules. A molecule is made of atoms and an atom is made of a nucleus containing protons and neutrons, surrounded by electrons. One step deeper, inside the proton and neutron, quarks were found. The traditional goal of particle physics has been to identify what appear to be the structureless units of matter and to understand the forces acting between the particles. At present it is understood that the basic constituents of matter are six leptons and six quarks. The interactions between them are classified in four types according to their strength: the gravitational, weak, electro-magnetic and strong interaction. To study these constituents and their interactions, high energy is needed to break the matter into small pieces. Therefore this part of physics is called elementary particle physics or high energy physics.

In the 20th century tremendous developments have taken place in physics. At the beginning of the century two great theories, the Theory of Relativity and the Theory of Quantum Mechanics, have influenced science fundamentally in general. A few years later the two theories were combined. The application of quantum mechanics to the electromagnetic field led to Quantum Electrodynamics (QED) with many predictions that were confirmed experimentally later on. Later, a unified theory of the electromagnetism and of the weak interaction took shape. Together with Quantum Chromodymamics, which describes the strong force, the electroweak theory forms the theory of modern elementary particle physics, the Standard Model.

To create the possibilities for further tests of the Standard model, LEP (Large Electron-Positron collider), has been constructed at CERN[†]. It is located at the

[*] or *Yi Jing*, written around 1000 B.C.

[†] European Organisation for Nuclear Research

Swiss-French border near Geneva. The machine is positioned in a tunnel of 27 km circumference situated 100m underground. It provides e^+ and e^- beams of equal energies, circulating in opposite direction and colliding at 4 interaction points. The energy of the beams is around 45 GeV (LEP phase 1) and will be upgraded to about 90 GeV later (LEP phase 2). Both types of particles are concentrated in 4 bunches. At each of the 4 interaction regions a detector has been constructed. They are called OPAL, ALEPH, L3 and DELPHI. Each collaboration consists of a few hundred physicists from many countries. The construction cost of each detector is around 100 MSFr.

The heaviest lepton τ provides a nice tool to study the interaction between the weak charged current and hadrons which is not available in the other two leptons. Many semi-leptonic τ decays have been studied in the last few years, but some of the decays have not been measured very well due to their low branching ratios or the difficulties of identifying the particles in the final states. Some questions, like what are the dominant resonances in the decays, motivate physicists spending time on this subject. Due to its unique position amongst the elementary particles the τ-lepton may also give us some surprises. The aim of this thesis is to study the decays of τ lepton into charged kaon(s). In the analysis presented in this thesis, the data from the DELPHI detector taken in 1992,1993 and 1994 are used. The relevant theory is outlined in chapter 2. The DELPHI detector is briefly described in chapter 3. In the chapters 4 and 5 contributions of the author are presented, on detector calibration and on data treatment. The physics analysis is shown in chapter 6 and chapter 7 summarises the results and draws the conclusions.

Chapter 2

Theory

Over a century ago, Maxwell unified the electric and magnetic force in classical electrodynamics. This still stands at speeds approaching the velocity of light, unlike Newton's classical mechanics that requires a correction at relativistic velocities as was shown by Einstein. Combining the Maxwell theory with quantum mechanics, the first modern gauge theory, QED, was constructed. QED predicts the electromagnetic interaction at high precision. Analoguously to QED, Quantum Chromo-Dynamics (QCD) was developed to describe the strong interaction of quarks. In the weak interaction the field quanta must be massive vector particles. Glashow[1], Weinberg[3] and Salam[2]have developed it as a gauge theory, in which the symmetry is hidden. It is called the electroweak theory or the GWS theory. It unifies the weak interaction with QED, and therefore describes the weak and electromagnetic interaction of both quarks and leptons. The theory predicts new gauge particles: Z^0 and $W^{\pm}$. They were discovered in their theoretically expected mass ranges in 1983[4], and no significant experimental deviation from the Standard Model has been found since.

2.1 Standard Model

According to the Standard Model, the basic constitutions of matter are spin 1/2 fermions. They are grouped in families, each containing 2 leptons and 2 quarks. They are considered to be pointlike particles, and they interact with each other via the strong, weak and electromagnetic interaction* by exchanging intermediate vector bosons. In addition, the scalar Higgs boson is conjectured to be responsible for the masses of the fermions and the gauge bosons. Table 2.1 lists these elementary particles with their quantum numbers.

The Standard Model of particle physics consists of the three gauge theories, mentioned before. They are based on the principle of local gauge invariance, *i.e.* invariance under certain local space-time dependent phase transformations. The corresponding gauge group is $SU_C(3) \times SU_L(2) \times U_Y(1)$.

* The effect of gravity is many orders of magnitude smaller than even the weak force. Therefore it is absent from our story.

fermions	family			Q	I_3	Y
	1	2	3			
leptons	ν_e	ν_μ	ν_τ	0	1/2	-1
	e	μ	τ	-1	-1/2	-1
quarks	u	c	t	2/3	1/2	1/3
	d	s	b	-1/3	-1/2	1/3
gauge bosons	γ			0		
	Z^0			0		
	$W^\pm$			± 1		
gluons	g_i (i=1,8)			0		
Higgs boson	H^0			0		

Table 2.1: *The three known families of elementary fermions, the gauge bosons and the Higgs boson with their quantum numbers: Q is the charge, I_3 is the third conponent of weak isospin and Y is the weak hypercharge.*

The gauge group $SU_L(2) \times U_Y(1)$ corresponds to the GWS theory and is referred to as the Standard Model of Electroweak Interaction. The $SU_L(2)$ part describes the force acting on left-handed weak isospin doublets.† The requirement of local $SU_L(2)$ gauge invariance entails the introduction of three gauge fields, with two charged gauge particles $W^\pm$ and an electrically neutral one. In order to deal with the weak neutral current and electromagnetic current, a new $U(1)$ gauge group is introduced. It is associated with weak hypercharge(Y) and unifies the electromagnetic and weak interactions completely. The electric charge is given by:

$$Q = I_3 + \frac{Y}{2} \tag{2.1}$$

The electromagnetic current(γ) and weak neutral current(Z^0) are identified as linear combinations of the neutral component of $SU_L(2)$ and that of $U_Y(1)$. The mixing between $SU_L(2)$ and $U_Y(1)$ is given by the weak mixing angle θ_W, that may be expressed in term of the W and Z masses:

$$\sin^2\theta_W \equiv 1 - \frac{m_W^2}{m_Z^2} = 0.23 \tag{2.2}$$

The tree level diagrams of the electroweak coupling to fermions are:

† All right-handed components are singlets under the weak isospin group

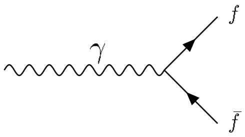

$$= -ieQ_f\gamma_\mu \qquad \begin{pmatrix} f \text{ can be any fermion} \\ \text{and } e = \sqrt{4\pi\alpha} \end{pmatrix}$$

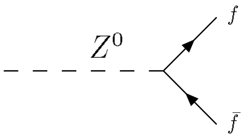

$$= \frac{-ie\gamma_\mu(g_{\mathrm{V}}^f - g_{\mathrm{A}}^f\gamma_5)}{2\sin\theta_W\cos\theta_W} \qquad (\ f \text{ can be any fermion}\ )$$

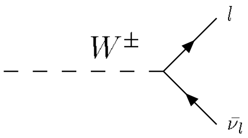

$$= \frac{-ie\gamma_\mu(1-\gamma_5)}{2\sqrt{2}\sin\theta_W} \qquad \begin{pmatrix} l = \mathrm{e},\ \mu \text{ or } \tau \text{ with} \\ \bar{\nu}_l \text{ the corresponding} \\ \text{anti-neutrino} \end{pmatrix}$$

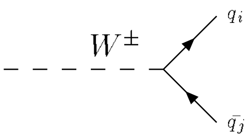

$$= \frac{-ie\gamma_\mu(1-\gamma_5)}{2\sqrt{2}\sin\theta_W}\cdot V_{ij} \qquad \begin{pmatrix} q_i = \mathrm{u, c \text{ or } t};\ q_j = \mathrm{d}, \\ \mathrm{s \text{ or } b};\ V \text{ is the CKM} \\ \text{matrix} \end{pmatrix}$$

where

$$g_{\mathrm{V}}^f = I_3^f - 2Q_f\sin^2\theta_W$$

$$g_{\mathrm{A}}^f = I_3^f$$

Differently from the electromagnetic and the strong interactions, flavour is not conserved in the weak interaction. The transformations for quark mass eigenstates to weak interaction eigenstates are described by a unitary 3×3 matrix, called Cabibbo-Kobayashi-Maskawa (or CKM) matrix:

$$\begin{pmatrix} d' \\ s' \\ b' \end{pmatrix} = \begin{pmatrix} V_{ud} & V_{us} & V_{ub} \\ V_{cd} & V_{cs} & V_{cb} \\ V_{td} & V_{ts} & V_{tb} \end{pmatrix} \begin{pmatrix} d \\ s \\ b \end{pmatrix} \tag{2.3}$$

The diagonal elements are close to 1, so those transitions are favoured. The off-diagonal elements are smaller than 1 and those transitions are referred to as Cabibbo-suppressed. Historically it is more convenient to use the Cabibbo angle θ_c:

$$\sin\theta_c = |V_{us}| = 0.22 \tag{2.4}$$

The local $SU_C(3)$ symmetry governs the strong interaction of quarks. It refers to a new degree of freedom, colour. Each quark exists in three colours while the leptons are colourless. The strong interactions are mediated by the exchange of massless gluons.

2.2 Physics of the τ Lepton

The τ lepton has been studied extensively since its discovery in 1975[5]. In the Standard Model, the sequential lepton τ and its associated neutrino form a weak doublet and belong to the third, presumably the last, family of leptons and quarks. It is the heaviest known lepton and the only one that is able to decay into hadrons. Therefore it provides a perfect tool to test the universality of the weak interaction, to study the weak interaction under simple conditions and to investigate cleanly the formation of resonances in hadronic states. It may also be a sensitive probe of physics beyond the Standard Model.

2.2.1 Properties of the τ

The τ was discovered in 1975 in the process $e^+e^- \to \tau^+\tau^- \to e\mu+$ missing energy. Since then many properties of the τ were measured[6]. From this we know that the τ has spin 1/2 and does not interact through strong interactions. The results show that the τ is the third sequential lepton with its own conserved lepton number and one associated neutrino.

Many theoretical predictions have been established, by Tsai[7] and others[8]-[12]. Some of them were made even before the discovery of the τ. More detailed pictures of the τ properties were described in many excellent reviews[13][14][15]. The decays of the $\tau^{-\ddagger}$ are described within the Standard Model by the Feynman diagrams shown in Fig 2.1.

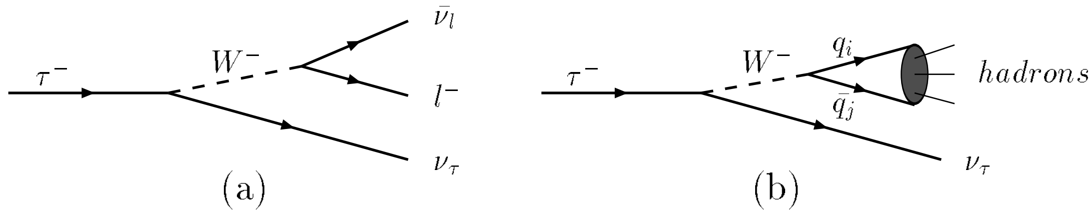

Figure 2.1: *Feyman diagram of tau decays (a) to leptons, (b) to hadrons.*

The width of leptonic τ decay, neglecting the radiative correction, can be expressed as:[7]

$$\Gamma(\tau \to \bar{\nu}_l l \nu_\tau) = \frac{G_\tau G_l m_\tau^5}{384\pi^4} \int d\Omega \int dx x^2 [3 - 2x \mp (\overrightarrow{\omega} \cdot \hat{p}_l)(2x-1)] \qquad (2.5)$$

where m_τ is the τ mass, $x = E/E_{max}$ is the scaled energy of the decay lepton l, $\overrightarrow{\omega}$ is the τ polarisation vector, and $\hat{p}_l$ is the unit vector along the direction of the decay lepton. G_l and G_τ are the weak current coupling constants for leptons.

‡ A specific charge state implies also the charge conjugate state.

If the masses of the final state particles can be neglected then the integral reduces to the value 2π, leading to the simple form:

$$\Gamma(\tau \to \bar{\nu}_l l \nu_\tau) \approx \frac{G_\tau G_l m_\tau^5}{192\pi^3} \tag{2.6}$$

With the first order electroweak correction, that takes into account the radiative process and the effects of the finite masses, assuming the neutrino to be massless[9], it becomes:

$$\Gamma(\tau \to \bar{\nu}_l l \nu_\tau) = \frac{G_\tau G_l m_\tau^5}{192\pi^3} f(y)[1 + \frac{3}{5}\frac{m_\tau^2}{m_W^2}][1 + \frac{\alpha(m_\tau)}{2\pi}(\frac{25}{4} - \pi^2)] \tag{2.7}$$

where $\alpha(m_\tau) = 1/133.3$ is the running coupling constant of QED at the τ mass scale. The function $f(y)$ accounts for the non-zero masses of final state leptons:

$$f(y) = 1 - 8y + 8y^3 - y^4 - 12y^2 \ln y \tag{2.8}$$

where $y = (m_l/m_\tau)^2$. For a τ decay into a muon, $f(y) = 0.9726$.

The mass of the τ lepton has been determined from a detailed measurement of the energy dependence of the τ production cross section $\sigma(e^+e^- \to \tau^+\tau^-)$ near the threshold. The new result from BES gives: $m_\tau = 1776.9 \pm 0.4 MeV$[16]. The τ life time was determined from the decay path measurement. The decay length is about $2\ mm$ at the LEP energy. Recent results from LEP benefit from the addition of high spatial resolution silicon micro-vertex detectors. The world average value is $\tau_\tau = (291.6 \pm 1.6) \times 10^{-15} s$[17]. Most of the results on leptonic branching ratios are based on counting the number of τ decays into leptons, correcting for acceptance and efficiency and estimating the number of produced τ's from the luminosity measurement. The latest results are: $Br(\tau \to e\bar{\nu}_e\nu_\tau) = (17.793 \pm 0.086)\%$ and $Br(\tau \to \mu\bar{\nu}_\mu\nu_\tau) = (17.333 \pm 0.087)\%$[17].

The electron-muon-tau universality ($G_e = G_\mu = G_\tau = G = 1.166 \times 10^{-5} GeV^{-2}$) predicts that these two decays should have the same branching fraction, apart from a phase space suppression factor ($f = 0.9726$). The observed ratio of couplings is:

$$\frac{G_e}{G_\mu} = \frac{Br(\tau \to e\bar{\nu}_e\nu_\tau)}{Br(\tau \to \mu\bar{\nu}_\mu\nu_\tau)} \cdot f = 1.0008 \pm 0.0035 \tag{2.9}$$

It compares well with the best test of $e - \mu$ universality from $\pi \to l\bar{\nu}_l$ decays[18], giving $\frac{G_\mu}{G_e} = 1.0012 \pm 0.0016$.

The $\tau - \mu$ universality ($G_\mu = G_e$) has been tested by the electronic branching fraction of τ decay, that can be related to that of the μ decay via the masses and lifetimes of the leptons:

$$Br(\tau \to e\bar{\nu}_e\nu_\tau) = \left(\frac{m_\tau}{m_\mu}\right)^5 \left(\frac{\tau_\tau}{\tau_\mu}\right) \tag{2.10}$$

The new results give agreement within one standard deviation[17].

The leptonic τ decay is well understood and provides a good deal of information on the weak interaction. The chiral structure of the decay was determined to be V-A by studying the momentum spectrum of the electrons in the decay $\tau \to e\bar{\nu}_e\nu_\tau$.

Comparing with leptonic decays, the semileptonic decays are less well understood but can be calculated with a few theoretical assumptions. Table 2.2 lists some measured branching fractions of semileptonic τ^- decays[41] with their theoretical predictions[8] –[12].

Decay	Branching Ratios (%)	Theory Prediction (%)
$\tau^- \to \pi^-\nu_\tau$	11.09 ± 0.15	10.95
$\tau^- \to K^-\nu_\tau$	0.68 ± 0.04	0.723
$\tau^- \to K^*(892)^-\nu_\tau$	1.36 ± 0.08	1.15
$\tau^- \to \rho^-\nu_\tau \to \pi^-\pi^0\nu_\tau$	24.91 ± 0.21	24.4
$\tau^- \to h^-h^-h^+(neutrals)\nu_\tau$	14.49 ± 0.23	—
$\tau^- \to \pi^-\pi^-\pi^+\nu_\tau$	8.64 ± 0.24	$6.4 - 12.6$
$\tau^- \to K^-\pi^-\pi^+\nu_\tau$	0.40 ± 0.09	0.77
$\tau^- \to K^-K^+\pi^-\nu_\tau$	0.20 ± 0.07	0.20
$\tau^- \to 3h^-2h^+\nu_\tau$	0.10 ± 0.01	—

Table 2.2: *semi-leptonic τ decays rate with their theorical predictions.*

2.2.2 Theory of semileptonic τ decay

In contrast to the electron and the muon, the τ is heavy enough to decay into hadronic final states, via the weak charged current (figure 2.1.(b)). In the framework of the Standard Model, the W has both vector and axial vector components, and can couple to hadronic states with spin-parity: $J^p = 0^-, 0^+, 1^-$ or 1^+. The general form of semi-leptonic τ decays can be written as[7]:

$$\Gamma(\tau \quad \to \quad hadrons + \nu_\tau) = \frac{G_F^2}{32\pi^2 m_\tau^3}\int_0^{m_\tau - m_\nu} dq^2(m_\tau^2 - q^2)^2 \times$$

$$\Big\{|V_{ud}|^2 \left[(m_\tau^2 + 2q^2)(v_1(q^2) + a_1(q^2)) + m_\tau^2(v_0(q^2) + a_0(q^2))\right] +$$

$$|V_{us}|^2 \left[(m_\tau^2 + 2q^2)(v_1^s(q^2) + a_1^s(q^2)) + m_\tau^2(v_0^s(q^2) + a_0^s(q^2))\right]\Big\} \qquad (2.11)$$

where V_{ud} and V_{us} are the CKM matrix elements, v and a are vector and axial vector spectral functions of the square of the invariant mass of the hadronic states, q^2. The subscripts of these functions denote the spin J of the hadronic system and the superscript s denotes the system with net strangeness (The mass of the τ is below that of charm mesons). The branching fraction is related to the decay width by $B_a = \Gamma_a \tau_\tau/\hbar$.

Since τ decays have low q^2 values, $q^2 < m_\tau^2$, the spectral functions are expected to be dominated by individual resonances. Possible final states are classified in Table 2.3, according to their quantum number.

Spectral function	Spin-Parity	Strangeness	Decay channel
a_0	0^-	0	π^-
a_1	1^+	0	$a_1^-(1260)$
v_1	1^-	0	$\rho^-(770), \rho'(1700)$
a_0^s	0^-	-1	K^-
a_1^s	1^+	-1	$K_1^-(1270), K_1^-(1400)$
v_1^s	1^-	-1	$K^{*-}(892)$

Table 2.3: *Quantum numbers of τ decay channels*

At present the spectral functions can not be calculated because QCD perturbative theory does not work at low energy, but there are several theoretical restrictions on these spectral functions. For example, in the limit of exact $SU(3)_L \times SU(3)_R$ symmetry $v_1 = a_1 = v_1^s = a_1^s$. The Conserved Vector Current (CVC) theorem states that $v_0(q^2) = 0$ and v_1 can be related to the total cross-section of e^+e^- annihilation into hadrons. The Weinberg sum rule[19] provides relations between v_1 and a_1, while the sum rules of Das, Mathor and Okubo (DMO)[20] relate v_1^s and a_1^s.

The CVC theory relates the vector part of the charged weak current to the isovector part of the electromagnetic interaction, which has been measured in the reaction $e^-e^+ \to hadrons$:

$$v_1(q^2) = \frac{q^2\sigma_{I=1}(e^-e^+ \to h)}{4\pi\alpha^2} \qquad (2.12)$$

The simplest example is the decay $\tau \to \rho\nu_\tau$, with a predicted branching fraction $BR(\tau^- \to \pi^-\pi^0\nu_\tau) = 24.4\%$[15]. It is in excellent agreement with the experimental result $BR(\tau^- \to h^-\pi^0\nu_\tau) = 24.36 \pm 0.21\%$[§].

[§] It includes about 0.4% decay of $\tau^- \to K^-\pi^0\nu_\tau$

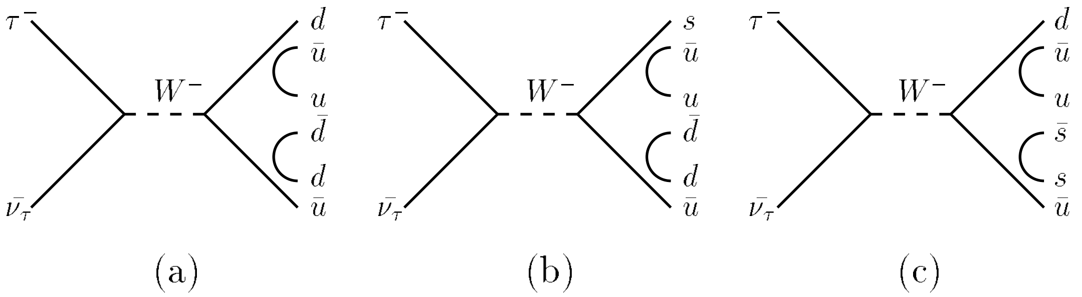

Figure 2.2: *tau decay to 3 charged mesons. (a) $\tau^- \to \pi^-\pi^+\pi^-\nu_\tau$, (b) $\tau^- \to K^-\pi^+\pi^-\nu_\tau$, (c) $\tau^- \to \pi^- K^+ K^-\nu_\tau$.*

The rate for the decay $\tau \to \rho\nu_\tau$ can also be calculated from the spectral function:¶

$$v_1(q^2) = 2\pi(f_\rho/m_\rho)^2\delta(q^2 - m_\rho^2)^4 \tag{2.13}$$

it leads to:

$$\Gamma(\tau \to \rho\nu_\tau) = \frac{G_F^2}{16\pi}|V_{ud}|^2 m_\tau 2(f_\rho/m_\rho)^2(1 - \frac{m_\rho^2}{m_\tau^2})(1 + 2\frac{m_\rho^2}{m_\tau^2}) \tag{2.14}$$

where the decay constant f_ρ characterises the $W - \rho$ interaction.

The τ decays into three charged mesons are illustrated in figure 2.2. Fig 2.2(a) shows the decay into three charged pions, which is the main contribution of the 3 hadron final state. All experimental results agree that the 3π final state is saturated by the $J^P = 1^+$ resonance $a_1(1260)$, decaying to $\rho\pi$.

The $(K\pi\pi)^-$ final state decay can occur via the Cabibbo suppressed weak current(Fig 2.2(b)). Its rate is therefore reduced by roughly a factor of $\tan^2\theta_c \approx 0.05$, compared with 3π decays. The axial-vector current is expected to be dominated by the mixture of the resonances $K_1(1270)$, which decays dominantly to ρK, and $K_1(1400)$, which decays to $K^*\pi$. The equation 2.14 can be used with the appropriate substitutions. The DMO sum rule relates the corresponding masses and couplings:

$$\frac{f_{K_1}^2}{m_{K_1}^2} = \frac{f_{a_1}^2}{m_{a_1}^2} \tag{2.15}$$

The branching fraction for the $K_1(1400)$ is expected to be about 0.5% , and only 4/9 decays to $K^-\pi^+\pi^-$.

¶ In fact the delta function should be replaced by a normalised Breit Wigner lineshape with a mass-dependent width.

Figure 2.2(c) shows the decay of τ into $KK\pi$. This channel is expected to be:

$$\tau \longrightarrow \rho'(1700)\nu_\tau \longrightarrow K^*K\nu_\tau \longrightarrow KK\pi\nu_\tau$$

where ρ' decays dominantly to four pions, while a small fraction leads to K^*K. In the quark model it is explained with the small probability to create a $s\bar{s}$ pair out of vacuum and the suppression by limitation in phase space. The decay rate can be derived with the CVC theory from the cross section $\sigma(e^-e^+ \longrightarrow K^*K)$. A decay rate of only 0.2% is expected.

In summary, the two 3-prong decays of τ with charged kaons are both strongly suppressed. Therefore a good K/π separation is needed to measure the branching ratios. From the quark model (Figure 2.2), we see that in the $\tau \rightarrow K\pi\pi\nu_\tau$ decay the kaon must have the same charge as the parent τ and in the $\tau \rightarrow KK\pi\nu_\tau$ decay the two kaons have opposite charges. This provides a perfect tool to check the results and to reduce the background.

In addition, the kaon has a much higher mass than the pion. Therefore the decay $\tau \rightarrow K^-K^+\pi^-\nu_\tau$ has many advantages to set a limit on the ν_τ mass by studying the invariant mass of the $(K^-K^+\pi^-)$ system. Since at LEP energies the three charged particles are close to each other, a good tracking is needed to have good mass resolution. This subject is not discussed in this thesis.

Chapter 3

Apparatus

3.1 DELPHI

DELPHI, a DEtector with Lepton, Photon and Hadron Identification[21], is a detector operating at the Large Electron Positron collider at CERN. It is exploited by a collaboration of 540 physicists from 53 universities and research institutes. The DELPHI detector is the most intricate of the four LEP experiments. It is a 4π general purpose detector, with special emphasis on particle identification with Ring Imaging Cherenkov (RICH) counters and on precise vertex determination. Most of the detector components provide three-dimensional information with high granularity.

The detector assembly consists of a cylindrical central region, the so-called barrel, and two endcaps (figure 3.1). A superconducting solenoid (radius 2.6 m, length 7.4 m) provides a magnetic field of 1.2 T, enabling a good momentum resolution of the track detectors.

A full technical description of the DELPHI detector can be found elsewhere[21]. In this section only the main characteristics of some sub-detectors are summarised. The RICH detectors will be described in more detail in the next section. A cylindrical coordinate system (r, z, ϕ) with the z-axis along the LEP beam is used to describe the geometry of the detector. In addition, the polar angle θ, with θ=0 along the beam axis, is used to describe intervals of acceptance.

3.1.1 Tracking

Primary and secondary vertices of charged particle tracks are determined with the Microvertex Detector (VTX)[22]. It consists of three concentric layers of silicon microstrip detectors. In its initial configuration the device provided track coordinates only in rϕ, with a measured intrinsic resolution of about 8 μm. Before the 1994 data taking period the inner and outer layers were fitted with double-sided detectors to allow measurements both in rϕ and in z.

The Inner Detector(ID)[23] immediately surrounds the Microvertex Detector. It consists of a jet chamber surrounded by 5 cylindrical MWPC (Multi Wire Proportional Chamber) layers. The MWPC layers provide fast trigger information and a

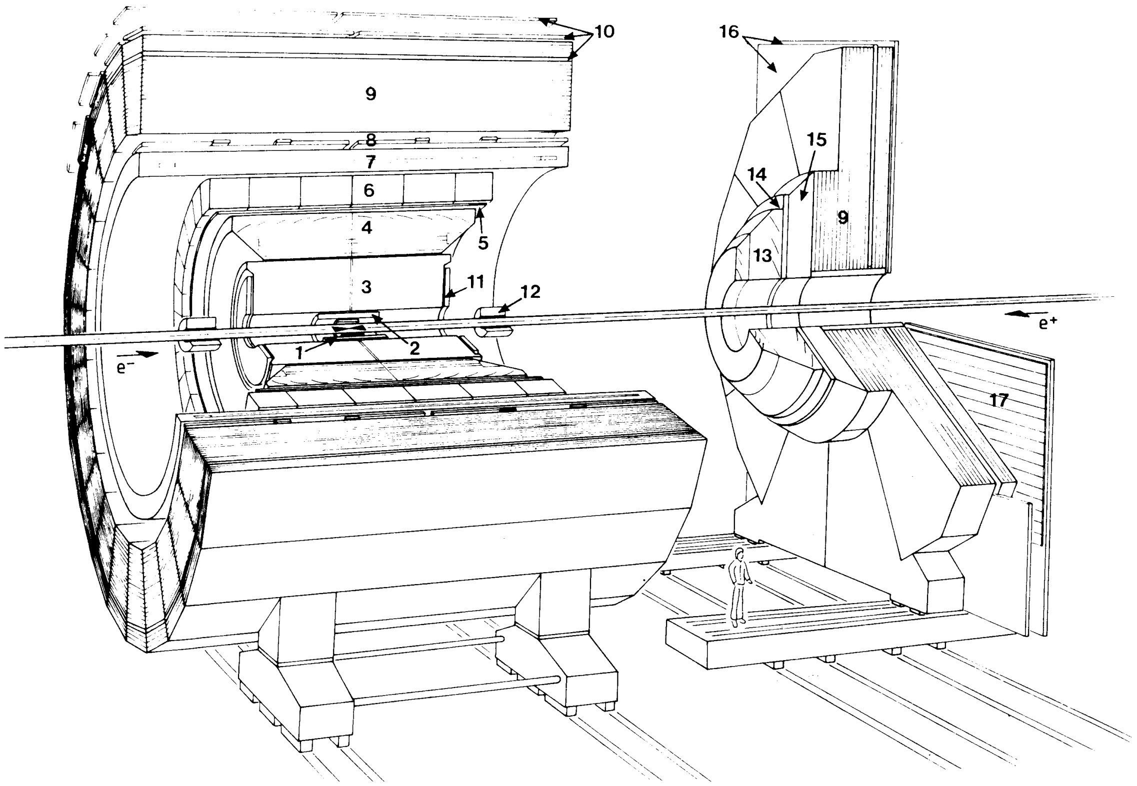

Figure 3.1: *The various parts of DELPHI: Vertex Detector (1), Inner Detector (2), Time Projection Chamber (3), Barrel RICH (4), Outer Detector (5), Hight density Projection Chamber (6), superconducting magnet (7), Time Of Flight (8), Hadron Calorimeters (9), Barrel Muon chambers (10), Forward Chambers A (11), Small Angle Tagger (12), Forward RICH (13), Forward Chambers B (14), Forward Electromagnetic Calorimeter (15), Forward Muon chambers (16), Forward Hodoscope (17).*

stable space point measurement in the z direction. The jet chamber measures 24 rϕ-points per track with a resolution of 90μm per point.

The main tracking device is the Time Projection Chamber (TPC)[24]. The DELPHI pattern recognition normally starts with the information of the TPC. It provides a good 3-dimensional measurement of space points and good two-track separation. Over some momentum range, the specific ionization dE/dX measured in the TPC supports the RICH particle identification. The dimensions of the TPC are r=120 cm and L=2×150 cm, which corresponds to a polar region of acceptance $22^0 < \theta < 158^0$. The resolution per space point is 230 μm in rϕ and 0.9 mm in z. The two-track separation is about 1.5 cm. Combined with other elements of the DELPHI detector, the momentum resolution is given by $\sigma_p/p = 0.0015\ p$ in the barrel and $0.0037\ p$ in the endcap (p in GeV/c).

The Outer Detector (OD)[25] consists of 5 layers of drift tubes located behind the Barrel RICH. It provides fast trigger informations both in rϕ and in z, and it improves the momentum resolution for fast particles. It also provides the tracking information that is important for the hadron identification in the barrel RICH. The position resolution per layer is $\sigma_{r\phi}$=110 μm and σ_z=4.4 cm. Since the Barrel RICH is located between the TPC and the Outer Detector, these two detectors provide the information on position and direction of track elements within the Barrel RICH. For the determination of Cherenkov angles, precision and reliability of tracking information and of Cherenkov photon detection are equally important.

The Barrel Muon Chambers (B-MU) provide muon identification and localisation. The system consists of 6 planes of drift chambers, two inside the return yoke of the magnet after 90 cm of iron and four outside after a further 20 cm of iron. Each chamber measures the rϕ coordinate to 2-3 mm. The resolution in z is about 2.5 cm.

In each of the endcaps, the tracking detectors are the Forward Chamber A (FCA) the Forward Chamber B (FCB) behind the Forward RICH, and the Forward Muon Chamber (F-MU). Information from FCA and FCB is crucial for hadron identification with the Forward RICH.

3.1.2 Calorimetry

The barrel electromagnetic calorimeter of DELPHI is a High-density Projection chamber (HPC)[26]. This sampling calorimeter is essentially a TPC in which lead converter layers alternate with drift channels. Its thickness is 18 radiation lengths. The device measures the three-dimensional charge distribution of electromagnetic showers with very high granularity. The precise imaging of shower development allows discrimination of electrons and photons against hadrons and the identification of π^0's that decay into two nearly parallel photons. To some degree, energy resolution has been traded for spatial resolution. The resolutions in shower direction and in energy are:

$$\sigma_\theta = \frac{36}{\sqrt{E}} + 2.5 \qquad \text{(mrad)}$$

$$\sigma_\phi = \frac{97}{\sqrt{E}} + 10 \qquad \text{(mrad)}$$

$$\frac{\sigma_E}{E} = \frac{23}{\sqrt{E}} + 7 \qquad (\%) \qquad \text{(E in GeV)}$$

The Forward Electromagnetic calorimeter (FEMC) consists of lead glass blocks. It is 20 radiation lengths deep. The energy resolution for bhabhas (E = 45 GeV) is $\sigma_E/\sqrt{E}$=6%.

The Hadron Calorimeter (HAC)[27] is a sampling gas detector incorporated in the magnet yoke. The barrel part covers polar angles between 42.6^0 - 137.4^0 and the two endcaps cover the polar angles between 11.2^0-48.5^0 and 137.5^0-168.8^0. The energy resolution is $120\%/\sqrt{E}$ (E in GeV).

3.1.3 On-line Systems and Off-line Software

The on-line systems concern triggering, data acquisition, slow controls and the supply of detector gases and liquids. The trigger system distinguishes Z^0 decays from background events. This is done sufficiently loosely to ensure that events of interest are not inadvertently rejected. The result is that the data stream written to tape by the Data Acquisition System is strongly enriched in Z^0 events. The slow control system monitors and controls the status of detector components. The fluids system regulates the supply and checks the quality of detector fluids and monitors safety devices.

The off-line software encompasses programme packages for data analysis (DELANA), simulation (DELSIM) and event graphics (DELGRA). From the huge amount of complex data, DELANA reconstructs the event topology, determines the momenta and energies of particles and identifies particle species (muon, electron, pion, etc.). DELSIM is used to generate events of a specific process according to a theoretical model, and to simulate the response of the detector to the final state products. The simulated data are analysed in the same way as the real data in order to check the response of the detector, the analysis program, the quality of the real data and the theoretical model as well. DELGRA visualises the event topology in 3 dimensions. It is used to investigate the performance of the detector and the results of the analysis programme.

DELANA reduces the raw data in combination with parameters from the detector database to Data Summary Tapes (DST). Each DST event carries only information relevant for physics analysis, about the event structure and about the constituent particles. Without loading the database and reprocessing the raw data, it is still possible to carry out minor improvements on DST level by a DST fixing programme. Subsequently a private mini-DST is created with the necessary information on the specific physics subject to perform the final analysis.

3.2 The Ring Imaging Cherenkov detectors of DELPHI

Experimental studies by the Russian physicist P.A. Cherenkov were in 1937 followed by a paper of Frank and Tamm explaining the production mechanism of Cherenkov radiation. The phenomenon has since been used widely in high energy physics for particle identification.

The DELPHI experiment is equiped with Ring Image CHerenkov (RICH) detectors for hadron identification over a large momentum range. This important feature distinguishes DELPHI from other experiments at LEP. The RICH system comprises the Barrel RICH detector in the central region of DELPHI and two endcap detectors which together form the Forward RICH. The development of the DELPHI RICH detectors was initiated by work of Seguinot and Ypsilantis[30]. The development work within DELPHI collaboration has been documented in reference in[31].

3.2.1 Principle of operation

A charged particle moving through a transparent dielectric medium with a velocity v larger than the phase velocity of light in that medium ($=c/n$, where n is the index of refraction) emits radiation under a specific angle with respect to the direction of flight of the particle. The angle between the propagation direction of the particle and the emitted radiation (the Cherenkov angle θ_c) is given by:

$$\cos\theta_c = \frac{1}{\beta n} = \frac{1}{n\sqrt{1-1/\gamma^2}} \tag{3.1}$$

with $\beta = v/c$ and $\gamma = E/mc^2$. Therefore the velocity of a particle could be determined by measuring the Cherenkov angle. With the momentum measured by other detectors, the mass of the particle is determined and the particle, consequently, is identified.

For a particle path length l in the radiator medium, the number of detected photons is:

$$N_{ph} = N_0 l \sin^2\theta_c \tag{3.2}$$

where the quality factor

$$N_0 = 370[cmeV]^{-1}\int_\omega \varepsilon(\omega)d\omega \tag{3.3}$$

takes into account the various multiplicative efficiency factors of the actual detection instrument. The efficiency $\varepsilon(\omega)$ for detection of a photon of frequency ω contains the transmission of windows, mirror reflectivity, the quantum efficiency of the photon conversion mechanism and inefficiencies in the detection of the photo-electrons produced.

Below the threshold velocity $\beta_{th} = 1/n$* no photons are emitted. Slightly above threshold the Cherenkov angle is close to zero. For higher velocities the Cherenkov angle and the number of emitted photons increase quickly, untill β approaches 1 where the Cherenkov angle is at its saturation value $\theta_{c,sat} = \arccos 1/n$ and the number of emitted photons reaches its plateau value.

Both liquid and gaseous radiator media are used in the RICH detectors of DELPHI. The aim of using two types of radiators is to extent the momentum region over

* Dealing with relativistic particles it is often more convenient to use the Lorentz variable:

$$\gamma_{th} = \frac{1}{\sqrt{1-1/n^2}}$$

Radiator	Boiling temp.[^{0}C]	n at $7eV$	$\frac{\Delta n}{n-1}(6.5-7.5eV)$	γ_{thr}	$\theta_{c,sat}[^0]$
C_4F_{10}	-1.7	1.00153	2.0%	18.1	3.17
C_5F_{12}	28 (1.0 atm.)	$1.00176(40^0C)$	2.9%	16.9	3.40
	35 (1.3 atm.)	$1.00229(40^0C)$		14.8	3.87
C_6F_{14}	57	$1.283(40^0C)$	3.0%	1.60	38.77

Table 3.1: *Properties of the radiators*[28][29]

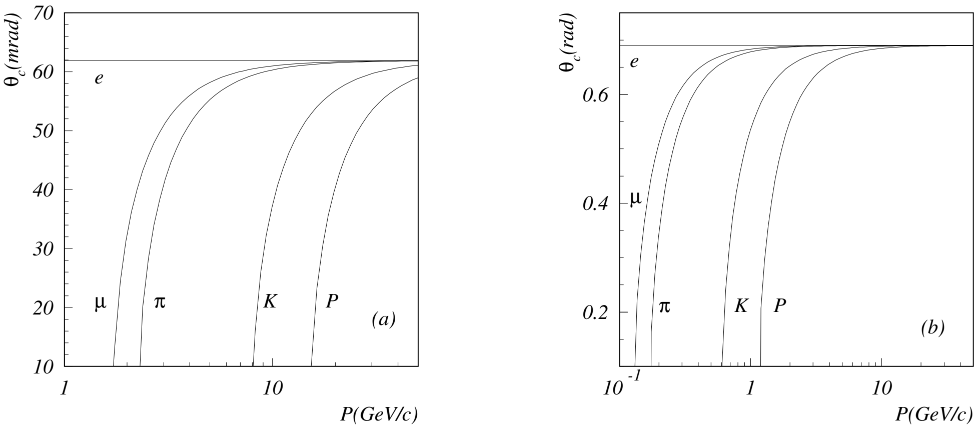

Figure 3.2: *Cherenkov angle as a function of momentum for different types of particles. (a) in the gas radiator C_5F_{12}. (b) in the liquid radiator C_6F_{14}.*

which particles can be identified. The selected radiator substances are all perfluorocarbons. Perfluorohexane, C_6F_{14}, is used as liquid radiator for both RICHes, while the gas radiators are perfluoropentane, C_5F_{12}, and perfluorobutane, C_4F_{10}, in the Barrel and Forward RICH, respectively. The properties of these substances are given in Table 3.1. The gas radiator is used for high momentum particles, the liquid for lower momenta. Figure 3.2 shows the Cherenkov angle as a function of the particle momentum for different types of particles, both in gas and in liquid radiators. The power of particle identification is determined by the separation between the particle bands in fig. 3.2 in units of the resolution on the Cherenkov angle.

The uncertainty on the Cherenkov angle determination from individual photons, σ_{ph}, is given by the quadratic sum of several error sources. For the photons from the gas radiator one has:

$$\sigma_{ph}^2 = \sigma_{chrom}^2 + \sigma_{bend}^2 + \sigma_{position}^2 \tag{3.4}$$

where σ_{chrom} is due to chromatic aberration, i.e. the variation of the refractive index with photon energy. The term σ_{bend} is caused by the bending of the particle trajectory in the 1.2 T magnet field of DELPHI, which smears the Cherenkov angle

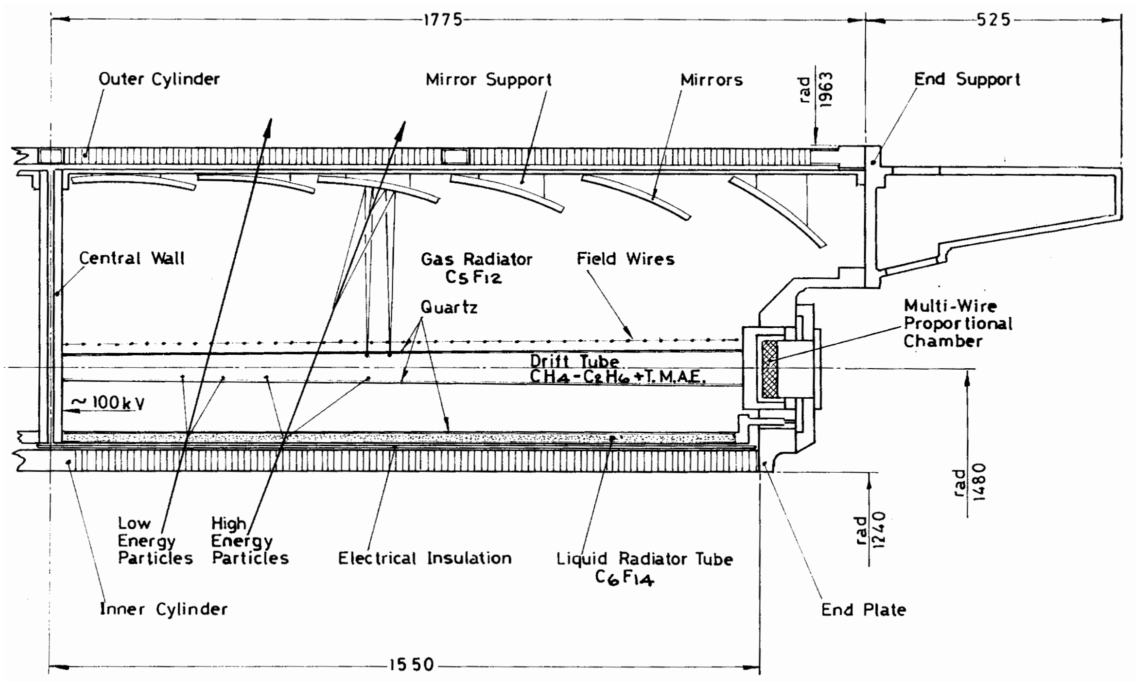

Figure 3.3: *Longitudinal view of a quarter of the barrel RICH*

in one direction. It depends on the transverse momentum of the particle ($p \sin\theta_p$), the track length (l) inside the gas radiator and the azimuthal position of the photon (ϕ) on the Cherenkov cone:

$$\sigma_{bend} \propto \frac{l|\sin\phi|}{p\sin\theta_p} \tag{3.5}$$

Finally, $\sigma_{position}$ is due to the finite position resolution of the photon detector. It includes diffusion during the drift of photo-electrons and the intrinsic resolution of the wire chambers which detect the photo-electrons.

For photons from the liquid radiator, the term σ_{bend} is replaced by a term σ_{geom} which represents a spread in the size of the Cherenkov image on the photon detector plane, due to the finite depth of the liquid radiator layer.

3.2.2 The Barrel RICH

The Barrel RICH (BRICH)[32] is a 3.5 m long cylinder with inner and outer radii of 130 and 197cm respectively. A mid-wall divides the detector volume into two identical halves, referred to as sides A and C. It covers the polar angular region from 40^0 to 140^0.

Each side of the BRICH is azimuthally divided into 24 sectors. The elements of a sector are one liquid radiator, one drift tube with a wire chamber at its end, and 6 mirrors. An undivided gas radiator volume is common to all sectors (see figure 3.3).

The liquid radiators consist of a 1 cm thick layer of C_6F_{14}. They are mounted close to the inner cylinder. Cherenkov photons from the liquid radiators are directly incident on the drift tubes, placed 12 cm behind the liquid radiators. The whole vessel is filled with the gaseous radiator C_5F_{12}. The average path length of particles in the gas volume is 40cm. Cherenkov light from the gas radiator is projected as ring images onto the drift tubes by parabolic mirrors The mirrors are mounted on the outer cylinder of the BRICH. For convenience in the analysis, all mirrors at the same distance from the interaction point are grouped together. Error calculus is the same for photons reflected by any mirror of group **i** (**i**=1,···,6; group 1 is close to the mid-wall).

The set of drift tubes forms the photon detector of the BRICH. The tubes are constructed from UV grade quartz plates and contain a gas mixture of $75\%CH_4$ $+25\%C_2H_6$. The drift gas is made photosensitive by bubbling through liquid TMAE†, which has an ionization potential of 5.4 eV. A drift field of 0.5 kV/cm transports the photo-electrons towards a Multi Wire Proportional Chamber (MWPC) at the end of the drift tube. Each MWPC has 196 anode wires at 2.62 mm pitch and 196 cathode pads at 4 mm pitch. The chambers are operated at a gas amplification of about 3×10^5. Photo-conversion points are reconstructed in three dimensions. The anode wire address provides the rϕ coordinate and the cathode pad address gives the **r** coordinate. The z coordinate is determined by the drift time. Combined with the position and the direction of the particle measured by the tracking detectors of DELPHI, the Cherenkov angle can be calculated for each photon.

The calibration system of the BRICH injects UV light into each drift tube at 45 accurately known points, arranged as 5 rows of 9 fibers. It provides a determination of the drift velocity at 0.1% accuracy and allows us to follow any changes in the drift velocity during data taking due to variations of temperature, pressure, gas mixture etc.

The performance figures of the BRICH for muon pairs at 45.6 GeV are: in the liquid and gas radiators the number of photons per ring is 11 and 8.5; per individual photon the resolution on the Cherenkov angle is 14 and 4 $mrad$ with the saturated angle 670 and 61 $mrad$, respectively.

3.2.3 The Forward RICH

The Forward RICH (FRICH)[33] covers both end-cap regions of DELPHI over polar angles $15^0 < \theta < 35^0$ and $145^0 < \theta < 165^0$. Although very different in geometry, it employs the same principles as the Barrel RICH. A major practical difference is that in the FRICH the electric drift field in the photon detector is perpendicular to the magnetic field of DELPHI.

The FRICH combines a layer of liquid radiator, C_6F_{14}, and a volume of gaseous C_4F_{10} into a single assembly. The general layout is shown in figure 3.4. Each of the two end-caps is divided azimuthally into 12 modular sectors. Each sector contains one drift box, two MWPC's, three liquid radiator containers and five spherical mir-

† Tetrakis(dimethylamino)-ethylene

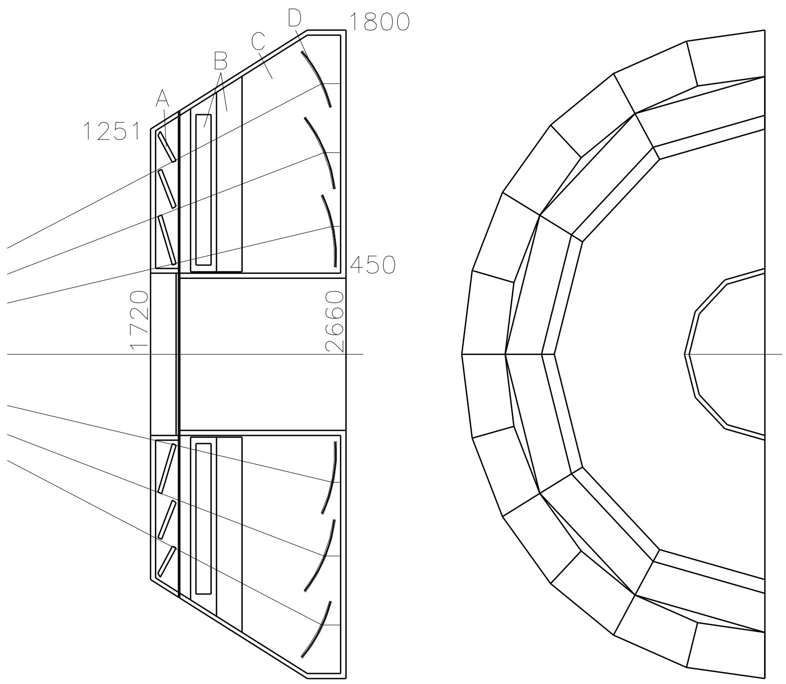

Figure 3.4: *Schematic view of the Forward RICH (dimensions in mm): A=liquid radiator, B=photon detector with the MWPC (see fig. 4.1), C=gas radiator, D=mirror.*

rors. The gas radiator fills the entire remaining volume of the vessel. The average path length inside the gas radiator is about 60cm.

The photon detector is built from trapezoidal TPC units (drift boxes) spanning 30^0 in azimuth. Each drift box is symmetrically divided into two halves with an electric drift field orthogonal to the radial edges where the MWPCs are located. The two sides of the drift box are made of quartz plates. The drift gas is C_2H_6 which is bubbled through liquid TMAE at 24^0C, which provides a photon absorption length a about 2 cm. Photo-electrons drift towards the read-out chambers under the combined action of the mutually orthogonal electric drift field ($E = 1KV/cm$) and the DELPHI magnetic field ($B = 1.2T$).

The electronics chain provides digitised time information for signals on each anode wire and cathode strip of the MWPC. The preamplifiers are mounted inside the MWPC assembly. The output signals are received by Amplifier-Discriminator-MUltipleXer(ADMUX) fastbus units, in which each signal is individually amplified and discriminated against an ajustable threshold. At the end of the signal acquisition chain, LEP Time Digitizer modules provide time digitization in 10 ns buckets.

With the UV calibration system, the drift velocity and Lorentz angle are measured precisely. The drift calibration will be discussed in detail in chapter 4.

A quarter of the FRICH was installed and operated in 1992. The full FRICH has been installed before the 1993 LEP run and has since then successfully taken data. The performance figures of the FRICH for muon pairs at 45.6GeV are: for the liquid and gas radiators the number of detected photons per ring is 7.8 and 10.8 respectively; the resolution on the Cherenkov angle for individual photons is 11.4 and 2.8 $mrad$ with the saturated Cherenkov angle 670 and 58 $mrad$ respectively.

3.2.4 K/π separation with the RICH

The most important aim of the RICH analysis is to distinguish kaons from pions. (Discrimination of hadrons against leptons is already provided for by other detector systems in DELPHI.) Especially in τ physics, the kaon production is only 2% compared with pion's.

Two technigues are used for kaon identification with the gas radiator. Below $\sim$9 GeV/c, the kaons are below the threshold for producing Cherenkov photons, while the pions yield a nearly saturated angle and the maxium number of Cherekov photons. In this momentum range kaons are identified by "Veto Identification", i.e. by requiring that no photon-electrons are associated with the particle. Below 4 GeV/c the Cherenkov angle and the number of photons radiated by pions starts to decrease, and the probability of kaon misidentification therefore increases.

Above the kaon threshold of $\sim$9 GeV/c, the Cherenkov angle is determined from the detected Cherenkov photons. The kaon is identified by requiring that the measured Cherenkov angle is compatible with the kaon hypothesis but is incompabtible with the (π,μ) hypothesis. This is called "Ring Indentification". It allows kaon identification up to 20 GeV/c in the BRICH and up to nearly 40 GeV/c in the FRICH.

Chapter 4

On-line Calibration of the Forward RICH

The photo-ionising additive TMAE in the RICH drift gas provides for efficient conversion of Cherenkov photons into free electrons, which then drift towards an MWPC. The Cherenkov angle of a particle is determined from the space points where photo-conversion occurred. The three coordinates of each conversion point are obtained from the addresses of anode and cathode signals in the MWPC and the drift time. For a precise measurement, the drift velocity and drift trajectory must be known accurately. Therefore, on-line calibration and monitoring systems of drift constants have been installed on the Barrel and Forward RICH. In the Barrel RICH, where the drift field is parallel to the magnetic field of the DELPHI detector, the drift direction is to very good approximation perpendicular to the MWPC wire plane. The x, y and z coordinates as defined within a given drift tube simply correspond to the anode wire address, cathode strip address and drift time coordinate, respectively. In the Forward RICH the situation is more complicated, because here the photo-electrons drift in a plane perpendicular to the 1.2 T magnetic field. Therefore, not only the drift velocity has to be measured precisely but also the Lorentz angle between drift trajectory and the electric field. Since this makes the calibration of the FRICH more complicated than that of the BRICH, we discuss the calibration of drift constants for the case of the FRICH.

4.1 UV calibration system of the FRICH

The calibration system of the FRICH is shown in figure 4.1. Ultraviolet light is fed into 22 quartz (pointing) fibres of 100 μm diameter, that are placed inside cylinders of G10 material mounted equidistantly on both sides of the midwall of the drift volume. Each light spot is produced through a 0.5 mm diameter collimator at the end of the cylinder. Two alignment fibres near each MWPC allow the determination of the position of the MWPC . The positions of these "fiducial" photon sources in the drift tube system (measured with 30 μm precision after the installation of the fibre system on the drift volume), deviate less than 200 μm from their nominal values. The UV lamp is a hydrogen flash lamp developed especially for this system. They are running at a frequency of 150 Hz when calibration data are taken.

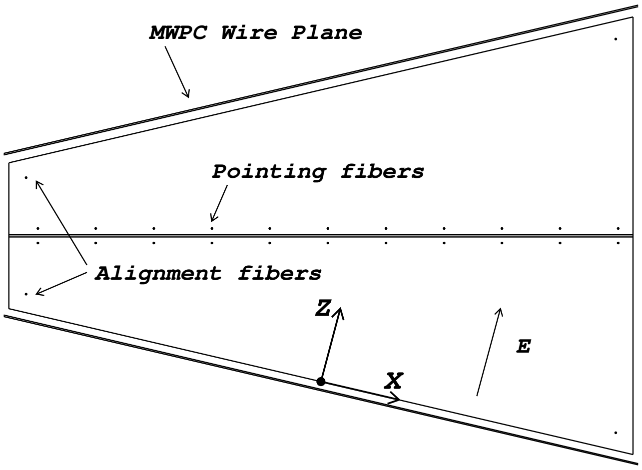

Figure 4.1: *Drift tube and calibration/monitoring system of the FRICH.*

To determine the drift velocity and the Lorentz angle, the following model of the movement of the photo-electron is adopted (figure 4.2): The photo-electron is produced at A. When the magnet is off, the drift path to the MWPC wire plane follows the electric field: from A to B to C. When the magnet is on, it follows the path AD inside the drift volume with a drift velocity V_d and Lorentz angle θ_L. Inside the MWPC it follows the path DE with a saturated drift velocity V_s and a saturated Lorentz angle θ_s.

The FRICH runs the calibration system outside normal data taking. Calibration data were taken both with and without magnetic field. The drift velocity and the Lorentz angle in the drift volume are parameterised as functions of temperature and pressure, while the saturated values V_s and θ_s are kept fixed.

The pointing fibres are numbered from 1 to 11 with the fibre 1 close to the small end of the drift box. The reference frame used is shown in figure 4.1, which is the same as the local coordinate system used in the off-line analysis. The measured position of each light spot is given in table 4.1.

In our analysis the following conversion factors are used:

Wire spacing = 0.262 cm
1 LTD count = 0.01 μsec

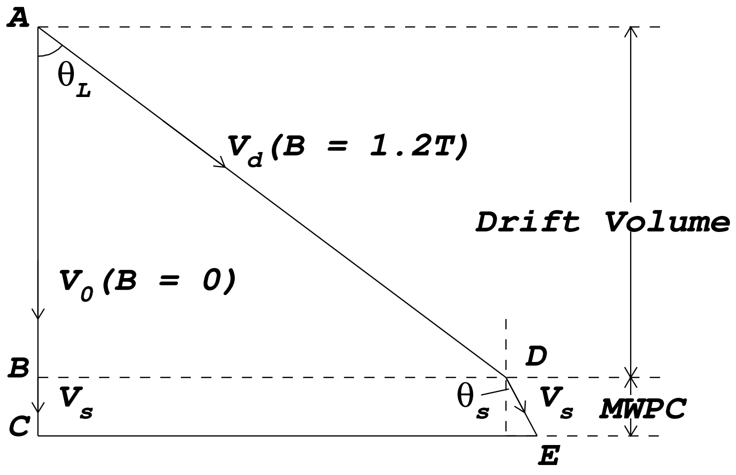

Figure 4.2: *The photo-electron movement in the FRICH.*

Light Spot		Coordinates X_s (cm)	Coordinates Z_s (cm)	Magnet off Wire (WIRE)	Magnet off Time (Count)	Magnet on Wire (WIRE)	Magnet on Time (Count)
Pointing fibers	1	-38.49	10.51	11.85	204.1	63.14	334.3
	2	-31.28	12.31	39.70	238.2	98.91	389.1
	3	-24.06	14.10	67.02	270.8	113.64	443.7
	4	-16.84	15.90	94.68	303.7	170.27	497.0
	5	-9.62	17.71	122.29	337.3	205.96	551.7
	6	-2.04	19.50	149.38	371.7	241.94	606.8
	7	4.81	21.30	177.35	404.4	277.90	662.5
	8	12.02	23.10	204.90	438.1	314.33	720.8
	9	19.23	24.90	232.33	471.3	-	-
	10	26.45	26.70	260.07	505.2	-	-
	11	33.66	28.50	288.07	539.9	-	-
Ali.	1	-36.82	2.10	-	-	31.22	78.5
	2	36.68	2.11	-	-	311.46	77.0

Table 4.1: *Coordinates of each fiber and a sample of their measured positions.*

4.2 Calibration Results

4.2.1 Data Selection

In a calibration run, a few hundred data points are taken for each spot. To reduce the noise, a signal is retained if the time match between the cathode and its adjacent anode is less than 50 ns (figure 4.3). Figure 4.4 displays a scatter plot of photons from a calibration run (magnet is on) seen with one MWPC. The light spots from pointing fibres and alignment fibres are clearly visible with almost no background.

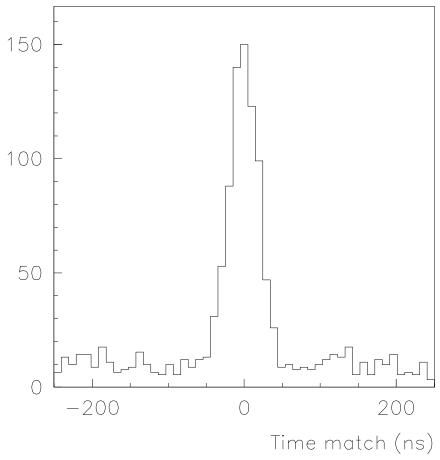

Figure 4.3: *The time difference between cathode and anode signals*

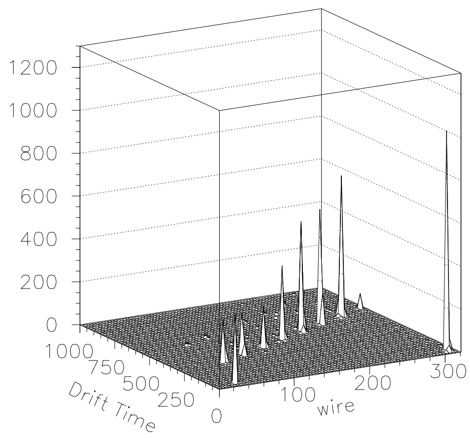

Figure 4.4: *UV light spots*

A gaussian fit was made to determine the position of each spot in wire and time coordinates (figure 4.5). The wire and time distributions have typical widths of $\sigma = 0.9$ wire spacings and $\sigma = 2.6$ LTD counts respectively.* Table 4.1 lists the coordinates of the pointing fibres in the coordinate system shown in figure 4.1 and the measured position of each spot in "wire" and "time" direction. The positions of the alignment fibres can not be reconstructed well without magnet because of the electronic noise. When the magnet is on, the pointing fibres 10 to 11 are out of acceptance for odd numbered chambers while the fibres 1 to 3 are out of acceptance for even numbered chambers.

Some spots are rejected because the position is not well determined. This may happen if there are not enough data points (in our analysis more then 80 data points are required) or if there is no good gaussian fit because of high electronic noise. The criteria for a good gaussian fit were:

- χ^2 per degree of freedom is less than 5
- The standard deviation of the wire distribution is less than 1 wire.

* Without magnetic field they are 0.5 wires and 1.7 LTD respectively, due to the shorter drift distance(figure 4.6).

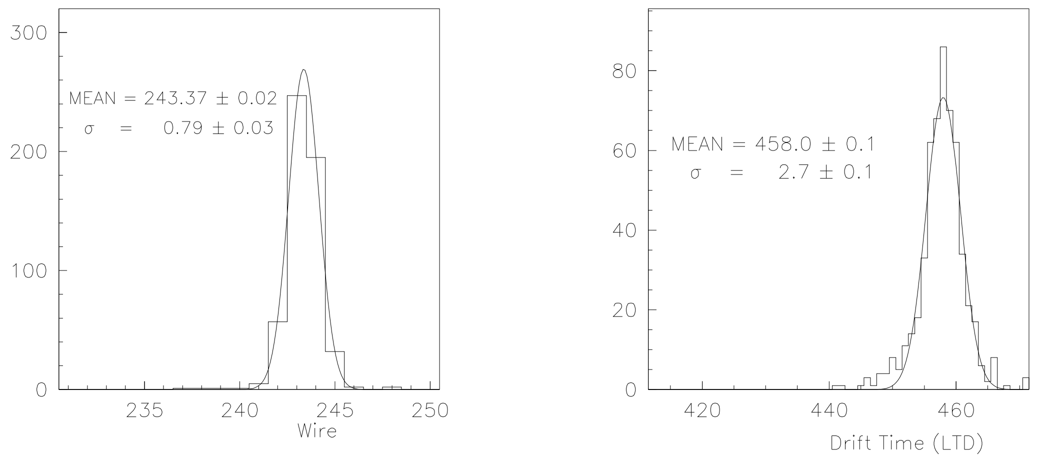

Figure 4.5: *Typical Gaussian fits on both wire and time distribution (B=1.2T) for all measured light spots.*

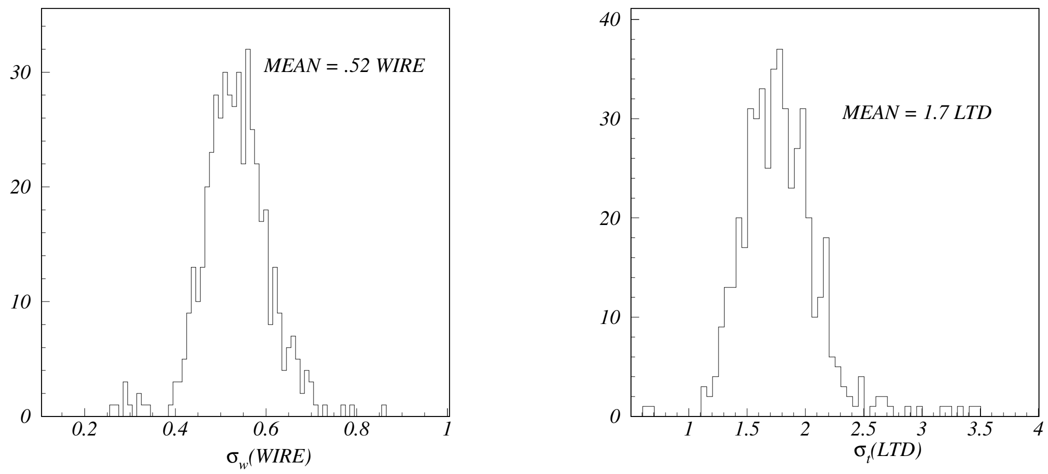

Figure 4.6: *The width of light spots in wire and time coordinates (B= 0.0T).*

- The standard deviation of the time distribution is less than 5 LTD counts.

One typically obtains wire coordinates and drift times with errors of about 0.2 mm and 2 ns respectively. On average 10.5 good spots per sector are seen for magnet off and 9 for magnet on.

4.2.2 Determination of Drift velocity and Lorentz angle

According to the model of photo-electron movement mentioned in the previous section, the following quantities should be determined from calibration for each MWPC and the drift volume it subtends:

T_0:	the sum of all time delays in trigger, cables and electronic units.
X_0:	the offset of the positioning of the MWPC module in the x-direction (see figure 4.2). For conformity with the off-line analysis, the origin of the x-coordinate is taken at the nominal position of wire address 160.5, which lies halfway along the MWPC. In the presence of an offset X_0 in units of wire spacing, the origin falls at wire address $160.5 + X_0$.
α:	the angle between the wire plane of the MWPC and the radial edge of the drift box, due to inprecision in its construction.
V_0:	the drift velocity when the magnet is off.
V_s, θ_s:	the saturated drift velocity and Lorentz angle inside the MWPC.
V_d, θ_L:	the drift velocity and Lorentz angle with the magnet on.

We denote by $X_s(i)$ and $Z_s(i)$ the coordinates of each light spot **i**. Light injected at spot **i** arrives after a time $t_0(i)$ at wire address $x_0(i)$ if the magnet is off. The corresponding quantities with magnet on are $t_1(i)$ and $x_1(i)$ (see Table 4.1). We recall that the wire spacing is 0.262 cm. The depth d of the MWPC (i.e. the distance between the points B and C in figure 4.2) is 0.86 cm.

With magnet off one has the relations:

$$t_0(i) = \frac{Z_s(i)}{V_0} + \frac{d + X_s(i)\tan\alpha}{V_s} + T_0 \tag{4.1}$$

$$x_0(i) = \frac{X_s(i)}{0.262} + 160.5 + X_0 \tag{4.2}$$

where $x_0(i)$ is expressed as a wire address. With magnet on the corresponding relations are:

$$t_1(i) = \frac{Z_s(i)}{V_s\cos\theta_L} + \frac{d + (X_s(i) + Z_s(i)\tan\theta_L)\tan\alpha}{V_s\cos\theta_s} + T_0 \tag{4.3}$$

$$x_1(i) = \frac{X_s(i) + Z_s(i)\tan\theta_L}{0.262} + \frac{(d + (X_s(i) + Z_s(i)\tan\theta_L)\tan\alpha)\tan\theta_s}{0.262} + 160.5 + X_0 \tag{4.4}$$

The calibration procedure consists of minimising the difference between arrival times and wire addresses calculated from relations (4.1)-(4.4) and their measured values. Thus, a global fit was made in which we minimise the sum:

$$\sum_{allspots}^{B=0}\left[\left(\frac{t_{m0}(i)-t_0(i)}{\sigma_t}\right)^2+\left(\frac{x_{m0}(i)-x_0(i)}{\sigma_x}\right)^2\right]$$

$$+\sum_{allspots}^{B=1.2}\left[\left(\frac{t_{m1}(i)-t_1(i)}{\sigma_t}\right)^2+\left(\frac{x_{m1}(i)-x_1(i)}{\sigma_x}\right)^2\right] \qquad (4.5)$$

where t_{m0}, x_{m0}, t_{m1} and x_{m1} are measured positions. The quantities σ_t (=4 ns) and σ_x (=0.4 mm) are the r.m.s. deviations of the light spot positions from their nominal values in "time" and "wire" direction.

In this global fit, the sum is not sensitive to the quantities V_s and θ_s. Since they do not change with time, we measured them with other methods and fixed them in the global fit , decreasing the error of the fit.

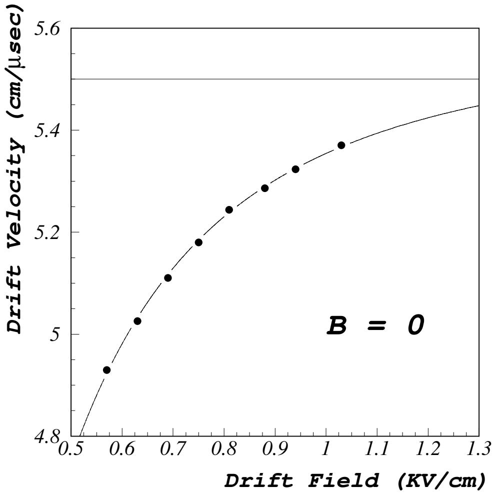

Figure 4.7: *Drift velocity versus drift field without magnetic field.*

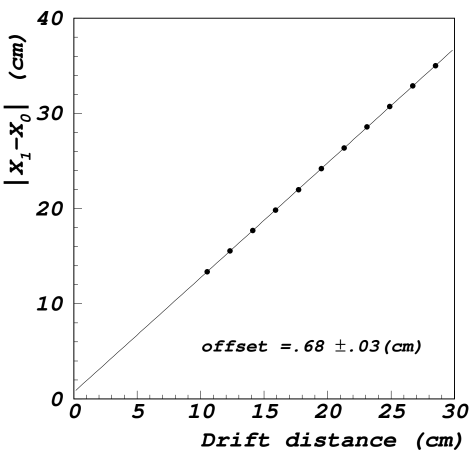

Figure 4.8: *Measurement of the saturated Lorentz angle*

Saturated drift velocity, V_s

To determine V_s we use a drift field scan with magnet off. Herein the drift field varies from 0.55 KV/cm to 1.03 KV/cm. The drift velocity was determined from a linear fit to the measured times versus the drift distances. Figure 4.7 shows the drift velocity as a function of the drift field, in good agreement with other measurements. Inside the MWPC the drift field is about 2 KV/cm, therefore 5.5 cm/μs was found to be a good approximation for the saturated drift velocity.

Saturated Lorentz angle, θ_s

To measure θ_s, we make a linear fit of $x_1(i) - x_0(i)$ as a function of the distance Z_s. Subtracting the equation 4.4 from equation 4.2, and using the standard value $\alpha = 0$, we get:

$$x_1(i) - x_0(i) = \frac{Z_s(i)\tan\theta_L}{0.262} + \frac{d\tan\theta_s}{0.262}$$

Therefore, the saturated Lorentz angle could be calculated from the offset term of the fit. We take the average of $x_1(i) - x_0(i)$ from all chambers. The result of the fit is shown in figure 4.8. We get $\theta_s = 26 \pm 1^0$.

With the fixed values of V_s and θ_s, the global fit was made with MINUIT software. For a good fit the spots with residuals bigger than 2 wire spacings or 6 LTD counts were removed. As an example figure 4.9 shows the measured drift velocity and Lorentz angle as a function of sector number. The accuracies of 0.2% and 0.4% were achieved for the drift velocity and Lorentz angle respectively.

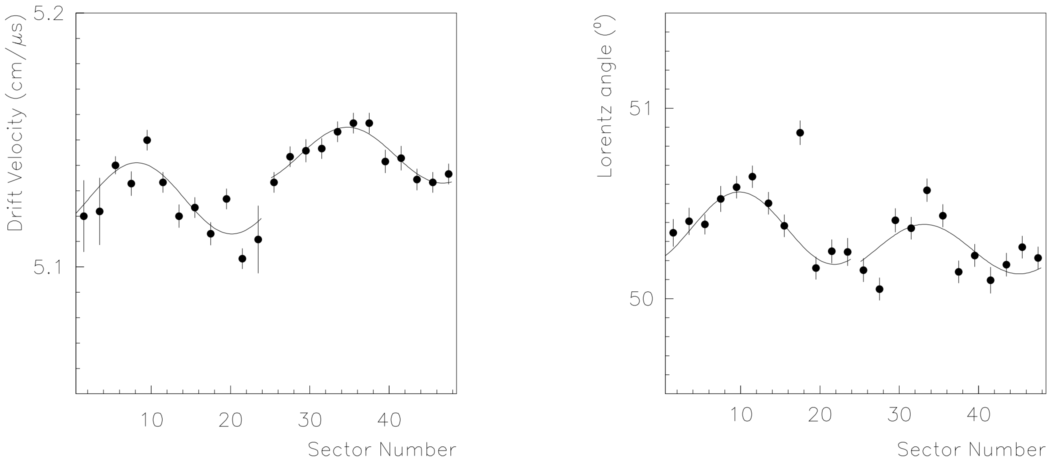

Figure 4.9: *Measured Drift Velocity and Lorentz angle as a function of sector number. The maximum/minimum of the curves correspond to location in the top/bottom part of the FRICH. It could be understood as due to a temperature difference.*

4.3 Monitoring

With the UV calibration system, some other properties of the FRICH could be measured.

4.3.1 High Voltage on the MWPC modules

To measure the MWPC efficiency plateau, a HV scan was made where the HV of the MWPC varied from $1.30kV$ to $1.65kV$. There are two ways to count the signals from the UV light: 1) the number of matched anode and cathode hits per trigger and 2) the number of fibres from which a signal is observed per trigger. The efficiency plateau is shown in figure 4.10. It is apparent that method 1 leads to spuriously high rates at the highest voltage settings, caused by electronics cross talk or by feedback photons. With method 2 the onset of the plateau is observed at $1.5kV$ and at $1.6kV$ good efficiency is achieved.

4.3.2 Discriminator thresholds

In the FRICH the thresholds of the discriminators may be varied from $4mV$ to $50mV$. They are defined by the ADC's in the ADMUX modules, and could be set by computer control. A scan was made to determine the appropriate threshold setting. The result is shown in figure 4.11 for the two counting methods mentioned above . A threshold of 50 ($\sim$ $15mv$) is a reasonable working point, where most of the noise signals are cut away.

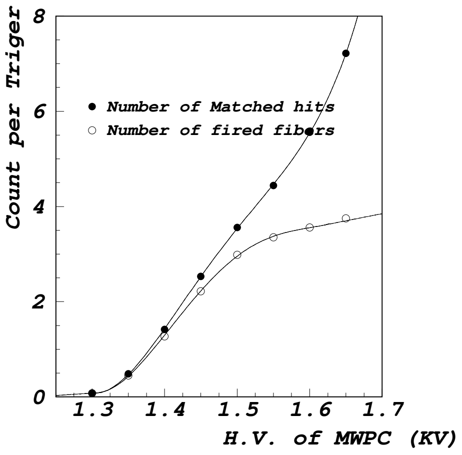

Figure 4.10: *The MWPC efficiency plateau*

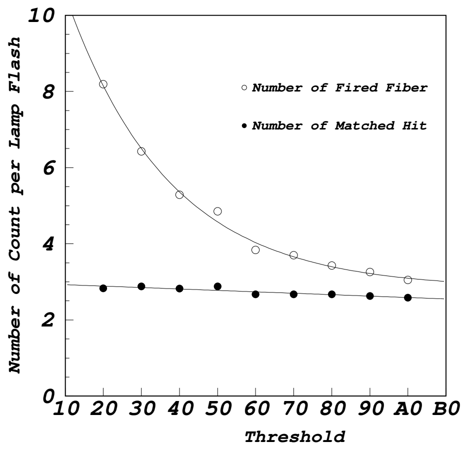

Figure 4.11: *Threshold scan*

4.3.3 Absorption of UV light in TMAE

The drift gas ethane is saturated with TMAE by bubbling it through liquid TMAE in a temperature controlled vessel. Therefore, the absorption coefficient μ ($=\lambda^{-1}$)

varies with the absolute temperature of the bubbler†:

$$\lambda = 0.1(cm)e^{2.966-5614(\frac{1}{300}-\frac{1}{T})} \tag{4.6}$$

To measure the conversion length λ with the UV calibration data, we count the number of matched hits on each cathode strip layer (figure 4.12), corresponding to the depth of the converted photon in the drift volume. The strip pitch is 0.5 cm. An exponential fit was made from layer 3 to layer 11. The result is λ=3.6 cm. These data were taken in 1992 when the temperature of the bubbler was kept at 16.5^0. It agrees with the calculation from the equation 4.6, which gives λ=3.7 cm.

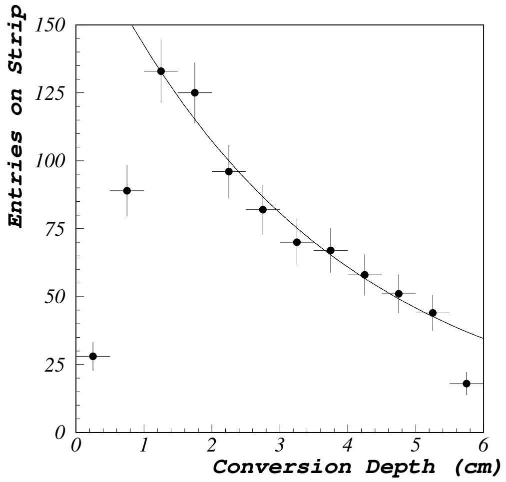

Figure 4.12: *Conversion length of TMAE*

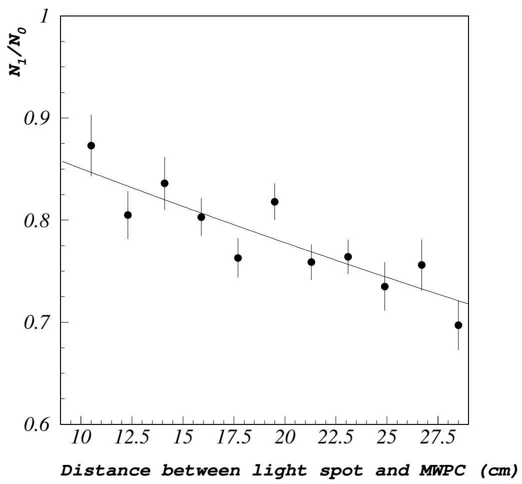

Figure 4.13: *Attenuation length*

4.3.4 Attenuation length of photo-electron drift

The electron attenuation length λ_{att} is measured by counting the number of events, recorded by the wire chamber, as a function of the drift distance. An exponential curve describes the number of counts as a function of the drift distance z:

$$N_i = N_t \varepsilon_i \exp(-\frac{z_d}{\lambda_{att}}) \tag{4.7}$$

where N_i is the number of counts from spot i, N_t is the number of UV flashes, z_d is the drift distance, and ε_i is a coefficient that accounts for the light output (number of photons per trigger) and for electronic noise. Since the unknown coefficient ε_i is quite different for different fibres, we compare the data with magnet on with the

† From the off-line simulation programme

data obtained with magnet off. From equation 4.7 we get the ratio:

$$R_i = \frac{N_{i0}}{N_{i1}} = \frac{N_{t0}}{N_{t1}} \exp \frac{Z_i}{\lambda_{att}} (1 - \frac{1}{\cos \theta_L})$$

where N_{i0} and N_{t0} are the number of MWPC counts and the number of UV lamp triggers when the magnet is off. The corresponding quantities in the measurement with magnet on are N_{i1} and N_{t1}, and Z_i is the distance between light spot **i** and the MWPC. To reduce counts due to electronic noise we count the leading photo-electrons instead of the number of matched hits.

The ratios R_i were measured for all light spots and an exponential fit was made (figure 4.13). The result is $\lambda_{att} = 48 \pm 3$ cm with $\theta_L = 50^0$.

4.3.5 Drift diffusion

The photo-electron image of the light spot spreads with drift distance Z, because of diffusion during drift. One may write:

$$\sigma^2 = \sigma_0^2 + \sigma_{0d}^2 Z$$

where σ_0 is a constant that accounts for the width of the light spot and for the intrinsic position resolution of the measurement. The quantity σ_{0d} is the diffusion coefficient.It was measured in both "wire" and "time" direction. The standard deviations of the Gaussian fits shown in figure 4.5 were used as estimates of the quantity σ in the two directions. Figure 4.14 shows the linear fit of its square against drift distance Z. The results are listed in table 4.2. They are in agreement with the values found in many other experiments.

		B=0	B=1.2 T
WIRE	$\sigma_0(mm)$	1.10 ± 0.02	1.19 ± 0.03
	$\sigma_{0d}(mm/\sqrt{m})$	2.0 ± 0.1	2.8 ± 0.1
TIME	$\sigma_0(mm)$	0.73 ± 0.05	0.96 ± 0.14
	$\sigma_{0d}(mm/\sqrt{m})$	1.4 ± 0.2	2.2 ± 0.5

Table 4.2: *Diffusion of the photo-electron in the FRICH drift tube(The drift voltage is 1.03 KV/cm).*

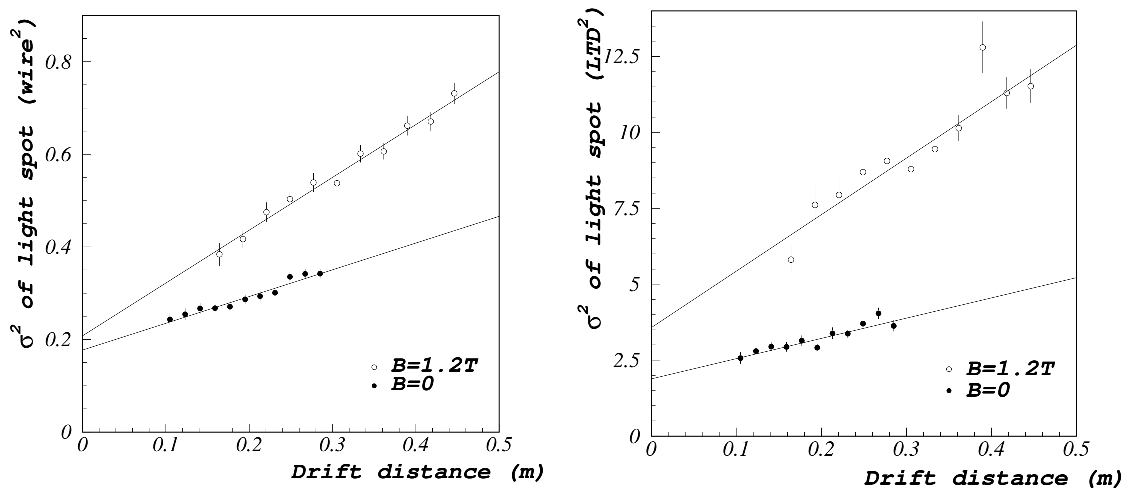

Figure 4.14: *Drift diffusion*

4.4 Summary and Discussion

The measurements of drift velocity and Lorentz angle at our operating point (drift field of 1.03 kV/cm) and at lower drift fields are listed in Table 4.3 for magnetic fields B=0 and B=1.2 T. The drift velocity and the Lorentz angle are related by[34]: $V_d = k(E_d/B)\sin\theta_L$. The factor k depends on the velocity distribution and on the collision cross section of the drifting electrons. It is expected to approach a constant value at small drift fields. In figure 4.15 the measured values $k \equiv V_d B/(E_d \sin\theta_L)$ have been plotted against the reduced drift field E_d/N, where N is the molecular density of the gas. The data points closely follow the calculated curve provided by ref.[35]. The calculation proceeds from ethane cross sections, using a multi-term solution of the Boltzmann equation for crossed E an B fields[36].

The calibration data were taken at known temperature and gas pressure. Therefore, the drift velocity and Lorentz angle could be parameterised as a function of pressure and temperature. Since variations are small, linear fits were made of V_d and θ_L against P/T (figure 4.16). It is found that V_d changes with P/T while $\sin\theta_L/V_d$ is a constant. We obtain

$$\frac{\sin\theta_L}{V_d} = 0.1493$$

and for the drift velocity we get the relation:

$$V_d = V_0(1 + 0.43(\frac{P_0}{T_0} - \frac{P}{T}))$$

Drift Field	B = 0	B = 1.2 T	
(kV/cm)	$V_0(cm/\mu sec)$	$V_d(cm/\mu sec)$	$\theta_L(^0)$
1.03	5.37	5.12	49.8
0.97	-	5.03	51.3
0.94	5.32	4.95	51.9
0.88	5.29	4.83	53.6
0.81	5.24	4.68	55.2
0.75	5.18	4.49	56.6
0.69	5.11	4.27	58.3
0.63	5.03	4.06	59.6
0.57	4.93	3.78	60.9

Table 4.3: *Drift velocity and Lorentz angle in ethane both with and without magnet field*

where P_0 = 975mbar and T_0 = 307.5K and V_0 is the corresponding drift velocity.

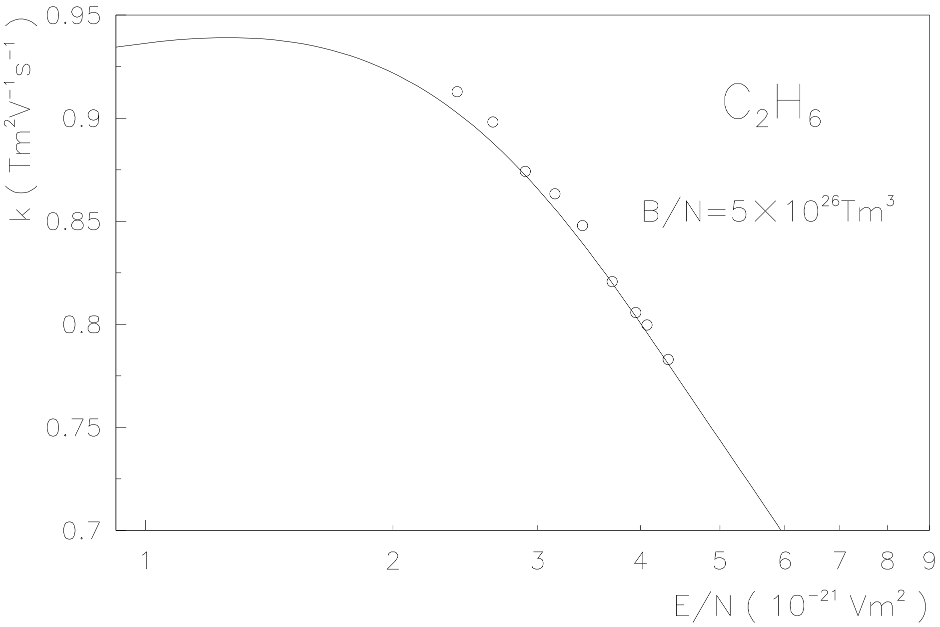

Figure 4.15: *The quantity* $k \equiv V_d B/(E_d \sin\theta_L)$ *versus the reduced drift field*

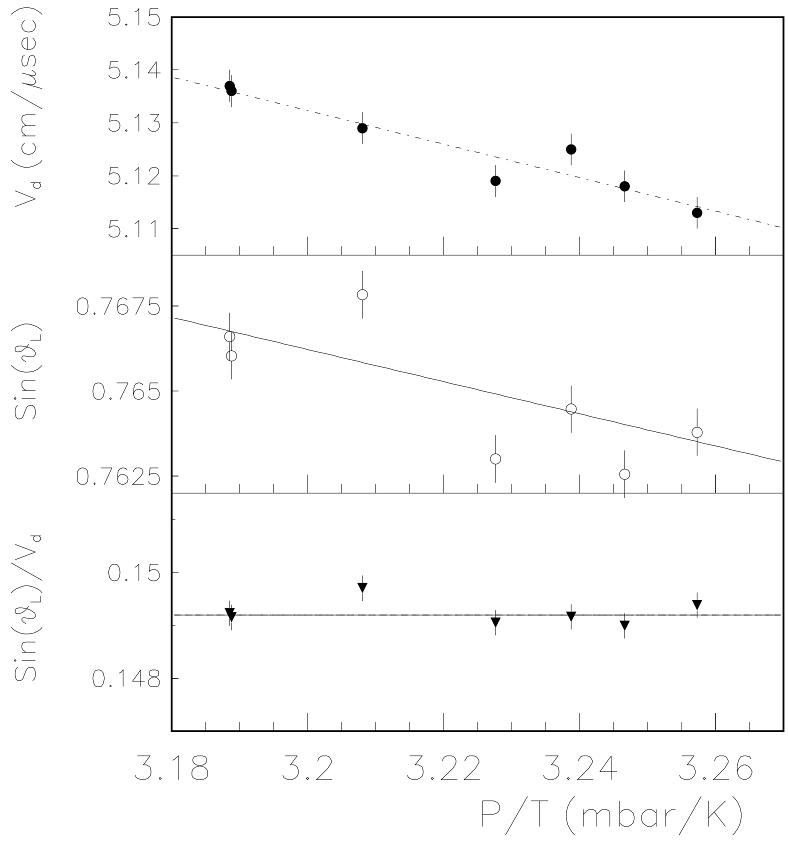

Figure 4.16: *Drift velocity and Lorentz angle as a function of P/T*

Chapter 5

Track Selection and Performance of the RICH

RICH data of good quality are obtained after on-line calibration and off-line tuning of the detector alignment and the background reduction. These data play a role in many physics analyses. In our analysis we have to distinguish kaons from pions. The fraction of kaon production in τ decay is only a few percent. Therefore, the misidentification probability must be reduced as much as possible; it is the main systematical error of the final result. So it is essential to understand all features of the RICH well, including subtle ones that may not be of consequence in other analyses. In this chapter we describe the performance of the RICH and the improvements we made on the Cherenkov angular resolution after DST processing.

The kaons from τ decay have a momentum higher then 3.5 GeV$/c$. The Cherenkov angle from the liquid radiator is saturated in this momentum region (figure in 3.2.1). Therefore, our analysis only uses data from the gas radiator. The data of the FRICH are not included in our analysis for reasons of tracking quality, statistics and neutral particle measurement in the forward region.

About 1,200,000 Z^0 events with the Barrel RICH detector operational have been recorded in the running period from 1992 to 1994. Muons from the decay $Z^0 \rightarrow \mu^+\mu^-$ were used to study the behaviour of the RICH and to check the stability of the detector during data taking. This provided a clean and well known sample. These muons have a momentum of 45GeV$/c$, where the Cherenkov angle is saturated (61 $mrad$ in the gas radiator) and the number of Cherenkov photons is maximal.

5.1 Track Selection

The Cherenkov angle is calculated for a given particle from the positions where photons hit the detection plane and from the location and direction of the particle track in the radiator. Therefore, good particle tracking is needed.

In the barrel region, tracking through the RICH was done by interpolation between the track segment measured in the TPC, located before the RICH and the measurement in the Outer Detector just behind the RICH. Therefore about 16%

tracks were rejected due to the absence of TPC or OD in tracking. It was also required that the uncertainty on the momentum was less than 20%.

The quality of the RICH data was checked by the number of photons observed per Cherenkov ring. Figure 5.1 shows the number of photo-electrons per ring as a function of the polar angle θ_p of the particle track. To stay well within the Barrel RICH acceptance, only tracks with $48^0 < \theta_p < 87^0$ and $93^0 < \theta_p < 132^0$ were accepted.

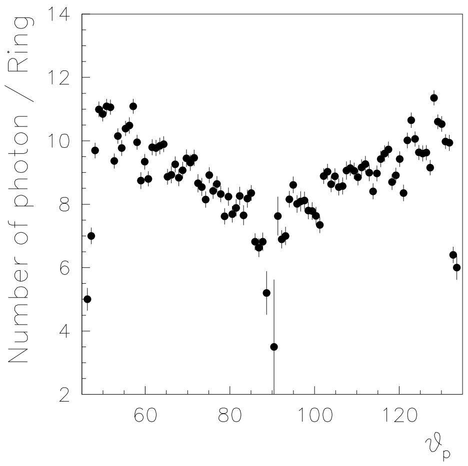

Figure 5.1: *Photon production as a function of the particle polar angle*

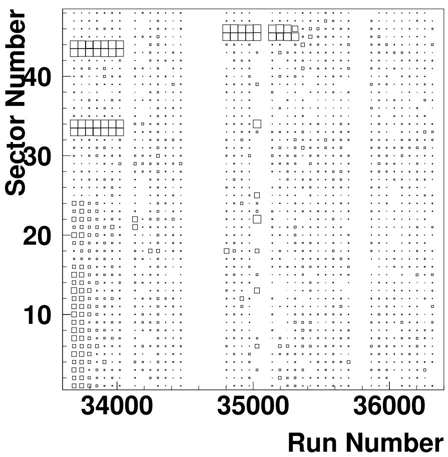

Figure 5.2: *Fraction of low photon production as a function of sector and run number. The size of a square is proportional to the numerical value, with maximum equal to 1 and minimum equal to 0.*

Poor sectors and running periods were identified by looking at the number of photo-electrons produced. We define the low photon production fraction as:

$$f = \frac{N_{low}}{N_{total}} \tag{5.1}$$

where N_{low} is the amount of tracks with less than 2 photons observed and N_{total} is the total amount of tracks. This fraction is shown for different sectors and runs in Figure 5.2, where the size of the box is proportional to the fraction. Sector numbers 1-24 correspond to side A of the detector, sector numbers 25-48 are on side C. Some dead sectors are clearly visible by a big box in the figure. All these cases were grouped in periods and rejected.

DST information was also used to identify data taking periods where problems with electronics, high voltage, radiator transparency, drift gas composition, etc.

caused insufficient quality of the data. These data were discarded for further analysis.

Even at maximum Cherenkov angle, each particle produces only 8 photons on average. Therefore, a few background digitisations among the true Cherenkov photons will spoil the determination of the average Cherenkov angle. Therefore tracks with a high background and bad Cherenkov angle determination were excluded. These criteria were applied after the fitting of the Cherenkov angle.

5.2 Ring Identification

For each detected photon, the expected error σ_γ on the Cherenkov angle is calculated (see 3.2.1). The resolution function is given by:

$$F = \frac{\theta_\gamma - \theta_{c,exp}}{\sigma_\gamma} \tag{5.2}$$

where θ_γ is the measured Cherenkov angle and $\theta_{c,exp}$ and σ_γ are the expected Cherenkov angle and its expected error respectively.

For a σ_γ that is estimated correctly, the resolution function of individual photons is a gaussian with a standard deviation $\sigma_F = 1$ plus a slowly rising background. However, when using the DST values of σ_γ the fit gives an average σ_F of 1.23 for 1992 data and of 1.35 for 1993 data. There is a clear dependence of the value of σ_F on the mirror group number. To obtain correct values of σ_γ, we parameterised σ_γ as a function of track and photon information from the DST.

We discuss the expected error of individual photons in the section 5.2.1 and the improvement of Cherenkov angle measurement in the section 5.2.2. However these two tasks are strongly correlated. An iterative procedure was used. In each step, photons within $2.5\sigma_\gamma$ window around expected value were used to parameterise new expected errors and to correct the systematic errors in the Cherenkov angle measurement.

5.2.1 Angular Resolution

According to equation 3.4 the following components were calculated:

Chromatic dispersion: σ_{chrom}

For a gaseous radiator the relation between the spreads in θ_γ and in the index of refraction n is:

$$\frac{\Delta\theta_\gamma}{\theta_\gamma} = \frac{\Delta n}{2(n-1)} \tag{5.3}$$

The window of sensitivity of the RICH detector is about $5.6-7.5$ eV. With $\Delta n/(n-1) = 2.9\%$ from table 3.1, one obtains $\Delta\theta_\gamma/\theta_\gamma = 2.8\%$. Assuming a uniform detection yield over the sensitivity region, we find:

$$\sigma_{chrom} = 2.8\%\theta_\gamma/\sqrt{12} < 0.5mrad$$

Track bending: σ_{bend}
Substitution of $l = L\sin\theta_p$ (L=40 cm is the distance between the mirror plane and the photon detector) in equation 3.5 gives:

$$\sigma_{bend} = \alpha_B \frac{L\sin\phi}{p} \tag{5.4}$$

The constant of proportionality α_B was determined from real data of single prong τ decays, where the momentum region of the single charged particle is 4-45 GeV. The result is $\alpha_B = 1.1$ mradGeV/cm.

Position resolution: $\sigma_{position}$
The position resolution of the RICH photon detector includes the intrinsic spatial resolution of the MWPC's, drift diffusion, any distortions of drift trajectories, etc. Its main variation is with drift distance. Photoelectrons from a certain mirror group i (i=1,..6) have drift distances z in a range of $\pm$ 12 cm around a central value $z_{mirror,i}$. For a detailed study of position resolution per mirror group, photons were binned in the relative drift coordinate $z' = z - z_{mirror,i}$. Per bin, the r.m.s. spread was determined of the measured Cherenkov angles for individual photons from dimuon events. Figure 5.3 shows the result as a function of z' for the six mirror groups. At the muon momentum of 45 GeV/c, the error contribution from track bending is small compared to the position resolution error, and the chromatic aberration error is always smaller than 0.5 $mrad$. Therefore, the data shown in fig. 5.3 are a good estimate of the position resolution of the photon detector. A second order polynomial function $\sigma_{position} = a_1(1 + a_2 z' + a_3 z'^2)$ describes the dependence on the reduced drift coordinate z' well.

External source of error: σ_{ext}
The study of dimuon events revealed that the r.m.s. spread on the Cherenkov angle depends on the azimuthal position ϕ of a photon along the ring image, as shown in figure 5.4. This is caused by a misalignment between the TPC and the BRICH, leading to a shift of the reconstructed particle path in the BRICH to the true trajectory. This in turn leads to an apparent change of the Cherenkov angle, that for photons at $|\cos\phi|$=1 fully affects the drift coordinate. At the longest drift distances (mirror group 1) the effect is maximal. The dimuon events were subjected to a global fit $\sigma_\mu^2 = \sigma_{position}^2 + (a_4\cos\phi)^2$ for each mirror group. Table 5.1 lists the parameters found by the fit.

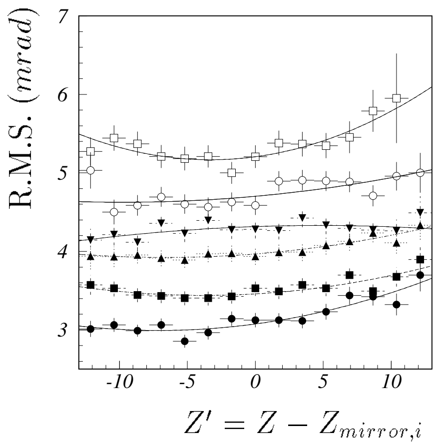

Figure 5.3: *Spread of Cherenkov angle as a function of relative drift distance for mirror groups 1 (top) to 6 (bottom).*

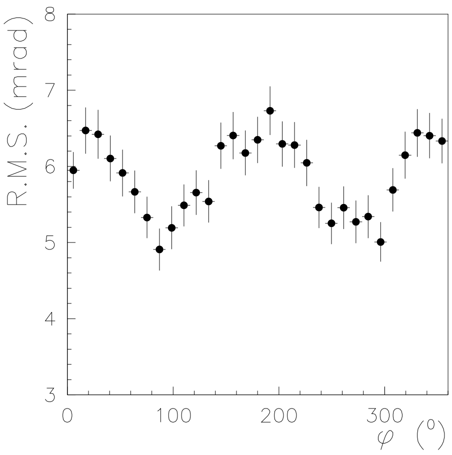

Figure 5.4: *Spread of Cherenkov angle as a function of photon azimuth (mirror group 1)*

Number of mirror	1	2	3	4	5	6
a_1 (mrad)	4.06	4.08	4.07	3.55	3.45	3.05
$a_2(10^{-3}cm^{-1})$	6.61	3.46	4.08	1.43	4.91	2.46
$a_3(10^{-4}cm^{-2})$	3.65	1.76	5.91	6.89	-0.87	8.34
a_4 (mard)	3.51	3.22	2.46	2.44	0.64	0.43

Table 5.1: *Parameters for individual photon error estimation (see text)*

Finally, σ_γ is the quadratic sum of σ_{bend}, $\sigma_{position}$ and σ_{extra}. The error from chromatic dispersion, σ_{chrom}, is much smaller than the others and is neglected.

5.2.2 Improvement of the Cherenkov angle measurement

The Cherenkov angle measured by an optimal detector should depend on the velocity of the particle only. Therefore the way to optimise the RICH detector is to identify the dependences of the measured Cherenkov angle on any variables provided by DST information and correct them.

5.2.2.1 Mirror alignment

The Cherenkov light produced in the gas radiator is reflected by focusing mirrors onto the photon detector. To be able to reconstruct the Cherenkov angle from the measured position of a photon in the detection plane, the positions of the mirrors and the orientation of their optical axes have to be known precisely. Extraction of this information from the data is called software alignment. All mirrors have been aligned individually before DST processing using muons from $Z^0 \rightarrow \mu^+\mu^-$ events by minimising the spread of the observed Cherenkov angles.

The alignment before DST processing proved to be correct for most of the mirrors, but a few of them were not aligned correctly, because of the underestimation of the single-photon error σ_γ. A misaligned mirror shifts the Cherenkov ring from its expected position. A clear dependence of the Cherenkov angle on the azimuthal position ϕ of the photon is then seen (figure 5.5) for some mirrors. Such mirrors have to be aligned again.

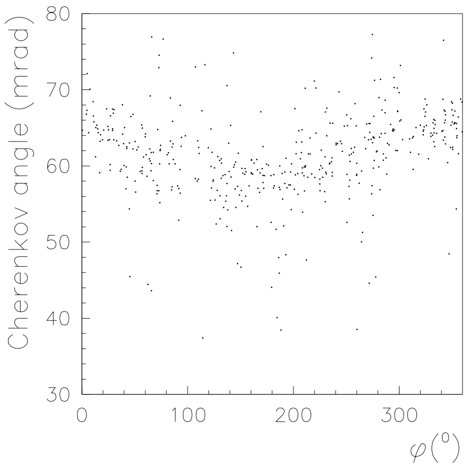

Figure 5.5: *Cherenkov angle of individual photons as a function of photon azimuth ϕ before proper mirror alignment*

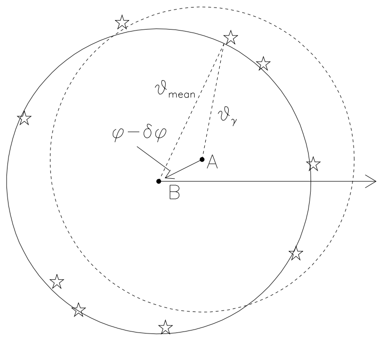

Figure 5.6: *Illustration of the RICH mirror alignment*

Mirror alignment is not possible *ab initio* with the information on DST, but because the remaining displacement is small and the alignment is equivalent to a shift of the ring (see figure 5.6), we can apply the following fit:

$$\theta_\gamma = \theta_{mean} - \delta\theta_\gamma cos(\phi - \delta\phi) \tag{5.5}$$

where θ_γ is the measured Cherenkov angle, ϕ is the azimuth of the photons from the DST, and θ_{mean} is the mean Cherenkov angle. The quantity $\delta\theta_\gamma$ represents the amplitude of the shift from point A to point B and $\delta\phi$ its direction .

To reduce effects of background, we only use photons within a few σ_γ around the expected value of the Cherenkov angle, θ_{exp}. But if the mirror is not well aligned this window can not be small, otherwise we loose good photons. To get a good fit the following three iteration steps were made:

- Use the photons within 3.5 σ_γ around θ_{exp}.
- With the result of the first step, use the photons within 3 σ_γ around θ_{exp}.

- With the result of the second step, use the photons within 2.5 σ_γ around θ_{exp}.

With this alignment the angular resolution could be improved by 10%.

5.2.2.2 Top and bottom difference

In the 1993 data, we observed different saturated Cherenkov angle in sectors at the top and at the bottom of the BRICH detector (figure 5.7). At the top of the detector (90^0 in fig. 5.7) the mean value has a minimum and at the bottom (270^0) it has a maximum.

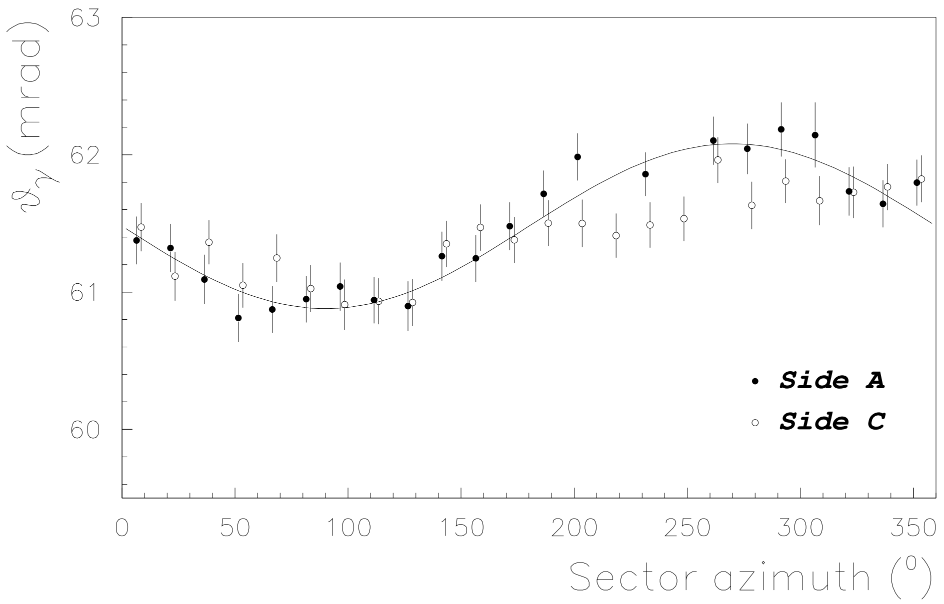

Figure 5.7: *Cherenkov angle as a function of sector azimuth from 1993 data*

Considering that $\cos\theta_\gamma=\frac{1}{\beta n}$, where n is the refractive index of the gas radiator, the most natural assumption is that the difference is caused by a gradient in refractive index. As an example we look at side A of the detector, where the difference in Cherenkov angle between top and bottom sectors is 2% . In the approximation β=1 and n-1$\ll$1, we get :

$$\frac{\Delta\theta_\gamma}{\theta_\gamma} = \frac{\Delta n}{2(n-1)}$$

A priori, there are a few possible causes for a height dependence of n:

- a temperature gradient;
- a pressure gradient;
- height dependence of the gas radiator composition.

According to the Lorentz-Lorenz law, (n-1) $\propto \frac{P}{T}$. The observed difference between Cherenkov angles at the top and bottom of the detector would require a difference of 15^0C in temperature or of 46 mbar in pressure; both are far outside the actual ranges of variation.

The difference between top and bottom is probably caused by a different concentration of admixed C_6F_{14}, that is the leakage from the liquid radiator, in the C_5F_{12} gas radiator. Since C_6F_{14} is heavier than C_5F_{12}, it tends to stay at the bottom of the detector. If f_T and f_B are the fraction, of C_6F_{14} in C_5F_{12} at the top and bottom respectively, the refractive index is:

$$\begin{aligned} Top : n &= f_T n_6 + (1 - f_T) n_5 \\ bottom : n &= f_B n_6 + (1 - f_B) n_5 \end{aligned}$$

The difference is:

$$\Delta n = (n_6 - n_5)(f_T - f_B)$$

Substituting the observed difference $\Delta\theta_\gamma$ in Δn=2(n-1)$\frac{\Delta\theta_\gamma}{\theta_\gamma}$ and using $n_6 - n_5$=0.0002,

one obtains the estimate

$$f_T - f_B \backsim 35\%$$

This looks like a possible explanation for the top and bottom difference. In our analysis a correction was applied for each sector.

5.2.2.3 Drift velocity

The measured position of the Cherenkov photons in x- and y- direction are simply given by the anode wire and cathode strip addresses which are stable. The z coordinate is calculated from the drift time of the photo-electron using two important constants, the drift velocity and the zero offset of drift timing. Small variations of these constants happened from time to time or sector to sector during data taking for different reasons. The use of wrong drift parameters shift the Cherenkov ring along the drift direction. This is parametrised similar to equation 5.5, but with the restriction that the shift $\delta\theta_\gamma$ only in the drift direction.

$$\theta_\gamma = \theta_{exp} + \delta\theta_z cos(\phi) \tag{5.6}$$

where θ_{exp}=61.5 mrad.

After the alignment described in the previous section, $\delta\theta_z$ is zero on average. But certain periods and sectors were identified with non-zero $\delta\theta_z$. In the figure 5.8, the fitted shift $\delta\theta_z$ is shown for tracks in sector 25 and 26 as a function of run number. A jump in the zero offset or the drift time measurement can be seen. Figure 5.9 shows the dependence of $\delta\theta_z$ on the particle polar angle. On the side A ($\theta_p < 90°$) the photo-electrons with the longest drift distance (near 90°) have a significant shift. This corresponds to a drift velocity mismeasurement in order of 0.15%.. To correct these effects, the shift $\delta\theta_z$ was parameterised as a function of run number and drift distance.

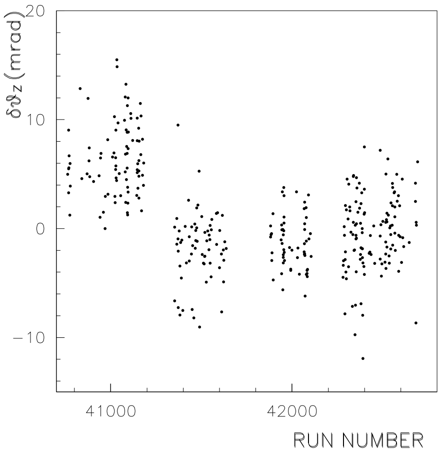

Figure 5.8: *Ring shift along the drift direction in sector 25 and 26 as a function of run number.*

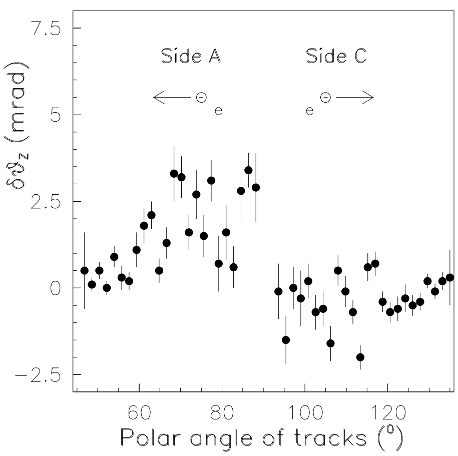

Figure 5.9: $\delta\theta_z$ *as a function of the particle polar angle for the data taken in August 1994.*

5.2.2.4 Miscellaneous

after the alignment and calibration described above, two remaining effects of the order of 4 or 5 *mrad* were identified and corrected:

Based on large statistics, it was found that within a mirror the rings shift systematically towards the center of the mirror and the images of the rings were slightly distorted (became ellipses). This can be explained by a shorter focal length of the mirrors than expected. Since mirrors of each group have the same shape, the corrections were made for each group separately. The variations from mirror to mirror are not observable within the statistics.

It was also found that the shift of the rings was a function of the depth in the photon detector where the Cherenkov photons were converted. There is no particular reason to explain this. Best guesses are bugs in the processing programme or remaining effects of other systematic deviations.

5.2.3 Photon Clusters

Background photons almost always occur in clusters. Therefore we reject background photons by looking for clusters of photons. At DST level the space coordinates of photons are not given. Instead, we use the Cherenkov angle θ_γ of each photon and its azimuthal angle ϕ along the ring image to get the relative position on the detection plane. In our analysis, a cluster of photons is built from the definition that two photons belong to the same cluster if their distance is less than 2.6 mm. This value is mainly determined by the rounding precision (0.1 rad) of the angle ϕ in the DST format.

It was found that most of the clusters have only one or two photons as expected.

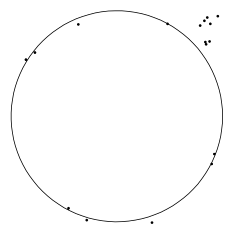

Figure 5.10: *Example of a Cherenkov ring with a big photon cluster.*

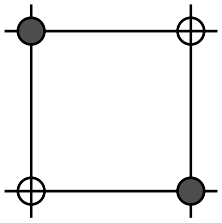

Figure 5.11: *Illustration of 4-photon cluster with 2 ghost photons.*

From the comparison of the data with a simple Monte Carlo simulation we conclude that small clusters contain mainly good Cherenkov photons. At the other extreme, there are some big clusters with five or more photons (figure 5.10). These may originate from oscillations or from cross-talk in the electronics. They can also belong to the ionisation signal of an other particle. (The optics of the BRICH is such that the ionisation of a track of a particle can not overlap with its *own* Cherenkov ring.) Big clusters are considered as background and removed if they contain more than 5 photons.

It was also found that the number of clusters containing four photons is higher than expected. Some of these clusters contain ghost photons, that are hit combinations of anode wires and cathode strips in an MWPC. When two real photo-electrons arrive in the MWPC plane at the same time, they produce two hits at the points indicated by the filled circles in figure 5.11, two so-called "ghost" photons (open circles) were also reconstructed. According to the properties of the ghost photon (*i.e.* Groups containing four photons with equal drift time and a hits pattern as indicated in the figure were identified. To distinguish the ghost pair from the pair of real photons, the difference in the apparent Cherenkov angle of the two photons is calculated for both pairs. The pair with the large difference is rejected as ghost photons.

5.2.4 Reconstruction of the Cherenkov Ring

The resolution function of individual photons from dimuon events and from high momentum hadrons from single-prong τ decay, with values of σ_γ calculated according to the procedure described above, is shown in figure 5.12(a) and 5.12(b). The plots show a low level of background. Signal to background ratios within 2.5 σ_γ around the expected Cherenkov angle were found to 9 and 6 for tracks from $\mu^+\mu^-$ events and single-prong τ decay.

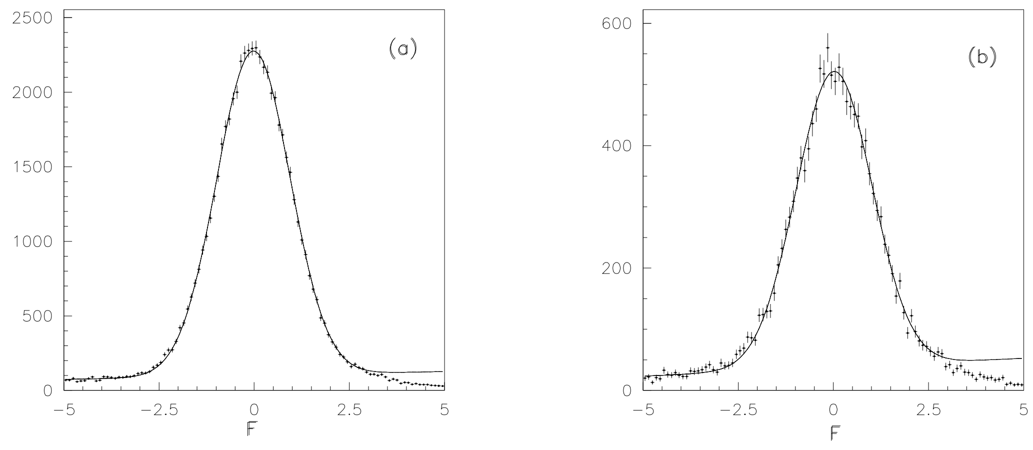

Figure 5.12: *The distribution of the resolution function F for individual photons from: (a)dimuons; (b)single-prong τ decay;*

To determine the Cherenkov angle θ_c of a particle from the individual photon measurements the photons are grouped. For each possible group the weighted average Cherenkov angle θ_c is calculated, with a weight per photon equal to $1/\sigma_\gamma^2$. A group is called a consistant set, if no photon of the set lies outside the window of $\pm 2.5\sigma_\gamma$ around θ_c and no photon not belonging to the set lies inside that same window. For track with more than one consistent set, the one with maximal number of photons and best χ^2 was chosen.

The expected error σ_c in θ_c was calculated from the errors σ_γ of the individual photons. It gives an average of 1.6 mrad for dimuon events. Variations around the average come from statistical fluctuations in the number of photo-electrons produced and from the kinematics of the particle track. Figure 5.13(a) and (b) show the resolution function of the Cherenkov angle for dimuon events before and after the correction (section 5.2.2). The improvement is observed. The tails on the resolution function F of tracks are significantly low. After the correction, the distribution can be well described by a Gaussian distribution with a standard deviation of one.

5.3 Veto Identification

In the veto identification region it is important to ensure for each particle that the RICH was fully active. Therefore, apart from the criteria mentioned in section 5.1, we ask that at least two ionisations along the particle track in the drift tube were recorded. This requirement implies a 10% reduction in acceptance, because it leads to rejection of particles passing through gaps between the drift tube sectors (which in itself does not affect the emission and detection of Cherenkov light). Below 4 GeV/c both the Cherenkov angle and the number of radiated photons decrease for

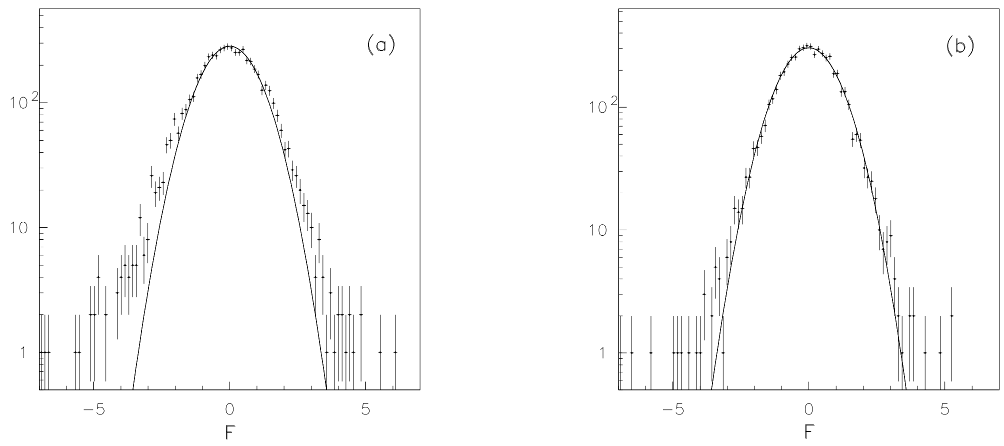

Figure 5.13: *The distribution of the resolution function F for muons from the decay $Z^0 \to \mu^+\mu^-$ (a)before the correction and (b)after the correction. The curves are Gaussian distribution with a standard deviation of one.*

pions. This increases the chance of pions being *misidentified* as kaons. With the large error of the individual photons and because of the track bending in the magnetic field, there is a high chance of background signals in the fiducial region around the expected Cherenkov angle. This decreases the *efficiency* of veto identification of kaons. Therefore, between 4 GeV/c and the the kaon threshold 3.5GeV/c no effort was made to identify kaons.

For reliable veto identification the yield of photo-electrons has to be well understood. The expected amount of photo-electrons per particle follows a Poisson distribution around a mean value depending on the mass and the momentum of the particle, the length of radiator it passes through, photon detection efficiency. The expected photon production was calculated for each particle track(see 3.2.1). Figure 5.1 shows the observed photo-electrons as a function of the polar angle of the particle for dimuon events. The variation with polar angle is caused by the different radiator lengths seen by the particle. In figure 5.14(a) the distribution of the expected amount of photons for 45 GeV/c muons is shown, together with the experimental distribution of the number of detected photo-electrons in a window of ± 2.5 σ_γ around the expected Cherenkov angle. One observes good agreement between the expected and observed distributions, including the bin with zero photo-electrons that is used for veto identification. The average is 8.4 photo-electrons per ring. In figure 5.14(b) the same distributions are shown for high momentum (20-35 GeV/c) particles from single prong τ decay. Here the average value is 8.2, nearly the same as the saturation value. Figure 5.14(c) shows the distribution for particles from single prong τ decay with a momentum in the veto identification region. The population of the bin with zero photo-electrons comes from kaons. The distributions of observed photon-electrons were identical for the three samples within the statistical errors.

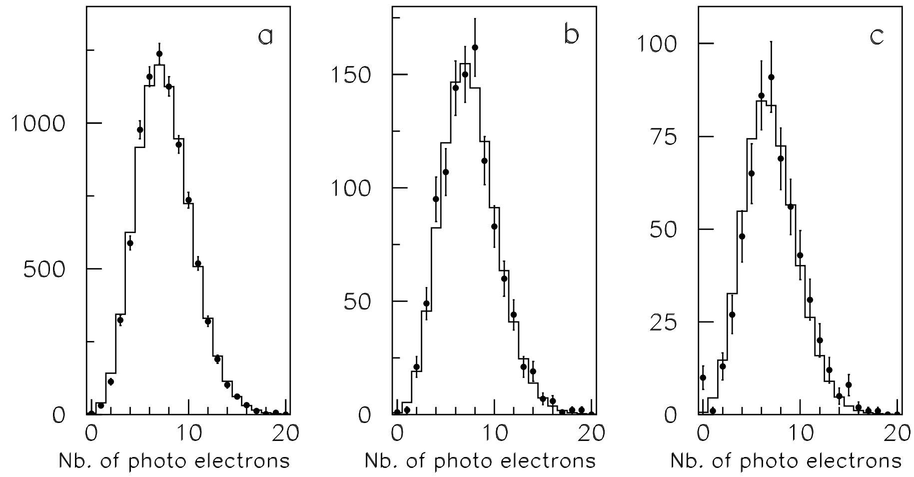

Figure 5.14: *Distributions of the number of photo-electrons for 45 GeV/c muons (a) and for high-momentum (b) and low-momentum (c) particles from single prong τ decays.*

Their good agreement with the expected distributions demonstrates that the issue of photon yield is well understood, as required for the method of veto identification.

5.4 Performance in single-prong τ decay

The techniques of charged kaon identification with the RICH detector have been used in single-prong τ decay successfully for the data taken in 1992[39]. The update of the analysis is ongoing[40].

In the veto mode a particle is identified as a kaon if no associated photo-electrons are observed. Therefore, the misidentification rate is the probability of observing no photo-electrons for a muon or a pion. From dimuon events and high momentum particles, the misidentification rates were found to be compatible with Poisson statistics for the expected amount of photo-electrons. It was estimated for each track, taking into account the slight decrease of the number of photo-electrons from muons or pions at momenta in the veto identification region. The result was $(0.15\pm0.04)\%$ from exclusive single prong τ decays. The inefficiency for kaon identification in the veto mode is given by the probability for finding a noise hit in the window around $\theta_{(\pi,\mu)}$, the expected Cherenkov angle for a π or a μ. The probability was calculated from the final sample of kaon candidates in veto identification for single prong τ decays. All photo-electrons were counted in the large area corresponding to 120 mrad around the track where the pattern recognition programme searches for photon candidates. After scaling of the area it was concluded that the efficiency for kaon veto identification is 99%.

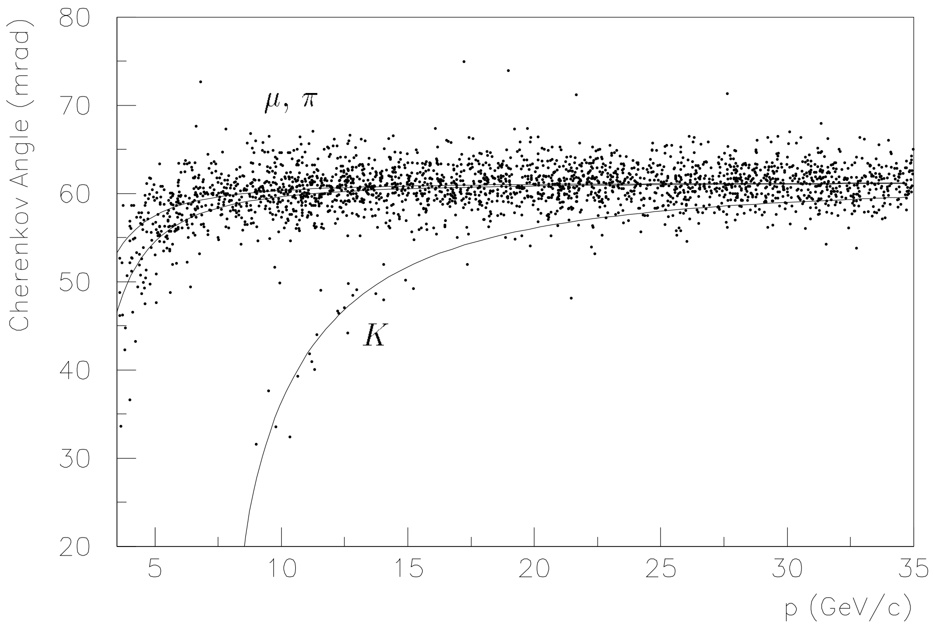

Figure 5.15: *Cherenkov angle as a function of momentum for single prong τ decays*

After applying our corrections described in the previous sections, the Cherenkov angles could be measured well. Figure 5.15 shows the Cherenkov angle as a function of momentum for single-prong τ decays. The solid lines show the expected angles for K and (μ, π). A kaon population is clearly visible.

In the ring identification mode, the particle is identified as a kaon if the measured Cherenkov angle is compatible with the kaon hypothesis within $\pm 2.5\sigma_c$ and incompatible with the (π,μ) hypothesis, i.e. more than n_{sep} σ_c below $\theta_{(\pi,\mu)}$. Obviously, the value of n_{sep} must be chosen with care: with increasing n_{sep} the background from misidentification decreases, but at the same time the identification efficiency becomes lower. The study of single prong τ decays showed that the $K/(\pi,\mu)$ ratio was stable within 2% for $n_{sep} \geq 4$, but starts to decrease significantly at $n_{sep} = 3$. The value 3.5 was chosen. This gives an efficiency for ring identification of 92%

The same techniques were extended to three-prong τ decays where we face more problems. This is discussed in the next chapter.

Chapter 6

Data Analysis

During recent years there has been a growing interest in measuring the decays of τ leptons into strange mesons. In this chapter, the measurement of the branching ratios of the decays $\tau^- \to K^-K^+\pi^-\nu_\tau(neutrals)$ and $\tau^- \to K^-\pi^+\pi^-\nu_\tau(neutrals)$ is described using a data sample of Z^0 events recorded with the DELPHI detector at LEP in 1992, 1993 and 1994. The charged kaons were tagged by the gas Barrel RICH, which provides good kaon and pion separation on a track-by-track basis. The resonances in the decays have been studied.

6.1 Event selection

At LEP energy, a $\tau^+\tau^-$ event consists of two collimated low multiplicity jets in opposite direction. The two hemispheres are separated by the plane perpendicular to the event thrust axis. The thrust axis is calculated using all "good" charged particles, those with momenta larger than 0.6GeV/c and a distance of closest approach to the interaction region less than 0.2 cm* in the plane perpendicular to the beam and less than 4.5 cm along the beam direction. This requirement rejects most of the charged tracks from interactions and photon conversions in the detector. The remaining tracks from photon conversion eliminated by mean of delicated track fitting programme which is tuned to tag such tracks. The sample of 3-prong τ decay was selected by requiring 3 charged particles on one side and up to 3 charged particles on the other side. This requirement already resulted in a clean sample of 3-prong τ decays, since hadronic Z° decays, $Z^\circ \to \mu^+\mu^-$, $Z^\circ \to e^+e^-$, single-prong τ decays and cosmic ray have completely different topologies.

In our measurement, the event selection was adapted to the kinematical conditions for kaon identification in the RICH. As explained later, a kaon in the fiducial volume of the RICH with momentum between 6GeV/c and 20GeV/c can be identified unambiguously. Therefore an event, with at least one particle of the 3-prong side meeting this condition, is accepted. The number of two photon events was reduced by the minimal momentum requirement of 6GeV/c.

To reduce the background further, the following criteria were also applied :

* Without associated hits in the vertex detector, the limit is 4.0 cm.

1. The particles in the opposite hemisphere have at least a total momentum of 1GeV/c.
2. The isolation angle, which is defined as the smallest angle between two particles in opposite hemisphere, was required to be bigger than 165°.
3. Event was rejected when neutral particles of more than 5GeV/c were observed outside a cone of 20° around the thrust axis.
4. Event was rejected when additional bad track was found in the 3-prong side.
5. Event was rejected if two tracks in 3-prong side have no associated hits in the Vertex Detector and the Inner Detector.

A first step no effort was made to identify the neutrals in the 3-prong τ decays, this will be discussed afterwards. The cuts mentioned above, together with the requirement of good RICH quality (see section 5.1), produce a sample of 6171 events of 3-prong τ decays. From a detailed simulation of the detector and by using JETSET[37] and the KORALZ[38] event generator, the background inside the acceptance was found to be 1.3% from single-prong τ decay and less than 0.2% from hadronic Z° decays.

6.2 Kaon Identification in 3-prong τ decays

To identify the kaons in 3-prong decays we use the same two techniques (veto and ring identification) as for single-prong τ decays[39]. However, at Z^0 energy tracks from such τ decays are close together. The images of the Cherenkov rings may overlap, so that some of the photons may be attributed to more than one track. To get a similar good K/π separation as for the single-prongs the photons were selected carefully. Simultaneous fits were made to find the ambiguous photons. The effects of the background were taken into account in the angular resolution and noisy tracks were rejected. First of all the photo-electrons were selected. In the ring identification the following steps were made:

- Fit the ring independently for each track, and resolve part of ambiguous photons.
- Fit the rings simultaneously for two tracks if there are ambiguous photons.
- The error of the measured Cherenkov angle for each track is corrected.

In the veto identification only the selected good photons were taken into account.

To gain in efficiency veto and ring identification both were applied for particles with a momentum between 8.5 and 10.5 GeV/c.

6.2.1 Photon Selection

Figure 6.1 shows the resolution function of individual photons from 3-prong τ decays. Compared with dimuon events (fig 5.12) the signal to background ratio is much smaller ($S/B = 4$). Apart from bad photons from clusters (Section 5.2.3), 3-prong τ decays have ambiguous photons caused by overlap between liquid and gas rings, or by the overlap between gas rings. Figure 6.2 shows an example of two overlapping gas rings with several ambiguous photons.

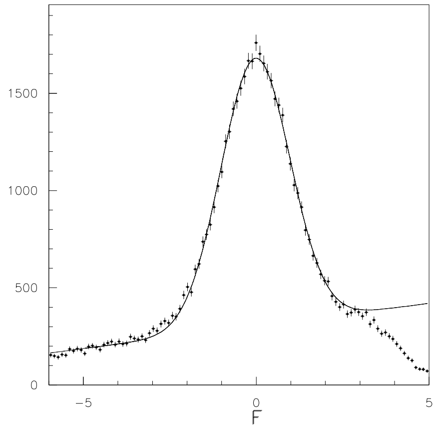

Figure 6.1: *The resolution function F of individual photons in 3-prong τ decays ($p \geq 6.0 GeV/c$)*

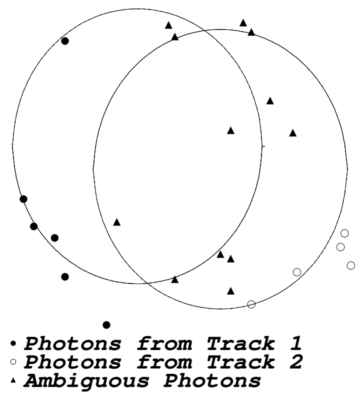

Figure 6.2: *The images of two overlapping rings*

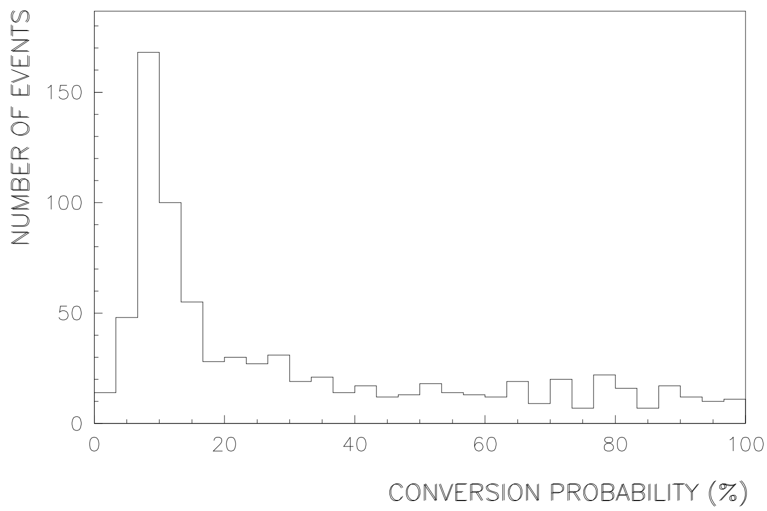

Figure 6.3: *Conversion probability (P) of the ambiguous photons between liquid and gas*

To identify the ambiguous photons between liquid and gas rings, a normalised conversion probability was used, calculated from the photon conversion length in the detector ($\lambda = 2.5\ cm$ in the BRICH) and the path length of the photon in the photon detector. Figure 6.3 shows the distribution of the conversion probability of ambiguous photons. A peak around 10% is clearly seen. It is caused by photons from the liquid radiator that entered the photon detector from the other side. Most of them were absorbed immediately after entering the detector. Therefore a cut at 18% was applied to reject ambiguous photons between liquid and gas rings.

Photons attributable to 3 rings were discarded, because they are mostly background and it takes too much CPU time in a multi-fit. The ambiguous photons attributable to two gas rings are separated in two classes. One class consists of photons that don't belong to the K or π band of the other track†. These photons are kept as good photons, the signal to background ratio is ($S/B = 5$), and the ambiguities are solved. The other class consists of photons that do belong to the K or π band of the other track. In this class the signal to background ratio is naturally low, because about half of the photons belong to the other track. They are the real ambiguous photons. The multi-fit will assign them to one of the two tracks.

photons		S/B	Comments	Group
un-ambiguous photons		7.0	good photons	1
gas - liquid ambiguity	$P < 18\%$	0.5	killed as liquid photons	2
	$P > 18\%$	6.5	good photons	3
gas - gas ambiguity	solved	5.0	see text	4
	unsolved	1.2	see text	5
attributed to 3 tracks		0.5	discarded	6

Table 6.1: *photon classification*

In summary, the photons are classified in a few groups (Table 6.1). Figure 6.4(a) shows the resolution function of the good photons (from groups 1, 3 and 4). They have a similar signal to background ratio as the single-prong τ decays ($S/B = 6.0$). The discarded photons (group 2 and 6) are shown in figure 6.4(b). There the S/B is only 0.5. Figure 6.4(c) shows that of photons from group 5 ($S/B = 1.2$).

6.2.2 Ring Identification

The independent fit is performed with the good photons (groups 1,3 and 4 in Table 6.1), in the same way as we did for $\mu^+\mu^-$ tracks and single-prong τ decays. After the independent fit, each ambiguous photon is checked to see if it could belong to both fitted rings. When the real ambiguous photons are identified, the multi-fit is applied. To save CPU time in the multi-fit, the ambiguous photons with a Cherenkov angle 4σ above the π hypothesis were assigned to the other track.

In the multi-fit the ambiguous photons are assigned to any of the tracks and the informations of the fits are combined. The assignment is chosen such that it gives

† In 3-prong tau decays only K and π were taken into account

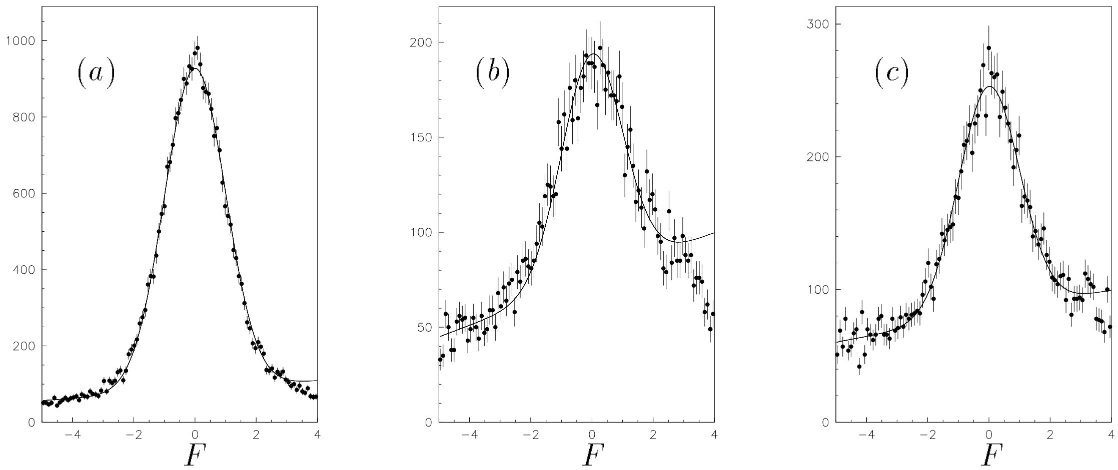

Figure 6.4: *Resolution functions F of the photons in 3-prong τ decays: (a) good photons, (b) discarded photons, (c) ambiguous photons.*

the maximum of good photons and the best χ^2. To decrease the effect of ambiguous photons, the weight of these photons was decreased by a factor of $\sqrt{2}$. No multi-fit was applied for tracks with more than 10 ambiguous photons. The results of the independent fits were kept instead.

For each track an uncertainty σ_c is calculated from the error of each individual photon (section 5.2.1). In 3-prong τ decay, the resolution function for each track is defined as: $F = \frac{\theta_c - \theta_\pi}{\sigma_c}$. It was found that the distribution of F was a gaussian distribution with a standard deviation of 1.5 and a tail . This is caused by background photons or by a bad reconstruction of the rings. Therefore the effect of background photons on the resolution per track has to be studied and the uncertainty σ_c has to be corrected. The noisy and not well reconstructed tracks were rejected to remove the tail on the resolution function.

The high momentum ($p > 6\mathrm{GeV}/c$) particles in 3-prong τ decays were used to study this. The r.m.s, per bin, is used to define the width of the resolution function. The difficulty is the impossibility to estimate the background precisely on a track-by-track basis. Therefore we define the r.m.s. as the width of the resolution function and increase the error σ_c according to changes of the width as a function of the following factors:

Quality of the fit

Sometimes when we determine the Cherenkov angle of a particle, more than one consistent set of photons was found (section 5.2.1). In this case the detected photons are not well clustered because of the presence of many background photons or because the tracking is not good. The resolution function of these tracks has a standard deviation 1.4 times the usual one. We take as the best fit the set of photons with the maximum amount of photons and the best χ^2. The uncertainty

σ_c becomes:

$$\sigma_c \Longrightarrow \sqrt{\sigma_c^2 + (\theta_c - \theta_c')^2} \tag{6.1}$$

where θ_c and θ_c' are obtained from the best fit and from the second best fit.

Multi-fit

The multi-fit is needed when the tracks are close together and therefore the signal is more noisy. We had to multiply σ_c by a factor of $f_{mf} = 1.1$ to get the resolution function comparable to the others.

Background photons

We define the observed amount of background photons N_{bg} as the number of good photons in the band between $\pm 2.5\sigma_\gamma$ and $\pm 5.0\sigma_\gamma$ around θ_c. When more background photons were observed the resolution function became wider (figure 6.5).

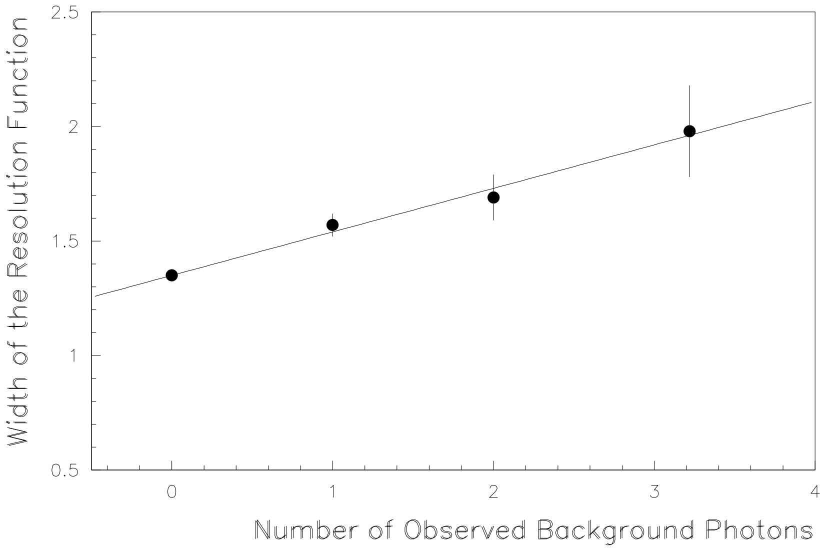

Figure 6.5: *The width of the resolution function as a function of the observed background photons.*

Therefore the following factor is needed:

$$f_{bg} = 1.0 + 0.26 N_{bg} \tag{6.2}$$

Non-uniformity along the ring

Normally the Cherenkov photons should have an uniform distribution along the ring (from 0 to 2π). Sometimes the distribution along the ring is not a uniform distribution because of a cluster of background photons or because of a tracking problem. We define the non-uniformity of a ring as:

$$\vec{r}_c = \sum_{i=1}^{N_{fit}} \vec{r}_i / \sqrt{N_{fit}} \tag{6.3}$$

where N_{fit} is the number of photons that are used in determining the average Cherenkov angle θ_c of the ring, and $\vec{r}_i$ is a unit vector in the direction of photon i. The division by $\sqrt{N_{fit}}$ is made here to get $|\vec{r}_c|$ independent of N_{fit}. A ring is more homogeneously populated for smaller $|\vec{r}_c|$. The dependence of the width of the resolution function on $|\vec{r}_c|$ is clearly seen in figure 6.6.

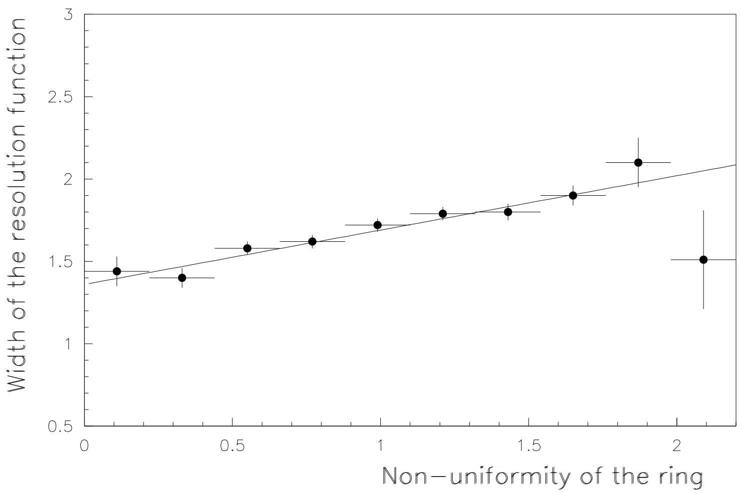

Figure 6.6: *The width of the resolution function as a function of the non-uniformity of the ring* $|\vec{r}_c|$.

The following factor is applied to increase σ_c:

$$f_{uf} = 1.0 + 0.17|\vec{r}_c| \tag{6.4}$$

Removed background photons

Before the fitting of θ_c, most of the background has been removed (*i.e.* by background reduction before DST, killed ghost photons and ambiguous photons). We define the fraction of good photons as:

$$r_{fit} = \frac{N_{fit}}{N_{total}} \tag{6.5}$$

where N_{fit} is the same as before and N_{total} is the total number of digitisations in a 90 mrad cone around the track. Again we see that the width of the resolution function increases as r_{fit} decreases (figure 6.7). Therefore we make another correction:

$$f_{kill} = 1.0 + 2.1(1.0 - r_{fit}) \tag{6.6}$$

In summary, the uncertainty σ_θ of a track is calculated from single photon uncertainties and the factors defined above:

$$\sigma_\theta = f_{uf} f_{kill} f_{bg} f_{mf} \sqrt{\sigma_c^2 + (\theta_c - \theta_c')^2} \tag{6.7}$$

In this way the resolution function has a gaussian distribution with a standard deviation of one. Figure 6.8 shows the distribution of the resolution function (the kaons are on the negative side of the distribution).

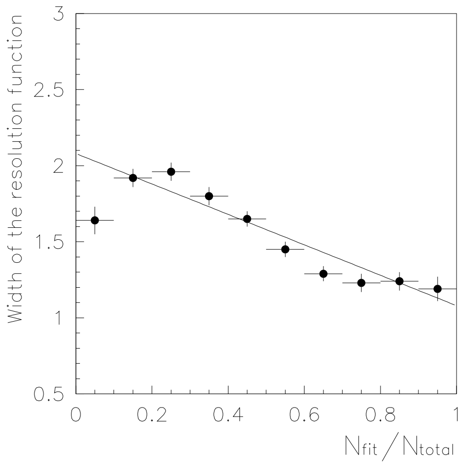

Figure 6.7: *The width as a function of r_{fit}*

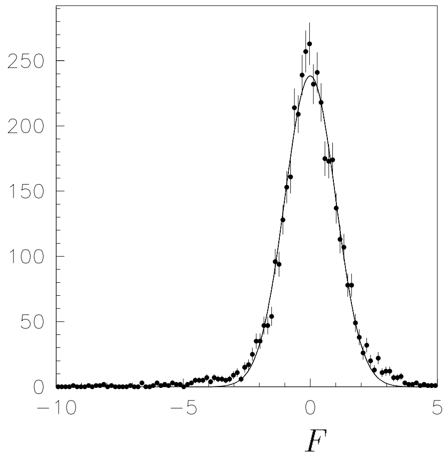

Figure 6.8: *The distribution of the resolution function F of the hadrons from 3-prong τ decay.*

Some of the tracks are so noisy or have a tracking so wrong that the problem can not be solved by increasing the errors. This is the main contribution to misidentification. Figure 6.9 shows the fraction of K candidates as a function of the variables r_{fit} and $|\vec{r}_c|$ (defined above).

Therefore the following 3 cuts were required to reject noisy tracks:

(1) r_{fit} is bigger than 0.15.
(2) $|\vec{r}_c|$ is smaller than 2.2.
(3) $2N_{bg}$ is smaller than N_{fit}.

Figure 6.10 shows the measured Cherenkov angle of a track as a function of the particle momentum for multi-prong τ decays. It also shows the expected angle for K and π. A K population around the expected line is clearly seen.

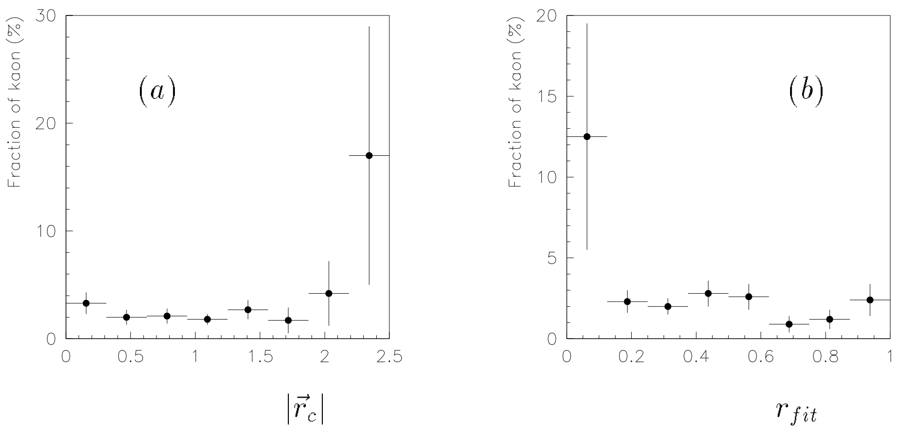

Figure 6.9: *Fraction of kaon candidate as a function of: (a) $|\vec{r}_c|$ and (b) r_{fit}.*

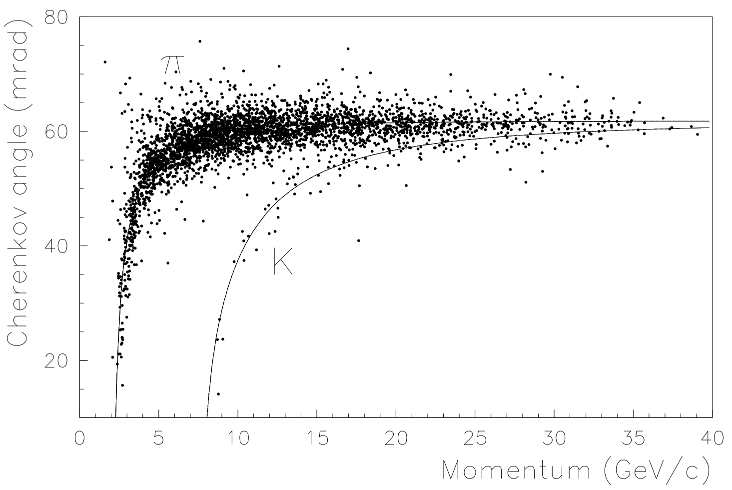

Figure 6.10: *Cherenkov angle as a function of momentum for 3-prong τ decays (Only the tracks with σ_θ smaller than 3.0mrad are shown).*

6.2.3 Veto Identification

As for the single-prong τ decays, the yield of photo-electrons in veto identification has to be well understood. The intrinsically expected number of photo-electrons $N_{intri,exp}$ was calculated for each track. In the 3-prong τ decay, the K/π separation is more difficult than in single prong because the tracks are close to each other. They produce more electronic noise and have a larger dead region. The consequence of this is that we will have more background and fewer true photons. The overlapping rings have similar effects. In our analysis, only the good photons (*i.e.* the groups 1, 3 and 4 in the Table 6.1) are used to reduce the background as much as possible. Therefore the number of observed photons N_{obs} is defined as the number of good photons within $\pm 2.5\sigma_\gamma$ window around the π hypothesis θ_π.

To get a good K/π separation we re-estimated the photon production for a π hypothesis. Just as for the angular resolution this is difficult to estimate on a track-by-track basis. Therefore we parametrise with several variables‡. To study the photon production, high momentum particles from 3-prong τ decays are used and all tracks are treated as pions, the effect of 2% kaons is neglected.

In the whole photon selection procedure, two steps were made to reduce the background. One is the background reduction in the data processing before the DST. It is a loose cut for the general RICH information, which rejects the background from dE/dx signals of the tracks and from electronic noise. The other step is a tight selection for the 3-prong τ analysis (Section 6.2.1), that rejects mainly the ambiguous photons. We define the number of photons rejected by these two steps, N_{k1} and N_{k2}, as follows:

$$\begin{aligned} N_{k1} &= N_{total} - N_{2.5\sigma} && (6.8) \\ N_{k2} &= N_{2.5\sigma} - N_{obs} && (6.9) \end{aligned}$$

where N_{total} is the total amount of digitisations within the 90 $mrad$ corn around the track, $N_{2.5\sigma}$ is the number of photons left in the $\pm 2.5\sigma_\gamma$ band around π hypothesis after the first selection. We expect that when more photons were killed as background, fewer good photons were left. Figures 6.11 (a) and (b) show the changes in $N_{obs}/N_{intri,exp}$ as a function of N_{k1} and N_{k2}.

These observations lead to a better approximation of the expected photon production:

$$N_{exp} = N_{intri,exp}\exp(-N_{k1}/100 - N_{k2}/20) \qquad (6.10)$$

On the average the photon production per ring is 5.5 in 3-prong τ decays, much smaller than that in dimuons and single-prong τ decays (7.9 photons per ring). To have good K/π separation in the veto region, only those particles were selected, which in the π hypothesis had an expected photon production N_{exp} higher than 6.2. This makes the probability for observing no photons from a π less than 0.2%.

In the veto identification some further cuts were applied to reduce the misidentification rate. The tracks on mirrors 1 and 2 (polar angle between 70° and 110°) were rejected because of relatively low photon production and high background. Each track must have hits on the Outer Detector to make sure that the tracking is correct up to the Outer Detector. At least two dE/dx photons must be visible along the track in the drift tube of the RICH for two reasons: (1). To be sure the BRICH is fully active on a track-by-track basis. (2). To reject tracks at the gaps between

‡ Here it is important to select the variables that don't or hardly depend on the photon production.

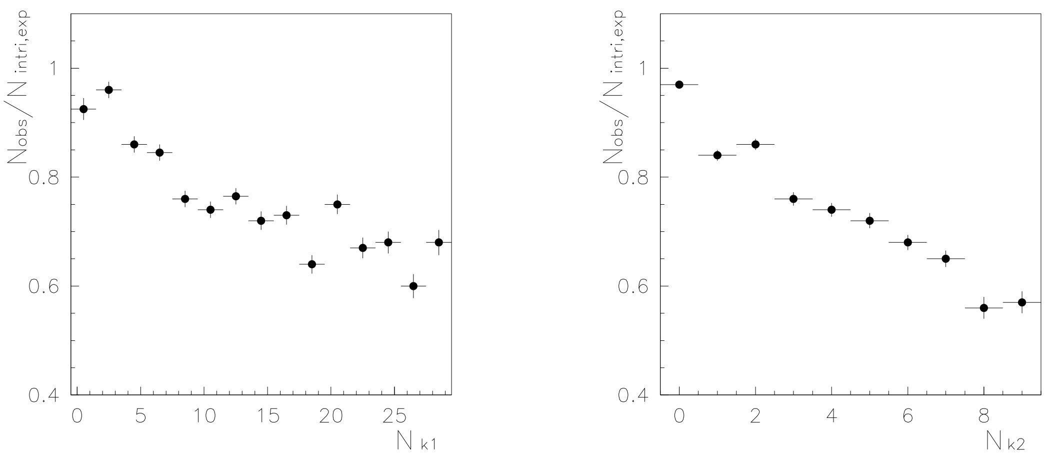

Figure 6.11: *$N_{obs}/N_{intri,exp}$ as a function of the number of rejected photons N_{k1} and N_{k2} (see text).*

adjacent drift tubes because of their poorly understood photon production. Kinematically the minimum momentum of a K in 3-prong could be 4.0 GeV/c, but near 4.0GeV/c the K production is small while the π production reaches a maximum. Therefore, the veto identification was only applied for particles with a momentum between 6.0 and 10.5 GeV/c. Tracks with high $N_{k1}(\geq 13)$ were rejected because of high background. The veto identification was not applied to the 1992 data.

After all these cuts only 22% of the particles in the veto region survive. Figure 6.12 shows the distribution of observed photo-electrons and of the expected amount

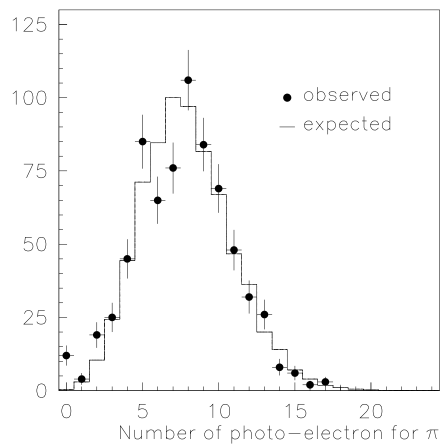

Figure 6.12: *photo-electron production*

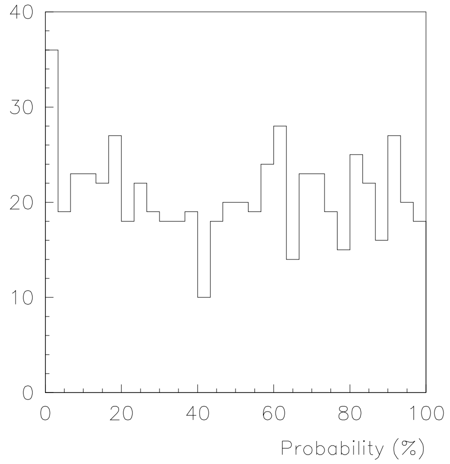

Figure 6.13: *Pion probability*

of photons with a Poisson distribution. The kaon production is seen at bin zero. Figure 6.13 shows the pion probability distribution of these tracks. A particle is taken as a kaon if the probability is less than 0.2%. The misidentification rate was found to be compatible with poisson statistic for the expected number of photo-electrons.

Another inefficiency in K identification is given by the probability of finding a noise hit in the window around θ_π, which may cause a kaon to be misidentified as a pion. This probability is calculated from the final sample of kaon candidates from the veto identification. All good photons were counted in the large area corresponding to 100 mrad around the tracks. Of 14 kaon candidates in 1994 data, only 1 background photon was identified by the pattern recognition programme. From the scaling of the area it was concluded that the efficiency is larger than 96%

6.3 Branching Ratios in 3-prong τ decays to Kaons

In this section the analysis is made to determine the branching ratios of $\tau^- \to K^-K^+\pi^-\nu_\tau(neutrals)$ and $\tau^- \to K^-\pi^+\pi^-\nu_\tau(neutrals)$. Kaons were identified in the veto identification region from 6.0 to 10.5GeV/c, and in the ring identification region from 8.5 to 20.0GeV/c.

After the tracking quality requirements (section 5.1) and the RICH quality cuts (section 6.2), the kaon identification efficiency is low, and the chance to identify all three particles in a 3-prong τ decays is very small. Instead the branching ratios are determined by the following procedure:

- Tag the events with at least one charged kaon in the final state.
- Identify the event as $K^-K^+\pi^-$ or $K^-\pi^+\pi^-$.
- Determine the branching ratios.

The branching ratios of $\tau^- \to K^-K^+\pi^-\nu_\tau(neutrals)$ and $\tau^- \to K^-\pi^+\pi^-\nu_\tau(neutrals)$ were derived from the number of tagged events of these two decays compared with the total number of 3-prong τ decay events, for which the world average branching ratio was used:[41]

$$Br(\tau^- \to h^-h^+h^-\nu_\tau(neutrals)) = (14.49 \pm 0.23)\%$$

With this method most of the systematic errors cancel.

6.3.1 Kaon Production in 3-prong τ decays

After the effects of background were taken into account, the resolution function of the Cherenkov angle θ_c is well described by a gaussian distribution with a standard deviation of one(Figure 6.8). As in single-prong τ decays, a particle is identified as a kaon if the measured Cherenkov angle θ_c is within $\pm 2.5\sigma_c$ around θ_K (expected angle in the kaon hypothesis) and is incompatible with θ_π (expected angle in the pion hypothesis), *i.e.* more than $n_{sep}\sigma_\theta$ below θ_π. In our analysis $n_{sep} = 3.0$ has been chosen. Similarly, a particle is identified as a pion if θ_c is compatible with θ_π and incompatible with θ_K. The misidentification rate was derived from particles with a momentum 6.0 to 8.5GeV/c, where pions produce almost the maximal amount of photons and the kaons produce no photons. It was calculated by integrating the tails on the negative side of the resolution function of these tracks (incompatible with π hypothesis), and scaling the area to the K hypothesis (compatible with K hypothesis). It was concluded that the rate of a pion being misidentified as a kaon is $0.14 \pm 0.06\%$.

The efficiency for K identification is shown in figure 6.14. It is calculated from the number of tracks that passed all criteria mentioned above and that were identified unambiguously as a kaon or a pion, divided by the total amount of tracks for the selected events. The inefficiency includes the following factors:

1. A 25% inefficiency because of additional tracking quality cuts for the particle identification.
2. 7% of the tracks have been killed in the ring identification because of bad ring measurement or noise.
3. About 20% of the kaons do not produce enough photons to reconstruct the ring near the threshold. This has been calculated from the probability of having less than 2 photons for a kaon hypothesis.
4. 55% tracks were rejected in the veto identification region because of low photon production and high background.
5. When the momentum increases, the K and π Cherenkov angles differ less; therefore the efficiency drops.

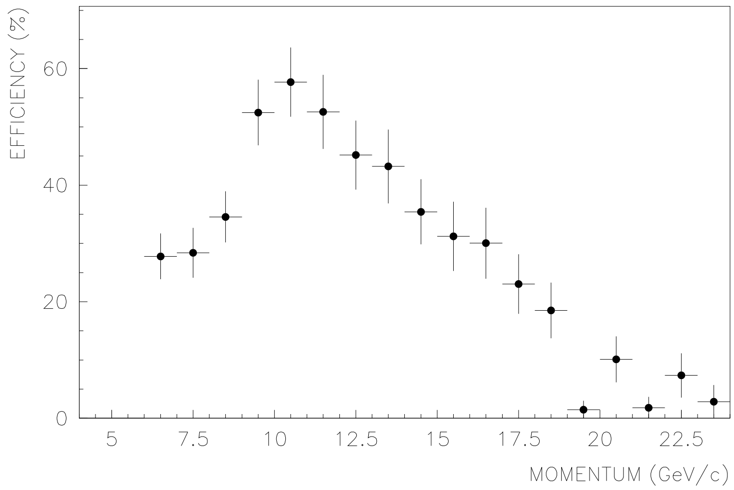

Figure 6.14: *Efficiency for kaon identification as a function of the momentum of the particle*

With our method, the efficiency for tagging $K\pi\pi$ events is equal to the efficiency for kaon identification, and the efficiency of tagging $KK\pi$ events is equal to the sum of the 2 kaon identification efficiencies minus the product of the 2 efficiencies. In 3-prong τ decays, two of the particles have the same charge. Their trajectories are bent in the same direction in the magnetic field. These two tracks have more chance to be close and parallel to each other. Therefore, their tracking qualities are a bit worse than that of the third one, and their images of Cherenkov rings have more chance to overlap because in the gas radiator of the RICH detector the position of the ring is only sensitive to the direction of the track. We found that the efficiency for these like-charged particles is about 30% lower than that for the oppositely charged particles.

Considering the momentum dependent efficiency of the particle identification, the momentum spectra of K and π (figure 6.15) in 3 prong τ decays were simulated with the KORALZ programme. Assuming the efficiencies for π and K identification are the same, an average efficiency was calculated by the multiplication of the efficiency and the K momentum distributions. The efficiencies of identifying the h^- and h^+ of τ^- decay were found to be 19.4% and 24.2% respectively for 1994 data. Therefore the average efficiency to tag $\tau \to KK\pi\nu_\tau(neutrals)$ is $38.9 \pm 1.0\%$ and the efficiency to tag $\tau \to K\pi\pi\nu_\tau(neutrals)$ is $19.4 \pm 0.5\%$. The uncertainty in the efficiency(2.5%) is dominated by the uncertainty of the K spectrum from different τ decay models.

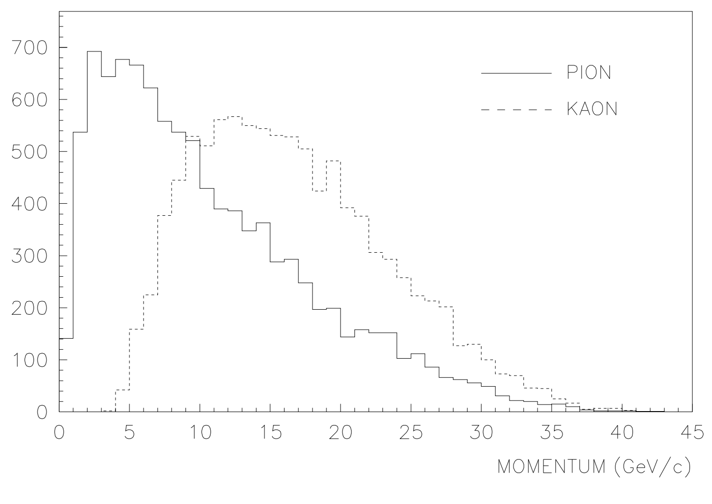

Figure 6.15: *Particle momentum spectrum in 3-prong τ decays.*

The result on kaon production has been listed in Table 6.2. In total, 92 candidates of τ decays to kaon(s) were tagged. The number of background events, caused by a pion misidentified as a kaon, could be calculated from the misidentified kaons. In our sample 105 identified kaons are corresponding to 92 events, therefore 7.1 ± 2.6

misidentified kaons are equivalent to 6.2 ± 2.5 background events.

	3-prong	identified tracks		tagged as Kaon		Events	Background of
	events	in veto	in ring	in veto	in ring	with kaons	misidentified kaon
92	1112	—	631	–	14	12	1.0 ± 0.4
93	931	117	613	4	14	15	1.2 ± 0.5
94	4128	798	2932	14	59	65	4.9 ± 2.0
total	6171	915	4176	18	87	92	7.1 ± 2.9

Table 6.2: *Number of identified kaons and events in 3-prong τ decay.*

6.3.2 Inclusive Branching ratios

It is important to identify the pion(s) or the second kaon for the separation of the decays $\tau \to KK\pi\nu_\tau(neutrals)$ and $\tau \to K\pi\pi\nu_\tau(neutrals)$. Within the sample of identified 3-prong events where one particle has already been identified as a kaon, the kaon to pion ratio is not small. Thus, the misidentification rate needs not to be as low as in the first step of the analysis, where rare kaons had to be identified in the full sample of 3-prong events. In this second step of analysis a few methods are combined:

1. Identification of a second kaon (without the tracking and the RICH quality cuts).
2. Pion identification. A particle is identified as a pion if:
   - 2a. the momentum of the particle is lower than $3.5\mathrm{GeV}/c$.
   - 2b. In the veto region, at least two good photons were observed in the window of the pion hypothesis.
   - 2c. Unambiguously identified pions are present in the ring identification region.
3. Charge combination. Since the two kaons in $KK\pi$ and the two pions in $K\pi\pi$ must have opposite charge, the event is identified as a $KK\pi$ ($K\pi\pi$) if the particle with opposite charge of τ is identified as a kaon (pion).

With these methods, 40 $KK\pi$ candidates and 51 $K\pi\pi$ candidates were identified. One event was identified as background because of a wrong charge combination. The details of these events are listed in Table 6.3.

Since the error from other backgrounds is small compared to the statistical error, they are estimated from Monte Carlo. The background from single-prong τ decays was calculated from the single-prong K fraction of 2%[39]. With 1.3% single-prong τ decays in the sample, we expected 0.2 ± 0.1 background events in the 1994 data sample. The background in hadronic Z° decays was calculated from the K fraction of 25%[42]. With 0.2% hadronic Z° decays in the sample, we expected 0.4 ± 0.2

Number of event	comments	event type
29	the second kaon has been identified	$KK\pi$
38	two opposite charged pions have been identified	$K\pi\pi$
11	identified kaon has the opposite charge of the τ	$KK\pi$
13	identified pion has the opposite charge of the τ	$K\pi\pi$
1	2 identified pions with the same charge	Background

Table 6.3: *Event identification*

background events in the 1994 data sample. The 4.9 misidentified kaons corresponding to 4.4 background event. In total, 5.0 background events were expected in the 1994 sample of 3-prong τ decays to kaon(s). One event was identified as a background event because of a wrong charge combination. The remaining background events were split statistically over the samples of $\tau \to KK\pi\nu_\tau(neutrals)$ and $\tau \to K\pi\pi\nu_\tau(neutrals)$. The uncertainty was taken into account in the systematical error.

During the three years, the quality of the RICH data has been improving. The consequence is that the efficiencies are slightly changing. The efficiency to tag $\tau \to KK\pi\nu_\tau(neutrals)$ is 33.9% and 22.7% for 1993 and 1992 respectively. The efficiency to tag $\tau \to K\pi\pi\nu_\tau(neutrals)$ is 15.7% and 10.5% for 1993 and 1992 respectively. Therefore the branching ratios were calculated separately for these three years, and the final branching ratios are the weighted averages. Table 6.4 lists the steps of determining the branching ratios for 1994, and table 6.5 gives the average results and the statistic errors.

final states	$KK\pi$	$K\pi\pi$	3-prong
Candidates	23	41	4182
Misidentification	4.4 ± 2.0		
Single-prong	0.2 ± 0.1		54
Hadronic Z° decays	0.4 ± 0.2		neglected
Identified background	1.0		
Total background	4.0 ± 2.0		54
signal	21.6	38.4	4128
efficiency (%)	38.9	19.4	
Branching ratio/Br(3-prong) (%)	1.34 ± 0.28	4.79 ± 0.74	
Branching ratio (%)	0.19 ± 0.04	0.69 ± 0.11	

Table 6.4: *Determining the branching ratios and the statistic errors for 1994 data*

Several sources of systematic uncertainties were investigated (Table 6.6). They are much smaller than the statistical error. The largest uncertainty in the measurement arises from the background estimation. Because of statistics and because of

Decay mode	$\tau^- \to K^-K^+\pi^-\nu_\tau(neutrals)$	$\tau \to K^-\pi^+\pi^-\nu_\tau(neutrals)$
1992	0.42 ± 0.15	0.45 ± 0.23
1993	0.39 ± 0.13	0.56 ± 0.23
1994	0.19 ± 0.04	0.69 ± 0.11
average	0.22 ± 0.04	0.63 ± 0.09

Table 6.5: *Inclusive branching ratios (%) of τ decay to charged kaon(s)*

the transfer of the background in the K sample to the event sample in the analysis, an uncertainty was expected of about 2.9 events leading to 3.1% in the branching ratios. In identifying the decay mode loose cuts were used that have a misidentification rate of 2%. Therefore, about 2% correlation was expected between the two branching ratios. In the τ selection, the rejection of background events is controlled at the level of 2%, which gives a 2% uncertainty in the final results. Two further uncertainties coming from the kaon identification efficiency and the branching ratio of $Br(\tau^- \to h^-h^+h^-\nu_\tau(neutrals)$ amount to 2.5% and 1.6% respectively. In total 5.1% systematic uncertainty is expected.

Misidentifition Background	3.1
Correclation between the decays	2.0
τ selection	2.0
K identification efficiency	2.5
$Br(\tau^- \to h^-h^+h^-\nu_\tau(neutrals))$	1.6
Total	5.1

Table 6.6: *Determination of the systematic error (in %).*

The branching ratios determined from our sample are:

$$Br(\tau^- \to K^-K^+\pi^-\nu_\tau(neutrals)) = (0.22 \pm 0.04 \pm 0.01)\%$$

and

$$Br(\tau^- \to K^-\pi^+\pi^-\nu_\tau(neutrals)) = (0.63 \pm 0.09 \pm 0.03)\%$$

In Figure 6.16, our result for the branching fractions of $\tau^- \to K^-K^+\pi^-\nu_\tau(neutrals)$ and $\tau^- \to K^-\pi^+\pi^-\nu_\tau(neutrals)$ are compared with DELCO[44],BES[45], TPC/2γ[47] and the world average of 1994[41]§

For the $\tau^- \to K^-K^+\pi^-\nu_\tau(neutrals)$, our result is in excellent agreement with other experiments, while our results for the decay $\tau^- \to K^-\pi^+\pi^-\nu_\tau(neutrals)$ is

§ In the reference, the result of ARGUS $Br(\tau^- \to K^-\pi^+\pi^-\nu_\tau) = (0.33 \pm 0.11 \pm 0.13)\%$[48] is also on the list. But it has been measured via $\tau \to K^*K\nu_\tau$, therefore we remove the result from the list and make the new average. The result of ARGUS 95 is listed in the next subsection.

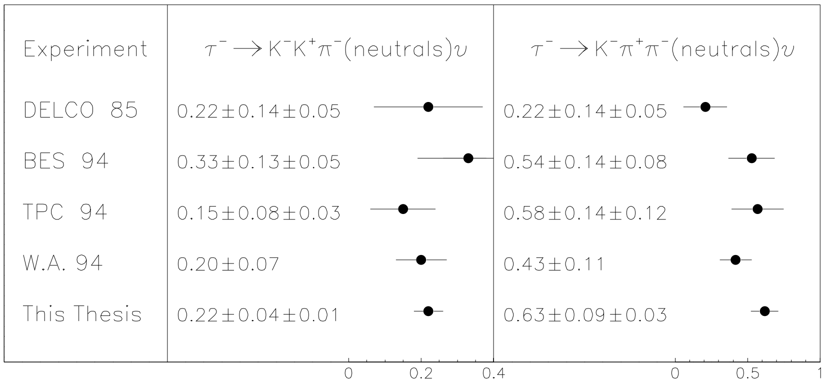

Figure 6.16: *The branching fractions (%)of $\tau^- \to K^-K^+\pi^-\nu_\tau(neutrals)$ and $\tau^- \to K^-\pi^+\pi^-\nu_\tau(neutrals)$ compared with other experiments.*

about one standard deviation higher than the world average of 1994. However the measurements of TPC and BES also show a significantly higher rates than DELCO ten years ago.

6.3.3 Exclusive Branching ratios

We checked our $K\pi\pi$ and $KK\pi$ samples for the presence of neutral particles by looking for π° candidates from the electromagnetic calorimeter (HPC) energy clusters within a 20° corn around the event thrust axis.

The π° decays into two photons. If the energy of the π° is sufficiently low (typically below 5 GeV) the two photons develop two separate showers in the calorimeter. For an energetic π° decay the two photons are too close to each other to be separated as two independent showers in the HPC. Therefore the π°'s could be defined as follows:

1. Electromagnetic shower, with an energy above $1.5GeV$, is not associated with any charged tracks
2. The invariant mass of two photons is between 0.05 GeV/c^2 and 0.225 GeV/c^2.
3. The sum of the electromagnetic shower energy in the HPC is above 20 GeV.

Using the MC data of $\tau^- \to a_1^- \nu_\tau \to 3\pi^\pm\nu_\tau$ and $\tau \to \rho'\nu_\tau \to 3\pi^\pm\pi^\circ\nu_\tau$, the efficiency of this selection is found to be 76.1% and misidentification rate is 13.0%.

With this selection a significant π° signal was observed in both decays. Figure 6.17 shows the π° invariant mass reconstructed from two photons in the 91

3-prong candidate events of τ decay to kaon(s). We found that 10 of the 40 $\tau \to KK\pi\nu_\tau(neutrals)$ candidates and 14 of 51 $\tau \to K\pi\pi\nu_\tau(neutrals)$ candidates have a π°.

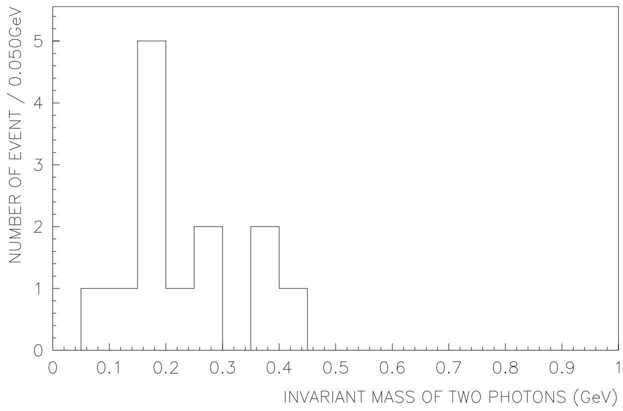

Figure 6.17: *invariant mass of* π°

We have the branching fractions:

$$\begin{aligned} Br(\tau^- \to K^-K^+\pi^-\nu_\tau) &= (0.18 \pm 0.04)\% \\ Br(\tau^- \to K^-\pi^+\pi^-\nu_\tau) &= (0.49 \pm 0.08)\% \\ Br(\tau^- \to K^-K^+\pi^- \geq 1\pi^\circ\nu_\tau) &= (0.04 \pm 0.02)\% \\ Br(\tau^- \to K^-\pi^+\pi^- \geq 1\pi^\circ\nu_\tau) &= (0.14 \pm 0.04)\% \end{aligned}$$

Only the statistical errors are given here, the systematic errors are neglected.

6.4 Further study of the decays $\tau \to KK\pi\nu_\tau(\pi^\circ)$ and $\tau \to K\pi\pi\nu_\tau(\pi^\circ)$

The hadronic decays of the τ lepton appear to be dominated by coupling of the W boson to ud or us resonant states. The experimental results of τ decays to π and K are in excellent agreement with the theoretical prediction. The $(\pi\pi)^-$ and $(K\pi)^-$ decays are dominated by the ρ^- and K^{*-} vector channels, while the $(\pi\pi\pi)^-$ decay occurs predominantly through $(\rho\pi)^-$ in s wave, consistent with a_1^- axial-vector dominance. However, the resonance structure of $(KK\pi)^-$ and $(K\pi\pi)^-$ decays is still an open question, because of their small branching ratios and the difficulties in identifying and reconstructing the strange mesons. In this section we describe the study of the resonant structures with our 40 candidates of $(KK\pi)$ and 51 candidates of $(K\pi\pi)$.

6.4.1 Resonances in the decays

In the standard picture, the τ decay to $KK\pi$ occurs through the $\rho'(1700)$ resonance. The dominant decay of the $\rho'(1700)$ goes to four pions, while a small fraction decays into K^*K, with the K^* decaying into $K\pi$:

$$\begin{array}{lll} \tau \longrightarrow \rho'(1700)\nu_\tau & & \\ \qquad \hookrightarrow K^*(892)K & & \\ \qquad\qquad \hookrightarrow K\pi & & \end{array}$$

For the 40 candidates of $\tau \to KK\pi\nu_\tau(\pi^\circ)$, the invariant mass of the opposite charge kaon-pion pairs was reconstructed. Figure 6.18 shows the distribution of the invariant mass. A clear peak of the K^* resonance is seen, and few events are not within $\pm 100MeV$ around the K^* mass, compatible with the expected background. Therefore, the conclusion is that the decay $\tau \to KK\pi(\pi^\circ)\nu_\tau$ is dominated by the $\tau \to K^*K(\pi^\circ)\nu_\tau$ decay.

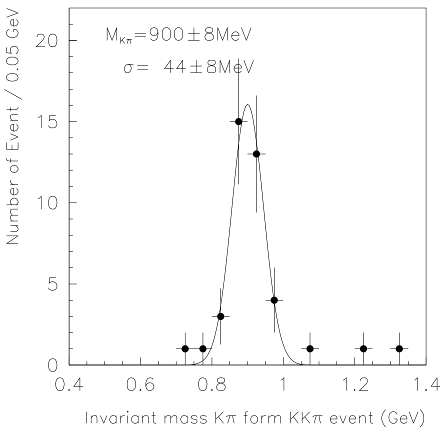

Figure 6.18: *K^* signal in $\tau \to K^-K^+\pi^-(\pi^\circ)\nu_\tau$.*

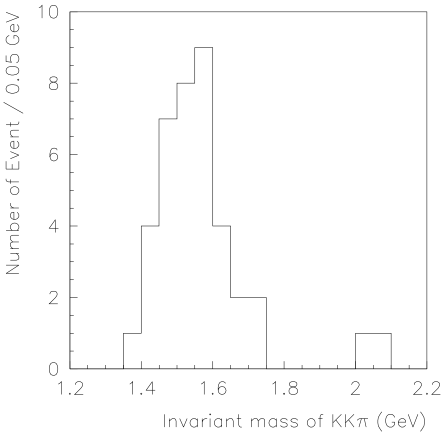

Figure 6.19: *Invariant mass of $KK\pi$.*

The invariant mass spectrum of $KK\pi$ (figure 6.19) shows a great potential for the ν_τ mass measurement. Events with mass above $2.0GeV$ might come from background events. To extract a limit on the ν_τ mass more efforts are needed, especially for the tracking and further background reduction.

According to theory, there are two relevant particles that have the correct quantum numbers for a three particle resonance with one kaon, *i.e.* the $K_1(1270)$ and $K_1(1400)$, which are mixtures of the $\bar{s}d$ states in $^3P_1$ and $^1P_1$ quark nonets. The dominant decay chains of $K_1(1270)$ and $K_1(1400)$ are:

$$\begin{array}{lcl} \tau \longrightarrow K_1(1270)\nu_\tau & \qquad & \tau \longrightarrow K_1(1400)\nu_\tau \\ \qquad \hookrightarrow \rho(770)K & & \qquad \hookrightarrow K^*(892)\pi \\ \qquad\qquad \hookrightarrow \pi\pi & & \qquad\qquad \hookrightarrow K\pi \end{array}$$

Therefore, the easiest way to distinguish the two channels is the identification of the ρ and the K^*. To suppress the decay $\tau^- \to K^-\pi^+\pi^-(\geq 1\pi^\circ)\nu_\tau$, that may come from other decay processes, events with identified π° were rejected. Figure 6.20 (a) and (b) shows the distribution of invariant masses of oppositely charged kaon-pion and pion-pion pairs from the decay $\tau \to K\pi\pi\nu_\tau$. A peak at the K^* mass is clearly seen, while no obvious signal is visible at the ρ mass.

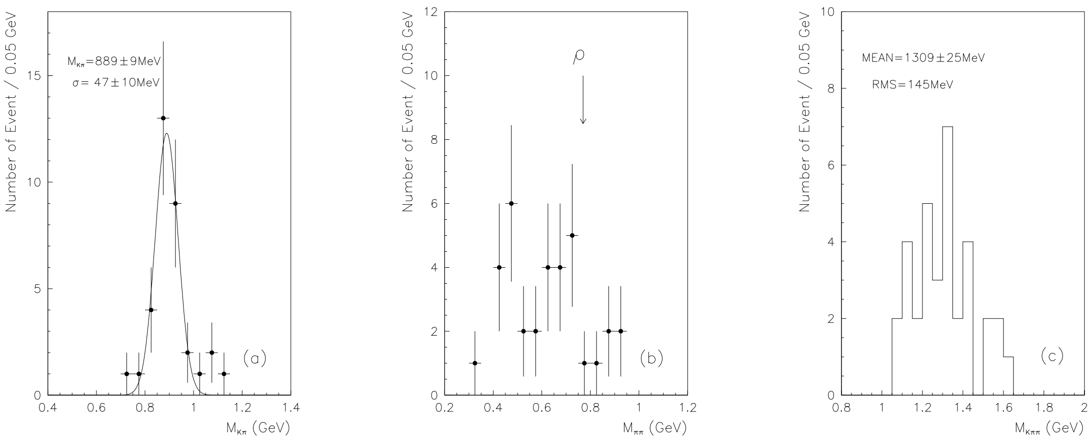

Figure 6.20: *Invariant mass (GeV) of (a) $K\pi$ from $K\pi\pi$ (b) $\pi\pi$ from $K\pi\pi$ (c) $K\pi\pi$*

The number of events outside the K^* resonance is compatible with the expected background. Therefore the conclusion is that the decay $\tau \to K\pi\pi\nu_\tau$ is dominated by the decay $\tau \to K^*\pi\nu_\tau$. However, the invariant mass of $K\pi\pi$ was also reconstructed (figure 6.20 (c)). A mean at $1.3GeV$ is observed, which is nearly 4 standard deviation below the mass of $K_1(1400)$ and compatible with the mass of $K_1(1270)$. Further study is needed.

In the decay $\tau^- \to K^-\pi^+\pi^-\pi^\circ\nu_\tau$, no obvious signals of K^{*0} and ρ^0 were observed from their charged decay. There might be resonance decays to one charged particle and a π°. This can not be confirmed because of low statistics and poor mass resolution caused by the neutrals.

6.4.2 Interpretation of the results and Comparison with other experiments

In the last decade or so, the τ decays to 3 particles with strangeness have been studied by several experiments, based on large data samples of τ decays. It is important to identify the kaon in order to suppress the huge background from non-strange decays. To do this several techniques have been used. Charged kaons are identified by their specific energy loss (dE/dx) or by Cherenkov radiation. As to neutral kaons K_S is tagged by the decay to two charged pions, and K_L is identified by a neutral hadronic shower in the calorimeter. In this section our results are interpreted and compared with other experiments.

$K^{*\circ}$ (or ρ) in the decays

As expected by the theory, the decay $\tau^- \to K^-K^+\pi^-\nu_\tau$ is found to be dominated by $\tau^- \to K^{*\circ}K^-\nu_\tau$.

For the decay $\tau^- \to K^-\pi^+\pi^-\nu_\tau$, the TPC/$2\gamma$[47] analysis of 23 $K\pi\pi$ events based on two-particle and three-particle masses found a higher production rate of $K_1(1400)$, while CLEO preferred predominance $K_1(1270)$ in decays to $K^\circ h^-\pi^\circ$[46]. Our result shows the dominance of $K^*\pi$ in the decay, but similar as CLEO the resonance of $K\pi\pi$ is close to $K_1(1270)$.

$Br(\tau^- \to K^*K^-\nu_\tau)$ and $Br(\tau^- \to K^*\pi^-\nu_\tau)$

CLEO[50] and ARGUS[49] have used the dE/dx method to suppress non-strange decays. The branching fraction was deduced from the $K^*(M_{K\pi})$ signals in the decays. Therefore, their results concern the branching fraction of $\tau^- \to K^{*\circ}K^-\nu_\tau \to K^-K^+\pi^-\nu_\tau$ and $\tau^- \to K^{*\circ}\pi^-\nu_\tau \to K^-\pi^+\pi^-\nu_\tau$. Our results of $\tau^- \to K^-K^+\pi^-(\pi^\circ)\nu_\tau$ and $\tau^- \to K^-\pi^+\pi^-\nu_\tau$ are comparable with theirs(Figure 6.21) because the decay $\tau^- \to K^-K^+\pi^-(\pi^\circ)\nu_\tau$ is saturated by $\tau^- \to K^{*\circ}K^-(\pi^\circ)\nu_\tau$, $\tau^- \to K^-\pi^+\pi^-\nu_\tau$ is saturated by $\tau^- \to K^{*\circ}\pi^-\nu_\tau$ and no significant $K^{*\circ}$ signal is present in the decay $\tau^- \to K^-\pi^+\pi^-(\geq 1\pi^\circ)\nu_\tau$. A good agreement is observed.

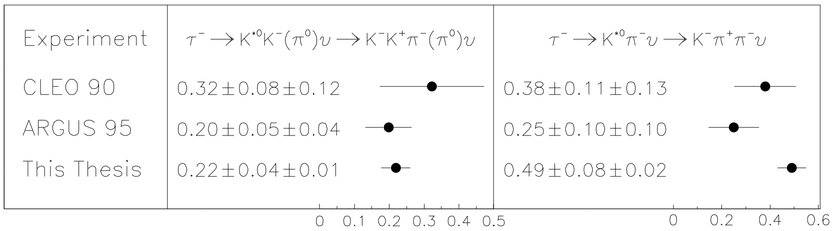

Figure 6.21: *The branching fractions (%) of $\tau^- \to K^{*\circ}K^-(\pi^\circ)\nu_\tau$ and $\tau^- \to K^{*\circ}\pi^-\nu_\tau$ compared with other experiments.*

The decay $\tau^- \to (K\pi\pi)^-\nu_\tau$

There are three decay modes for the decay $\tau^- \to (K\pi\pi)^-\nu_\tau$, :

$$\tau^- \to K^-\pi^+\pi^-\nu_\tau$$

$$\tau^- \to K^0\pi^0\pi^-\nu_\tau$$

$$\tau^- \to K^-\pi^0\pi^0\nu_\tau$$

The measured branching ratios of these decays are listed in table 6.7. In this table our result of $\tau^- \to K^-\pi^+\pi^-\nu_\tau$ without π° is used, while the other two branching

Decay mode	branching ratio (%)	relative ratio
$\tau \to K^-\pi^+\pi^-\nu$	0.49 ± 0.08	4
$\tau \to K^0\pi^0\pi^-\nu$	0.41 ± 0.07	4
$\tau \to K^-\pi^0\pi^0\nu$	0.09 ± 0.03	1

Table 6.7: *$K\pi\pi$ decay modes*

ratios are the world average of 1994[41], *i.e.* the average of the results of TPC, ALEPH and CLEO.

Assuming all $(K\pi\pi)^-$ go through $K^*\pi$, the relative branching ratios of these three decay modes can be determined from the Clebsch Gordan coefficients for isospin : $Br(K^-\pi^+\pi^-) : Br(K^0\pi^0\pi^-) : Br(K^-\pi^0\pi^0) = 4 : 4 : 1$. Table 6.7 shows an excellent agreement with this prediction. Under this assumption the branching ratio is:

$$Br(\tau \to K^*\pi\nu_\tau) = 0.94 \pm 0.10\%$$

The decay $\tau^- \to (KK\pi)^-\nu_\tau$
Similar to $(K\pi\pi)^-$, $(KK\pi)^-$ has three different decay modes:

$$\tau^- \to K^-K^+\pi^-\nu_\tau$$

$$\tau^- \to K^0K^0\pi^-\nu_\tau$$

$$\tau^- \to K^-K^0\pi^0\nu_\tau$$

Assuming all $(KK\pi)^-$ go through K^*K, from the Clebsch Gordan coefficients the relative branching ratios are predicted as $1 : 1 : 1$. Table 6.8 lists the measured branching ratios of these decays. Again our result of $\tau^- \to K^-K^+\pi^-\nu_\tau$ without π° is used, that of $\tau^- \to K^-K^0\pi^0\nu_\tau$ is the world average of 1994[41], and that of $\tau^- \to K^0K^0\pi^-\nu_\tau$ is the one from CLEO[51], which is determined from the decay $\tau^- \to K^0_SK^0_S\pi^-\nu_\tau$. Our branching ratio is nearly two standard deviations higher than the others.

Decay mode	branching ratio (%)	relative ratio
$\tau \to K^-K^+\pi^-\nu$	0.18 ± 0.04	1
$\tau \to K^0K^0\pi^-\nu$	0.083 ± 0.024	1
$\tau \to K^-K^0\pi^0\nu$	0.12 ± 0.03	1

Table 6.8: *$KK\pi$ decay mode*

Assuming all these decays come from K^*K and have the same the branching ratio, we have:

$$Br(\tau \to K^*K\nu_\tau) = 0.34 \pm 0.08\%$$

Chapter 7

Summary and Discussion

With the excellent performance of the RICH detector in DELPHI, we collected 92 candidates of 3-prong τ decay to charged kaon(s), which is the biggest data sample on these decays so far. The branching ratios of $\tau^- \to K^-K^+\pi^-(neutrals)\nu_\tau$ and $\tau^- \to K^-\pi^+\pi^-(neutrals)\nu_\tau$, determined with this sample, are more precise than the earlier measurements. The presence of additional π°'s in the decays is confirmed. The sample provides an opportunity to study the resonances in these decays. The semi-leptonic τ decay thus becomes more and more clear.

In the last few years, the branching ratios of almost all semi-leptonic τ decay channels have been studied in many experiments. The results are summarised in table 7.1 - 7.3, according to their final states. Here the π° and K_S° are treated as stable particles in the final states and the charges of the particles are not specified. The contribution of different charge channels has been calculated with the Clebsch Gordan coefficients for isospin. Most of the branching ratios are the world average of 1994[41]. $Br(K2\pi)$ and $Br(KK\pi)$ are the results of this thesis. $Br(K \geq 3\pi)$ and $Br(KK \geq 2\pi)$ are estimated under the assumption that these two decays are dominated by the decays $K3\pi$ and $KK2\pi$ via the channels $K^*\rho$ and K^*K^* respectively. Therefore the results of $Br(K^-\pi^+\pi^- \geq 1\pi^\circ)$ and $Br(K^-K^+\pi^- \geq 1\pi^\circ)$ in this thesis were multiplied by a factor of 12/5 and 9/2 respectively to get the $Br(K \geq 3\pi)$ and $Br(KK \geq 2\pi)$.

Table 7.1 lists the Cabibbo favoured decays, with typical final states $n\pi$ (n=1,2...).

Table 7.2 lists the Cabibbo suppressed decays with their corresponding Cabibbo favoured decays in the fourth column, where one π has been replaced by a K to get the Cabibbo suppressed decay. The decay rates should be suppressed by a factor of $\tan^2\theta_c = 0.05$. From the ratios of the branching ratios (last column) it is seen that they are consistent with this prediction for the different channels. The small differences are presumably caused by different phase spaces and interaction constant.

Table 7.3 lists the decays that are Cabibbo favoured but suppressed by creating a $K\bar{K}$ pair. To get a $K\bar{K}$ pair in the final states, a $s\bar{s}$ quark pair is produced and combined with ud from a π (figure 7.1). Therefore these final states can be compared to Cabibbo favoured decays with a π replaced by a $K\bar{K}$ pair. It is seen that all the decay rates are suppressed by about a factor of 0.012. According to perturbative QCD, a quark from the W may radiate a gluon and this gluon may decay into a quark pair. One can estimate this suppression to be order of $(\alpha_s(m_\tau)/\pi)^2 = 0.01$, in agreement with the result in the last column of table 7.3. These decays provide the simplest sample of the hadronic interaction in the cleanest environment at low energy. It is a great challenge for QCD to calculate this factor.

final state	resonance	Branching fraction %
π	—	11.09 ± 0.15
2π	ρ	24.91 ± 0.21
3π	$A_1 \to \rho\pi$	17.73 ± 0.28
4π	ρ'	5.2 ± 0.3
$\geq 5\pi$	—	1.0 ± 0.2

Table 7.1: *Cabibbo favoured Semi-leptonic τ decays*

final state	resonance	Branching fraction%	favoured	$Br/Br(n\pi)$
K	—	0.68 ± 0.04	π	0.061 ± 0.004
$K\pi$	K^*	1.36 ± 0.08	2π	0.055 ± 0.003
$K2\pi$	$K_1 \to K^*\pi$	0.94 ± 0.10	3π	0.053 ± 0.006
$K \geq 3\pi$	—	0.34 ± 0.09	$\geq 4\pi$	0.055 ± 0.015

Table 7.2: *Cabibbo suppressed Semi-leptonic τ decays*

final state	resonance	Branching fraction%	favoured	$Br/Br(n\pi)$
KK	—	0.13 ± 0.04	π	0.012 ± 0.004
$KK\pi$	K^*K	0.34 ± 0.08	2π	0.014 ± 0.003
$KK \geq 2\pi$	—	0.18 ± 0.09	$\geq 3\pi$	0.008 ± 0.004

Table 7.3: *Semi-leptonic τ decays with two kaons in the final state.*

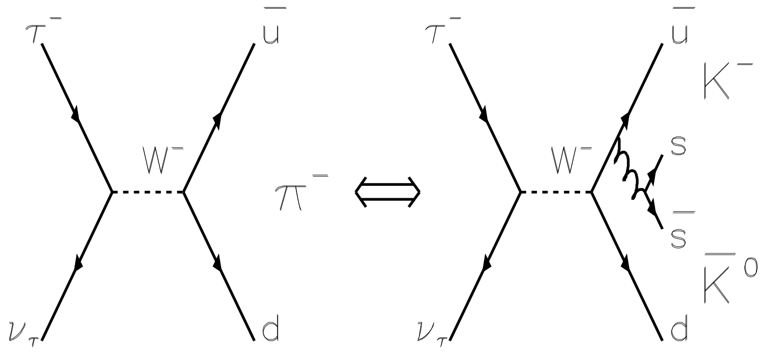

Figure 7.1: *The Feynman diagrams for $\tau \rightarrow \pi\nu_\tau$ and $\tau \rightarrow K\bar{K}\nu_\tau$.*

Bibliography

[1] S. L. Glashow, Nucl. Phys. **22** (1961) 579

[2] A. Salam, in "Proc. 8th Nobel Symposium Aspenasgorden" ed. N. Svartholm, Almquist and Wiksell, Stockholm (1968) 367

[3] S. Weinberg, Phys. Rev. Lett. **19** (1967) 1264

[4] UA1 Collaboration, G. Arnison et al, Phys. Lett. **B122** (1983) 103
UA1 Collaboration, G. Arnison et al, Phys. Lett. **B126** (1983) 389
UA2 Collaboration, P. Bagnaia et al, Phys. Lett. **B129** (1983) 130

[5] M. L. Perl et al, Phys. Rev. Lett. **35** (1975) 1489

[6] M. L. Perl et al, Ann. Rev. Nucl. Part. Sci. **30** (1980) 299

[7] Y. S. Tsai, Phys. Rev. **D4** (1971) 2821 (*erratum*: Phys. Rev. **D13** (1976) 771)

[8] F.J. Gilman and S. H. Rhie, Phys. Rev. **D31** (1985) 1066

[9] W. J. Marciano and A. Sirlin, Phys. Rev. Lett. **61** (1988) 1815

[10] R. Decker et al, Z. Phys. **C58** (1993) 455

[11] R. Decker and M. Finkemeier, Nucl. Phys. **B438** (1995) 17

[12] M. Finkemeier and E. Mirkes, **MAD-PH-882** hep-ph/9503474. March, 1995

[13] M. L. Perl, Ann. Rev. Nucl. Part. Sci. **30** (1980) 299

[14] A. J. Weinstein and R. Stroynowski, Ann. Rev. Nucl. Part. Sci. **43** (1993) 457

[15] Proceedings of the third Workshop on Tau Lepton Physics (Montreux, September, 1994), Nucl. Phys. B (proc. Suppl.) 40 (1995)

[16] BES Collaboration, J. Z. Bai et al, Phys. Rev. Lett. **69** (1992) 3021

[17] M. Davier, in: Proceedings of the third Workshop on Tau Lepton Physics (Montreux, September, 1994), Nucl. Phys. B (proc. Suppl.) 40 (1995) 395.

[18] D.I. Bretton et al, Phys. Rev. Lett. **68** (1992) 3000

[19] S. Weinberg, Phys. Rev. Lett. **18** (1967) 507

[20] T. Das, V. S. Mathur and S. Okubo, Phys. Rev. Lett. **18** (1967) 761

[21] the DELPHI collaboration, Technical Proposal, **DELPHI 83-66/1**, **CERN-PPE 90-128** (1990)
the DELPHI collaboration, DELPHI Progress Report, **DELPHI 84-60**
the DELPHI collaboration, Nucl. Instr. and Meth. **A303** (1991) 233

[22] N. Bingefors et al, Nucl. Instr. and Meth. **A328** (1993) 447

[23] F. Hartjes et al, Nucl. Instr. and Meth. **A256** (1987) 55

[24] C. Brand et al, Nucl. Instr. and Meth. **A283** (1989) 567

[25] A. Amery et al, Nucl. Instr. and Meth. **A283** (1989) 502

[26] H. Fischer et al, Nucl. Instr. and Meth. **A265** (1988) 218

[27] G. Alekseev et al, Nucl. Instr. and Meth. **A269** (1988) 652

[28] Y. Giomataris, DELPHI 86-72 RICH-19 (1986)

[29] T Ekelöf, DELPHI 85-11 RICH-5 (1985)

[30] J. Séguinot and T. Ypsilantis, Nucl. Instr. and Meth. **142** (1977) 377

[31] J. Séguinot et al, Nucl. Instr. and Meth. **173** (1980) 283;
E. Barrelet et al, Nucl. Instr. and Meth. **A 200** (1982) 219;
L. O. Eek et al, IEEE Trans. Nucl. Sci. **NS-31** (1984) 949
R. Arnold et al, Nucl. Instr. and Meth. **A 252** (1986) 188;
W. Dulinski et al, Nucl. Instr. and Meth. **A 252** (1986) 418;
D. Fraissard et al, Nucl. Instr. and Meth. **A 252** (1986) 524;
Barrel RICH Construction Group, DELPHI 66-22 RICH-22 (1986);
P. Beltran et al, Proc. Int. Symp. on Position Detectors in High-Energy Physics, Dubna, 1987, **JINR** D1-13-88-172, p.286;
R. Arnold et al, Nucl. Instr. and Meth. **A 270** (1988) 255;
R. Arnold et al, Nucl. Instr. and Meth. **A 270** (1988) 289;
D. Bloch et al, Nucl. Instr. and Meth. **A 273** (1988) 847;
P. Baillon et al, Nucl. Instr. and Meth. **A 277** (1989) 338;
G. Kalkanis et al, Nucl. Instr. and Meth. **A 283** (1989) 37;
F. Hahn et al Nucl. Instr. and Meth. **A 283** (1989) 686;
G. Van Apeldoorn et al, Nucl. Instr. and Meth. **A 283** (1989) 767;
P. Anrianos et al, Nucl. Instr. and Meth. **A 294** (1990) 424;
E. G. Anassontzis et al, IEEE Trans. Nucl. Sci. **NS-38** (1990) 417.

[32] E. Anassontzis et al, The Barrel Ring Imaging Cherenkov counter of DELPHI
Nucl. Instr. and Meth. **A323** (1992) 351

[33] W. Adam et al, The forward ring imaging Cherenkov detector of DELPHI
Nucl. Instr. and Meth. **A338** (1994) 284

[34] A. Breskin et al, Nucl. Instr. and Meth. **124** (1975) 189-214

[35] B. Schmidt, Private communication.

[36] K. F. Ness, Phys. Rev. **E 47** (1993) 327

[37] T. Sjöstrand, " PYTHIA 5.6 JETSET 7.3 Physics and Manual " preprint CERN-TH 6488/92 (1992)

[38] S. Jadach, B.F.L. Ward and Z. Was. Comput. Phys. Commun. **66** (1991) 276.

[39] P. Abreu et al, The DELPHI collabration. Phys. Lett. **B 334** (1994) 435

[40] E. Agasi, Ph. D. Thesis, NIKHEF. *to be published*

[41] B. Heltsley, in: Proceedings of the third Workshop on Tau Lepton Physics (Montreux, September, 1994), Nucl. Phys. B (proc. Suppl.) 40 (1995) 413.

[42] P. Abreu et al, The DELPHI collabration. Nucl. Phy. **B 444** (1995) 3

[43] P. Abreu et al, The DELPHI collabration. Z. Phys. **C 55** (1992) 555

[44] G. B. Mills, The DELCO collabration. Phys. Rev. Lett. **54** (1985) 624

[45] Nading Qi, in: Proceedings of the third Workshop on Tau Lepton Physics (Montreux, September, 1994), Nucl. Phys. B (proc. Suppl.) 40 (1995) 387.

[46] J. G. Smith, in: Proceedings of the third Workshop on Tau Lepton Physics (Montreux, September, 1994), Nucl. Phys. B (proc. Suppl.) 40 (1995) 351.

[47] D. A. Bauer et al, The TPC/Two-Gamma collabration. Phys. Rev. **D50** (1994) 13

[48] C. Hast, Dortmund Ph.D. Thesis (1993)

[49] H. Albrecht et al, The ARGUS collabration. DESY 95-087, May,1995

[50] M. Goldberg et al, The CLEO collabration. Phys. Lett. **B 251** (1990) 223

[51] R. Balest et al, The CLEO collabration. CLEO CONF 94-25. July 18, 1994.

Summary

This thesis presents the measurement of kaon production in 3-prong τ decays. The data sample of Z^0 events is used that was recorded with the DELPHI detector at LEP in 1992,1993 and 1994. Charged kaons in the τ decay are identified on a track-by-track basis using the Ring Imaging Cherenkov detector (RICH). The branching ratios of $\tau^- \rightarrow K^-K^+\pi^-(neutrals)\nu_\tau$ and $\tau^- \rightarrow K^-\pi^+\pi^-(neutrals)\nu_\tau$ are determined. The resonance structure of these two decays is studied. Evidence for a simple QCD process of kaon pair production in τ decay is discussed.

The first chapter is a general introduction in high energy physics. It gives the motivation of the analysis.

The second chapter describes briefly the theory of modern elementary particle physics, the Standard Model. The properties of the τ lepton are summarised, and the relevant theories for semi-leptonic τ decay are introduced.

In the third chapter, the DELPHI detector is described. The RICH sub-detector plays an important role in the particle identification. The mass of the particle is determined from its velocity, as determined by the Cherenkov angle in the RICH, and its momentum as measured by other sub-detectors.

The on-line calibration of the Forward RICH detector is discussed in chapter four. In the Forward RICH drift tube the single photo-electrons drifts in a plane perpendicular to the 1.2 T magnetic field. With the calibration system the drift velocity and the Lorentz angle were measured with an accuracy of 0.2% and 0.4% respectively. Some other properties of the Forward RICH were also determined with the calibration system.

In chapter five, the performance of the RICH detector is discussed. The angular resolution of the RICH detector is improved by 10% by using muons from $Z^\circ \rightarrow \mu^+\mu^-$. For single-prong τ decays a misidentification rate of 0.15% is achieved both for ring and veto identifications.

In chapter six, the particle identification techniques are extended to three-prong τ decay with the similar misidentification rate. The branching ratios of $\tau^- \rightarrow K^-K^+\pi^-(neutrals)\nu_\tau$ and $\tau^- \rightarrow K^-\pi^+\pi^-(neutrals)\nu_\tau$ are determined to be $(0.22 \pm 0.04 \pm 0.01)\%$ and $(0.63 \pm 0.09 \pm 0.03)\%$ respectively. The π° production in these two decays is confirmed. It is found that the decay $\tau^- \rightarrow K^-K^+\pi^-(\pi^\circ)\nu_\tau$ is dominated by the decay $\tau^- \rightarrow K^-K^{*0}(\pi^\circ)\nu_\tau$ and the decay $\tau^- \rightarrow K^-\pi^+\pi^-\nu_\tau$ is dominated by the decay $\tau^- \rightarrow \pi^-K^{*0}\nu_\tau$.

In chapter seven, the status of branching ratio measurement in hadronic τ decay is discussed. The decay modes are classified in three different types. The Cabibbo

favoured decays are characterised by pions in the final state. The Cabibbo suppressed decay have a pion is replaced by a kaon, which suppresses the decay rate by a factor of $\tan^2\theta_c = 0.05$. Decays of the third class are Cabibbo favoured, but a pion replaced by a pair of kaons. Their decay rates are suppressed by a factor of 0.012. It can be understood as gluon emisson by one of the two quarks in the final state, with the gluon decaying into a $s\bar{s}$ pair.

samenvatting

Dit proefschrift beschrijft de meting van kaon productie in het verval van het τ lepton naar drie geladen deeltjes. Gebruik is gemaakt van Z^0 verval naar τ paren. De meetgegevens werden verzameld met de DELPHI detector bij LEP in de jaren 1992, 1993 and 1994. Geladen kaonen in het τ verval werden geidentificeerd met de Ring Imaging Cherenkov detector (RICH). De vertakkingsverhoudingen van $\tau^- \rightarrow K^-K^+\pi^-(neutralen)\nu_\tau$ en $\tau^- \rightarrow K^-\pi^+\pi^-(neutralen)\nu_\tau$ zijn bepaald en de resonantiestructuur van deze twee vervalswijzen is onderzocht. Aangeduid wordt, hoe een eenvoudig QCD proces de paarproductie van kaonen in τ verval kan beschrijven.

Het eerste hoofdstuk schetst in algemene termen het vakgebied der hoge energie fysica. De motivatie voor het onderzoek van τ verval naar hadronen wordt gegeven.

Het tweede hoofdstuk beschrijft in het kort het Standaard Model, de theorie van de moderne elementaire deeltjes fysica. De eigenschappen van het τ lepton worden opgesomd en een inleiding wordt gegeven van relevante theorieen voor het semi-leptonische τ verval.

In het derde hoofdstuk wordt een beschrijving gegeven van de DELPHI detector. De RICH sub-detector speelt een belangrijke rol in de identificatie van de deeltjes. De massa van een deeltje wordt bepaald uit de snelheid, als bepaald door de Cherenkov hoek in de RICH, en de impuls als gemeten in andere sub-detectoren.

De ijking van de voorwaartse RICH detector wordt besproken in hoofdstuk vier. In de driftbuis van de voorwaartse RICH bewegen foto-electronen loodrecht op het magnetisch veld van 1.2 Tesla. De driftsnelheid en de Lorentz hoek werden met het ijksysteem gemeten tot op respectievelijk 0.2% en 0.4% nauwkeurig. Enige andere eigenschappen van de voorwaartse RICH werden eveneens met het ijksysteem bepaald.

In hoofdstuk vijf worden de eigenschappen van de RICH detector besproken. Door gebruik te maken van muonen van het verval $Z^\circ \rightarrow \mu^+\mu^-$ wordt het scheidend vermogen van de RICH detector met 10% verbeterd. De fractie van onjuist geidentificeerde deeltjes bedraagt met de ring- en veto- methoden 0.15%.

In hoofdstuk zes wordt de techniek voor identificatie uitgebreid tot drie-deeltjes vervalswijzen. De vertakkingsverhoudingen voor $\tau^- \rightarrow K^-K^+\pi^-(neutralen)\nu_\tau$ en voor $\tau^- \rightarrow K^-\pi^+\pi^-(neutralen)\nu_\tau$ zijn respectievelijk bepaald als $(0.22 \pm 0.04 \pm 0.01)\%$ en $(0.63 \pm 0.09 \pm 0.03)\%$. De productie van neutrale pionen is in beide vervalswijzen aangetoond. Het verval $\tau^- \rightarrow K^-K^+\pi^-(\pi^\circ)\nu_\tau$ verloopt voornamelijk via het kanaal $\tau^- \rightarrow K^-K^{*0}(\pi^\circ)\nu_\tau$ en het verval $\tau^- \rightarrow K^-\pi^+\pi^-\nu_\tau$ voornamelijk via

$\tau^- \to \pi^- K^{*0} \nu_\tau$.

Hoofdstuk zeven biedt een overzicht van de hadronische vervalswijzen van het τ lepton. Er zijn drie verschillende vervalstypes. Het Cabibbo-toegelaten verval is gekarakteriseerd door pionen in de eindtoestand. Het Cabibbo-verboden verval wordt verkregen uit het toegelaten verval door een pion te vervangen door een kaon. Deze vervalswijze is onderdrukt met een factor $\tan^2 \theta_c = 0.05$. In het derde type is een pion vervangen door twee kaonen. De vervalsnelheid is ten opzichte van het toegelaten verval met een factor 0.012 gereduceerd. Dit vervalsproces kan opgevat worden als een toegestaan verval waarin een der quarks echter een gluon uitstraalt, dat zelf weer vervalt in een $s\bar{s}$ quarkpaar.

Acknowledgements

Over the past few years, I have received great support and help from many people. I gladly take this opportunity to express my gratefulness to all of them, who made this thesis possible.

I profitted greatly from working in the Forward RICH group under the leadership of Dr. O. Ullaland and Dr. B. Nielsen. With their help I learned a great deal about the detectors, especially the RICH detector. This formed a strong basis for my later data analysis.

I awe a lot to Dr. D. Holthuizen for his careful reading of the manuscript and countless suggestions that improved the thesis both in English and Physics. It has been a pleasure to work and discuss with other people in the DELPHI group of NIKHEF. I can not forget Dr. J. Timmermans, Dr. P. Kluit, Dr. D. Toet, Dr. M. Heijden, Dr. M. Merk, E. Agasi, J. van Eldik and I. Siccama for being always available to help me, overcoming many difficulties and filling my chicken head with their intelligence and humour that made my life and work very enjoyable.

From discussions with Prof. K.J.F. Gaemers, I learned a lot about theories.

Finally I would like to express my gratitude to my mother and to my wife for their love and support.

Curriculum Vitae

First of all, a confession has to be made. The author of this thesis is not a pure scientist, because he is half superstitious. He was born in Beijing, P.R.China on November 30, 1961. A thing he remembers of the primary school is that one day a teacher told him: "Hi boy, you have a magic name (In Chinese, 'HAO' means good and 'WEI' means very good or great). You might do something excellent later."

He started his study of physics at Peking University in 1980. In 1984 he obtained his Bachelor of Science degree in physics. In the same year he entered the Institute of High Energy Physics as graduate student to join the BES collaboration. In 1987, he obtained his master degree in experimental high energy physics.

In June 1987, he was selected to attend the ICFA school on Instrumentation in Elementary Particle Physics (Trieste, Italy), where he belonged to the top four students.

From February 1990, he worked in the SPACAL group in the LAA project at CERN. Not long after he came to CERN, one of his friends told him: "Hi guy, you have a strange name (In English 'HAO' reads HOW and 'WEI' reads WHY). Why is that?" At that time he could not answer this question, but he knew that he must be very good in research. The SPACAL project developed the SPAghetti CALorimeter, that is made of lead and scintillating fiber.

In September 1991, he joined the NIKHEF group in the DELPHI collaboration. In the first two years, he worked at CERN, Geneva. He contributed to the analysis of UV calibration data for the Forward RICH drift tube. In September 1993, he started his analysis of charged kaons in three-prong τ decays at NIKHEF, Amsterdam.

In 1992, he won the trophy of the table-tennis tournament of the Dutch-German-Belgian Graduate Student Summer School in Dalfsen, The Netherlands. In the bridge tournaments of the VVGA bridge club in Amsterdam, he once won a box of chocolate and once a bottle of whiskey.

After finishing this thesis he realised that the real meaning of his name is: "HAdrOns in WEak Interaction".